UNIVERSITY OF OKLAHOMA
GRADUATE COLLEGE

FACTORS INFLUENCING RATES AND PRODUCTS IN THE TRANSFORMATION OF CARBON TETRACHLORIDE BY ZEROVALENT IRON METAL

A THESIS

SUBMITTED TO THE GRADUATE FACULTY

In partial fulfillment of the requirements for the degree of

MASTER OF SCIENCE

ENVIRONMENTAL ENGINEERING

By

María L. Támara

Norman, Oklahoma
2003

UNIVERSITY OF OKLAHOMA
LIBRARIES

OU
THESIS
TAM
COP. 2

FACTORS INFLUENCING RATES AND PRODUCTS IN THE TRANSFORMATION OF CARBON TETRACHLORIDE BY ZEROVALENT IRON METAL

A THESIS APPROVED FOR THE
SCHOOL OF CIVIL ENGINEERING AND ENVIRONMENTAL SCIENCE

BY

[redacted]

Elizabeth C. Butler, Chair

[redacted]

David A. Sabatini

[redacted]

Mark A. Nanny

© Copyright by Michael Thomas Spies
All Rights Reserved

© Copyright by María L. Támara 2003
All rights Reserved.

ACKNOWLEDGMENTS

I would like to thank Dr. Elizabeth Butler for her support and guidance throughout the development of this work, the School of Civil Engineering and Environmental Science, and the Graduate College for providing financial support to complete this research. I also express my gratitude to Edgar Acosta and Nopawan Ratasuk for their help in the initial stages of the laboratory work. I acknowledge the encouragement and help given to me by my husband, Harry J. Barraza, whose example of dedication and hope in a better future is worth to follow. Most importantly, I thank God for all the blessings received every day, especially while pursuing this degree program.

TABLE OF CONTENTS

LIST OF TABLES

LIST OF FIGURES

ABSTRACT

Batch experiments were conducted to study the influence of iron purity and solution chemistry, i.e., pH and common groundwater species such as HS^-, HCO_3^- and Mn(II), on the anaerobic degradation of carbon tetrachloride (CT) by iron metal (Fe^0). CT degradation experiments by four commercial irons at pH values of 7 and 9.3 indicated that iron purity and extent of oxidation affect the rate of CT transformation. In contrast, the product distribution was not significantly affected by iron purity, with chloroform (CF) being the major product in all cases. Surface area normalized rate constants ($k_{obs,SA}$), backscattered electron images, and elemental composition analysis of the untreated metals indicate that the highest purity and least oxidized Fe^0 was the most reactive in transforming CT. High pH values slowed the rates of CT disappearance by Peerless Fe^0 and led to a pattern of decreasing CF yields as the pH increased from 7 to 12.9. The Fe/O atomic ratio vs depth, obtained by depth profiling analysis with X-ray photoelectron spectroscopy (XPS), for Peerless Fe^0 filings equilibrated at pH 7 and 9.3 suggested that the oxide layer is thicker at pH 9.3, which may explain the slower rates of CT transformation as pH increases. Ground water constituents such as HS^-, HCO_3^- and Mn(II) affected the rates of CT by a high-purity Fe^0, but did not strongly influence product distribution, except for HS^-, where less CF was produced, possibly due to the formation of carbon disulfide (CS_2). The results have practical implications for in situ remediation of groundwater contaminated with chlorinated organic compounds by iron permeable reactive barriers.

INTRODUCTION

Carbon tetrachloride (CT) is a groundwater pollutant currently regulated under the Safe Drinking Water Act with a maximum contaminant level (MCL) of 5 μg/L (*1*). In addition, CT is a persistent compound because it is neither readily biodegradable nor oxidizable under aerobic conditions (*1-2*). CT, however, is more amenable to transformation in reducing environments. In fact, CT degradation has been accomplished by various reducing agents, including vitamin B_{12}, Fe^0, iron minerals, and sulfur-containing compounds (*3-6*).

Under reducing conditions, CT can be transformed by two main pathways: (1) hydrogenolysis, or replacement of chlorine by hydrogen in the CT molecule during electron transfer, to produce chloroform (CF), which is toxic, and (2) dichloroelimination, which produces completely dechlorinated products such as carbon monoxide (CO) and formate ($HCOO^-$) via hydrolysis of a dichlorocarbene intermediate (*3*, *6-15*).

Fe^0 is a powerful reductant that has found application in remediating groundwater contaminated with chlorinated organic compounds (*16*). Fe^0 is effective in transforming these contaminants to products that can either be more benign or as toxic as the parent compound. For example, TCE can be degraded via sequential hydrogenolysis to vinyl chloride (VC), which is toxic, or through dichloroelimination to acetylene, ethane, and ethane (*17*). CF has been reported as the only major product (yields > 50%) of CT reduction by Fe^0 in aqueous systems (*1, 4, 18*). Benign products such as $HCOO^-$, CO, and carbon dioxide could account for the incomplete mass balance on carbon observed in those systems. Completely dechlorinated products such as CO, $HCOO^-$, and acetylene are

more readily metabolized by microorganisms or susceptible to abiotic transformation pathways (e.g., hydrolysis and oxidation).

Thus, Fe^0 permeable reactive barriers (PRBs) have emerged as a passive, cost-effective technology to clean-up contaminated groundwater in situ (*16*). Previous studies have addressed the influence of surface area, groundwater constituents (i.e., carbonates, sulfides, organic matter content, anthropogenic substances), and pH on the rates of chlorinated contaminant transformation by Fe^0 (*4*, *19-26*). However, the influence of groundwater characteristics and Fe^0 impurities on the distribution of reaction products has not yet been thoroughly investigated, and is the focus of this research. Identifying conditions that favor benign products (e.g., $HCOO^-$ and CO) and that lead to fast contaminant transformation rates is desirable for a realistic design and operation of Fe^0 PRBs.

In this work, we studied the effects of Fe^0 type and impurities, groundwater characteristics ($[HS^-]$, $[HCO_3^-]$, [Mn(II)], and pH), and Fe^0 acid-washing pretreatment, which removes unreactive oxides and/or promotes pitting corrosion, on the rates and products in the anaerobic transformation of CT by Fe^0 in batch systems. We chose CT as a model compound because of its widespread presence in contaminated aquifers, its well-known transformation pathways under reducing conditions, and its relatively fast transformation rates by Fe^0. Four commercial Fe^0 metals, two electrolytic and two cast Fe^0, were chosen because of their differences in types and content of impurities, arising from their manufacturing methods.

This document is organized in four chapters. Chapter 1 presents the background literature supporting the hypothesis of this research as well as the tasks devised to test it.

Next, Chapter 2 compiles the materials and experimental methods developed to accomplish the research tasks. After this, Chapter 3 displays the experimental results along with possible explanations of the observed trends. Finally, Chapters 4 and 5 present conclusions and recommendations for groundwater remediation applications and for future work in this area.

1. BACKGROUND

1.1 In Situ Treatments

In situ transformation of CT occurs by natural degradation processes occurring in the subsurface or in Fe^0 PRBs (*17*, *27*). Abiotic and biotic natural degradation processes, which constitute a form of natural attenuation, have been reported to transform CT under reducing conditions (*27*). Minerals such as ferrous sulfides (FeS) and Fe(II) oxides (e.g., magnetite), naturally present in the subsurface because of the activity of sulfate reducing bacteria and the microbial reduction of Fe(III) oxides, have shown reactivity in transforming CT (*5*, *11*, *28-29*).

Microbial-mediated transformation of CT can also take place as found in batch and column experiments (*27*). Microbial processes, however, are constrained by the availability of nutrients, electron donors, oxygen supply, contaminant physical properties (i.e., concentration, solubility, etc.), so that biostimulation and air sparging may be necessary in order to achieve remediation goals at a particular site (*30*). There is still the need for long-term field studies to evaluate the effectiveness of natural attenuation processes as the only alternative to remediate contaminated sites.

Although natural attenuation is cost-effective in comparison to engineered remediation strategies such as Fe^0 PRBs, degradation of a contaminant by natural processes generally occurs over long periods of time and it is highly dependent on the biogeochemistry of the site (*31*). Therefore, when rapid action is needed to contain a contaminated groundwater plume before it poses a risk on public health, engineered techniques may be preferred over natural attenuation. The major advantage of PRBs is

that they can remediate contaminants in a passive way with minimal maintenance required, but the long-term performance of these barriers is still under investigation (*32*).

1.2 Chemistry of Fe^0 PRBs

PRBs are placed in the subsurface, where contaminated groundwater flows through the reactive medium and reduction of the chlorinated organic compounds takes place, forming products that can be either completely or partly dechlorinated. For illustrative purposes, this redox process can be represented by the following two half reactions:

$$RCl + H^+ + 2e^- \rightarrow RH + Cl^- \quad (1.1)$$

$$Fe^0 \rightarrow Fe^{2+} + 2e^- \quad (1.2)$$

which involve hydrogenolysis of the contaminant, designated as RCl, to a product RH plus chloride anion (eq 1.1), and aqueous iron corrosion (eq 1.2). Note that reduction of the contaminant can occur via reactions other than hydrogenolysis such as reductive dichloroelimination. The next equations show the transformation of TCE (C_2Cl_3H) and CT (CCl_4) via reductive dichloroelimination.

$$C_2Cl_3H + 2e^- \rightarrow C_2HCl + 2Cl^- \quad (1.3)$$

$$CCl_4 + 2e^- \rightarrow :CCl_2 + 2Cl^- \quad (1.4)$$

Reductive dichloroelimination is referred to as β-elimination for TCE since the two Cl^- anions are eliminated from adjacent carbon atoms whereas geminal dichloroelimination is the name given to CT dichloroelimination because the two Cl^- anions are eliminated from the same carbon. Both chloroacetylene (C_2HCl) and the dichlorocarbene ($:CCl_2$) are transient and very reactive intermediates.

The overall reaction resulting from adding eqs 1.1 and 1.2 is thermodynamically feasible because its Gibbs free energy is negative according to,

$$\Delta G^0 = -n\,F\,(E_1^{\,0} - E_2^{\,0}) \qquad (1.5)$$

where $E_1^{\,0} > E_2^{\,0}$; $E_1^{\,0}$ and $E_2^{\,0}$ are the standard reduction potentials for reaction (1.1) and the reverse of reaction (1.2), respectively, n is the number of electrons transferred, and F is the Faraday constant (96,490 Coulombs per mole of electrons). Schwarzenbach et al. (*33*) reported $E_1^{\,0}$ = + 0.67 V for the half reaction of CT hydrogenolysis at pH 7. In contrast, $E_2^{\,0}$ for the iron half reaction is equal to – 0.44 V (*4*).

Two other competing reduction reactions can also occur. Under aerobic conditions, iron corrosion can be coupled with reduction of dissolved oxygen,

$$O_2(aq) + 2\,H_2O + 4\,e^- \Leftrightarrow 4\,OH^- \qquad (1.6)$$

whereas under anaerobic conditions water can be reduced to molecular hydrogen as illustrated in the next equation:

$$2\,H_2O + 2\,e^- \Leftrightarrow H_2 + 2\,OH^- \qquad (1.7)$$

The solution pH increases primarily due to release of hydroxyl groups (see eqs 1.6 and 1.7) and, to a lesser extent by the consumption of protons (see eq 1.1), is expected in the vicinity of the PRB. This pH rise will drive the precipitation of iron (oxy)hydroxides (e.g., FeOOH) and carbonates (e.g., siderite ($FeCO_3$), calcite/aragonite ($CaCO_3$), and magnesite ($MgCO_3$)) on the barrier. Precipitation of amorphous FeS can also occur under sulfate-reducing conditions. Finally, a film of hydrogen (H_2) may form on the barrier surface as a result of the reduction of water (eq 1.7) under anaerobic conditions.

1.3 Kinetics of CT Reduction

Aqueous CT degradation by iron metal can exhibit either zero or pseudo-first order kinetics depending on the initial concentration of CT as well as on the availability of reactive sites, the latter being influenced by the surface area of the iron metal. At low initial concentrations, CT disappearance is proportional to its aqueous concentration, but at high initial concentrations, the reactive sites become saturated, so that the rate of CT reduction is constant (*34*). The rate laws for zero and pseudo-first order CT disappearance kinetics are:

$$-\frac{d[CT]}{dt} = k_{obs} \tag{1.8}$$

$$-\frac{d[CT]}{dt} = k_{obs}[CT] \tag{1.9}$$

where k_{obs} is the overall reaction rate constant.

Previous studies indicate that iron surface area is the main factor determining the degradation rates of chlorinated solvents (*35*). In fact, there exists a linear relationship between k_{obs} and the iron surface concentration, ρ (m^2/L of solution), according to:

$$k_{obs} = k_{SA}\rho \tag{1.10}$$

where k_{SA} is the surface-normalized rate constant (*35*).

The surface-mediated reduction of CT involves several steps. First, this contaminant diffuses from the bulk of the solution to the iron oxide-water interface. Next, it adsorbs on the iron surface, where it undergoes chemical transformation. Finally, the reaction products diffuse out to the solution. Thus, the slowest step dictates the overall rate of transformation (*16*). A study of the electrochemical reduction of CT at an oxide-free iron electrode showed that the rate of reduction of CT was dominated by reaction at

the metal-water interface rather than by CT diffusion to the metal-water interface (*36*). Similarly, the rate of reduction of CT by oxide-covered Fe^0 in well-mixed batch systems appeared to be significantly controlled by reaction at the surface as evidenced by the large activation energy of the reaction (*36*). Thus, the rate of CT reduction in both oxide-free and oxide-covered Fe^0 is dominated by chemical rather than by mass-transport processes.

1.4 Reaction Pathways

The mechanism of CT transformation and its reaction products under reducing conditions has been studied in a variety of systems (*3*, *6-15*, *27*). It has been postulated that the rate-limiting step in the reduction of CT by Fe^0 is a one-electron reduction to form a trichloromethyl radical ($\cdot CCl_3$) plus chloride (Cl^-) (*4*). The strong correlation between the overall reaction rate constants and the one-electron reduction potentials for several polyhalogenated alkanes as well as the trapping of the radical support this hypothesis (*37*).

The trichloromethyl radical may react in different ways. It can abstract a hydrogen atom species to yield CF (see (**a**) in Figure 1.1) (*4*). The radical can also accept another electron to form a trichloromethyl carbanion ($^-:CCl_3$), which upon protonation leads to CF (see (**b**) in Figure 1.1) (*9*). Alternatively, the radical can undergo electron transfer and Cl^- release to form a dichlorocarbene intermediate ($:CCl_2$) (see (**c**) in Figure 1.1) (*38*).

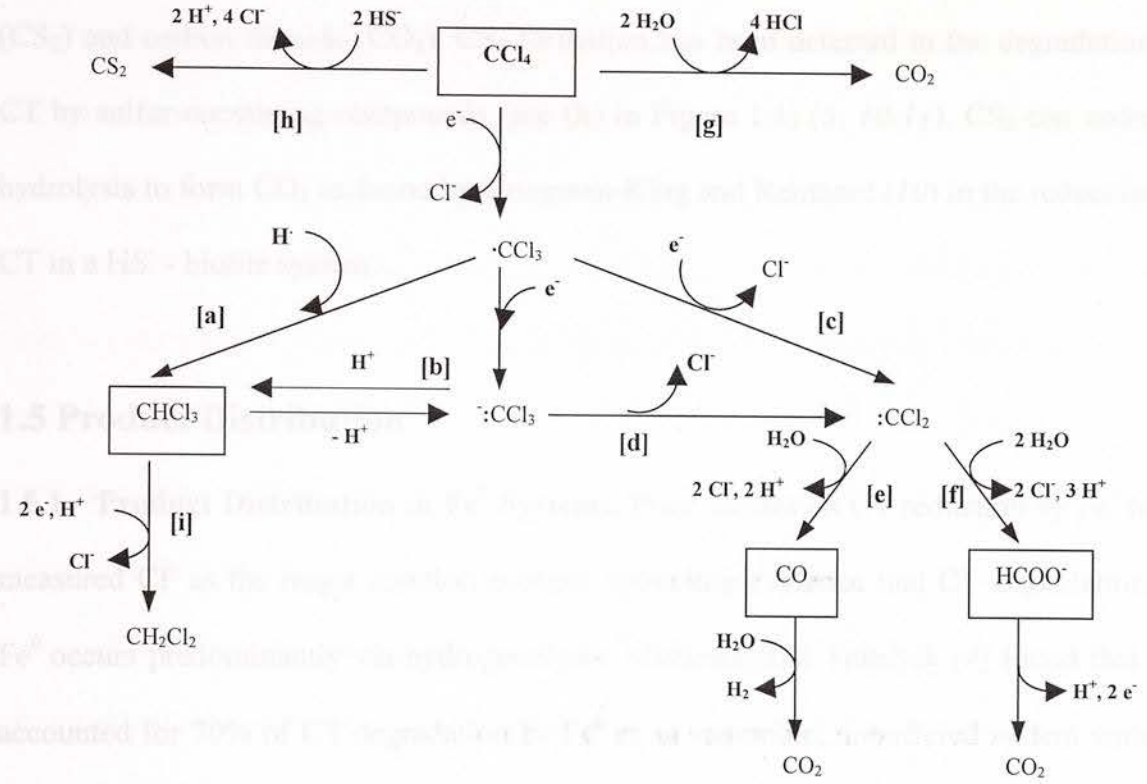

Figure 1.1 Possible pathways for CT degradation (*3*, *6-15*, *27*). Letters a through i identify different pathways. Compounds measured in our experimental systems are enclosed in boxes.

Hydrolysis of the carbene intertermediate leads to CO or $HCOO^-$ (see (**e**) and (**f**) in Figure 1.1) (*7-8*). Direct nucleophilic attack at chlorine (x-philic attack) by electron rich species, such as compounds having reduced sulfur moieties, could also produce the trichloromethyl carbanion that upon decay produces the dichlorocarbene (see (**d**) in Figure 1.1). Indeed, carbenes were trapped in the transformation of CT in the presence of mercaptojuglone and cysteine, suggesting a two-electron transfer or nucleophilic attack at chlorine to produce a trichloromethyl carbanion that upon chloride expulsion yields the dichlorocarbene (*6*). From a remediation standpoint, CO and $HCOO^-$ formation is preferred over CF since the latter compound is toxic.

Other products that may form under reducing conditions are carbon disulfide (CS_2) and carbon dioxide (CO_2). CS_2 formation has been detected in the degradation of CT by sulfur-containing compounds (see (**h**) in Figure 1.1) (*5*, *10-11*). CS_2 can undergo hydrolysis to form CO_2 as found by Kriegman-King and Reinhard (*10*) in the reduction of CT in a HS^- - biotite system.

1.5 Product Distribution

1.5.1 Product Distribution in Fe^0 Systems. Prior studies on CT reduction by Fe^0 have measured CF as the major reaction product, providing evidence that CT degradation by Fe^0 occurs predominantly via hydrogenolysis. Matheson and Tratnyek (*4*) found that CF accounted for 70% of CT degradation by Fe^0 in an anaerobic, unbuffered system with an initial pH of 8.0. Over longer periods of time, dichloromethane (DCM), the hydrogenolysis product of CF (see (**i**) in Figure 1.1), appeared and accounted for 50% of the CF lost. Dichloroelimination products such as formate and carbon monoxide were not analyzed in that research.

Helland et al. (*1*) reported that CF formation accounted for 49% of CT removed by Fe^0 in an aerobic, unbuffered system. The authors hypothesized that the incomplete mass balance was due to competing reactions such as reductive hydrolysis through a dichlorocarbene intermediate or dimerization of trichloromethyl radicals. In the work by Warren et al. (*18*) about CT dehalogenation by Fe^0 in a buffered system at pH 5.8, CT disappearance almost paralleled CF production, with an estimated CF yield of 89%.

Electrochemical reduction of CT at Fe^0 electrodes also points towards hydrogenolysis as the predominant pathway (*39*, *40*). The reductive transformation of CT

at an oxide-free Fe^0 electrode, with cathode potential (E_c) of –800 mV and pH 7, resulted in CF accounting for 70% of the CT disappearance (*40*). DCM and methane (CH_4) formed over a longer period of time. However, CH_4 seemed to originate from a pathway not involving DCM as an intermediate since DCM was not degraded under the conditions of the experiment. The product distribution was a function of the cathode potential, with more negative potential values leading to higher yields of methane and faster rates of CT reduction. Li and Farrell (*41*) also conducted electrochemical reduction of CT at an oxide-free iron electrode in an unbuffered system, with an initial pH of 6.5. In this system, CF accounted for 90% of CT disappearance.

The differences among the yields of CF in the systems previously discussed are most likely due to different experimental conditions. Solution chemistry, in particular pH and dissolved oxygen, as well as reduction potential appear to be key variables driving product distribution.

1.5.2 Product Distribution in Other Systems. Kriegman-King and Reinhard (*10*) addressed CT transformation in a system containing bisulfide (HS^-) and biotite (a silicate of iron, magnesium, potassium, and aluminum) under anaerobic conditions. They found that CS_2 formation was the major transformation pathway. Direct nucleophilic attack of HS^- at carbon or reduction of CT to a trichloromethyl radical that can react with HS^- or polysulfides (S_x^{2-}) were hypothesized to be the steps preceding CS_2 production. In this system, hydrolysis of CS_2 generated CO_2. It was estimated that, ultimately, CO_2 represented 85% of the initial CT concentration whereas CF accounted for only 5%. Later, Kriegman-King and Reinhard (*11*) conducted CT degradation by fresh pyrite

(FeS_2) under anaerobic conditions at pH 6.5 and 25°C. At the end of the experiment, CT, CF, $HCOO^-$, CS_2, CO_2, and an adsorbed nonvolatile fraction, were quantified as 1%, 48%, 5%, 2%, 10%, and 12% of the initial CT concentration, respectively. The authors acknowledged that a S_N2 reaction between FeS_2 and CT was unlikely. Instead, a mechanism that consists of an initial one-electron transfer from pyrite to CT to form a trichloromethyl radical was proposed.

Devlin and Muller (*5*) presented evidence for two competing pathways producing CF and CS_2 in the transformation of CT under sulfate reducing conditions during a field bioremediation experiment. Column experiments designed to simulate field conditions were also carried out. It was observed that the ratio of CF to CS_2 was approximately 2:1 in both field and column experiments. Furthermore, batch experiments of CT degradation by fresh amorphous FeS gave the same 2:1 CF: CS_2 ratio. From this, the authors concluded that the consistency in the CF: CS_2 ratio was indicative of a pathway involving the abiotic transformation of CT by amorphous FeS of biogenic nature. Results from a long-term study on CT degradation in a reducing groundwater environment showed that FeS-mediated reduction occurred because the estimated CF:CS_2 ratio from field measurements was 2.4:1 (*27*).

1.6 Factors Influencing Rates and Product Distribution

The influence of groundwater characteristics, iron surface treatments, iron purity, and iron surface composition on the rates of degradation of chlorinated compounds, including CT, by Fe^0 has been the subject of several investigations (*4*, *19-26*, *42-45*).

Nevertheless, research on how these factors may alter the distribution of reaction products in the degradation of CT by Fe^0 has not been undertaken.

1.6.1 Effect of Groundwater Characteristics. Groundwater chemical characteristics (e.g., anions such as bisulfide and bicarbonate, buffering capacity, pH) and microbial activity (e.g., presence of sulfate-reducing bacteria) influence the predominant minerals that can precipitate on Fe^0 PRBs, which in turn could affect reaction rates and products (*19-25*). pH is a key variable in groundwater remediation applications with Fe^0 since it controls processes like precipitation of iron (oxy)hydroxides, iron carbonates, and iron sulfides. Solution pH can also determine the thickness of the oxide layer, the acid-base equilibrium of the iron oxide surface hydroxyl groups, and the production of hydrogen (H_2) due to anaerobic corrosion of iron (*46-47*). pH values as high as 10 have been measured in the vicinity of Fe^0 PRBs used to treat groundwater contaminated with chromium, TCE, and uranium (*48-49*). Analysis of iron samples taken from operating PRBs indicated that precipitates of $FeCO_3$, FeS and iron oxyhydroxides coexist on iron surfaces (*49*). Mineral precipitation may decrease reactive surfaces, iron oxyhydroxides may bind iron grains, and H_2 production may lead to a film of H_2 on iron surfaces, resulting in porosity losses that affect the long-term performance of Fe^0 PRBs (*46*).

Batch and field studies on the transformation of chlorinated and non-chlorinated compounds by Fe^0 have found that the rate constants decrease as pH increases (*4, 50, 51*) possibly due to the precipitation of iron oxyhydroxides that block reactive sites or decrease Fe^0 corrosion rates by forming a protective layer that inhibits the cathodic reaction (*52*). Consistent with this, one study found that the thickness of the iron oxide

layer rather than the amount of ferrous iron (Fe(II)) in the oxide was the predominant factor affecting the rates of CT and nitrobenzene degradation at an iron-oxide coated gold electrode (*53*).

pH may indirectly influence the product distribution and reaction kinetics through the iron surface chemistry and medium characteristics. Iron(oxy)hydroxides that form upon contact of iron metal or iron minerals with water have acid-base characteristics depending on the pH (*47*). At low pH values, iron oxide surface hydroxyl groups are protonated (≡ FeOH) whereas at high pH values, completely deprotonated oxide hydroxyl groups (≡ FeO^-) predominate ("≡" stands for the iron oxide surface). It has been hypothesized that the formation of *cis*–DCE and TCE, the products of TCE and PCE hydrogenolysis, respectively, in Fe^0 and FeS systems, may occur via hydrogen atom abstraction from protonated surface functional groups such as ≡FeSH and ≡FeOH (predominant at pH ≥ 7) (*20*, *54*).

1.6.2 Effect of Iron Surface Treatments. The kinetics of chlorinated organic compounds degradation by Fe^0 depends on iron surface preparation and conditioning (*36*). A study on transformation of CT by Fe^0 reported enhanced reaction rates by using iron grains pretreated with acid (*4*). Acid washing dissolves nonreactive oxide or organic coatings deposited on the iron surface, leaving clean metal. In addition, increased surface area due to corrosion pits may also contribute to the greater reactivity of the chlorinated compounds with acid-washed iron. Evidence of induced pitting on the surface of iron, as one of the possible techniques to enhance the rates of TCE degradation, is the main subject of an article by Gotpagar et al. (*42*). In that research, it was found that

pretreatment of the iron surface with chloride (Cl^-) ions improved TCE initial degradation rates; the improvement was attributed to the increased roughness of the iron surface due to crevice corrosion, a type of localized corrosion, obtained by pretreatment. Spectroscopic evidence suggests that crevices, which are cracks in the oxide layer that may result from its breakdown by aggressive anions (e.g., Cl^-), are at least one kind of reactive site in the transformation of CT (*55*).

Generation of FeS precipitates on Fe^0 surfaces has been carried out to examine the impact of the Fe^0/FeS system on the degradation rates of TCE. A significant enhancement in the rates of TCE degradation in Fe^0/FeS systems has been documented (*20*, *45*). The reducing properties of FeS may explain the increased reactivity in Fe^0/FeS systems as suggested by Lipczynska-Kochany et al. (*19*) in their work about the aerobic degradation of CT in the presence of Fe^0, Fe^0/FeS, and Fe^0/FeS_2. In situ generation of FeS precipitates on Fe^0 PRBs to accelerate contaminant degradation reaction rates has been suggested (*20*). Implementation of this alternative, however, relies on a better understanding of the reaction products expected in such systems and on whether these products are more toxic or persistent than the parent compound.

1.6.3 Effect of Iron Purity. Different commercial iron metals (i.e., electrolytic vs cast) that vary in composition and types of impurities have been used to study the kinetics of degradation of chlorinated compounds (*1, 4, 17-26, 34-36, 42-46*). Cast irons produced by high-temperature reduction of the ore (i.e., hematite (α-Fe_2O_3) and limonite ($Fe_2O_3 \cdot 3H_2O$)) by coke, a coal-derived carbon, contain substantial amounts of carbon (C),

silicon (Si), and manganese (Mn) and are relatively inexpensive, whereas irons produced by electrolysis are more pure and more expensive.

Carbide, in which single carbon atoms are bonded to an iron lattice, and graphite, a separate phase of crystalline carbon, were identified as the major forms of carbon in cast commercial irons (e.g. Fisher filings – 40 mesh and Master Builders iron filings) (*56*). Burris et al. (*57*) studied the sorption and reduction kinetics of TCE and PCE in the presence of a commercial cast iron (Fisher filings-40 mesh). They found that the bulk of TCE and PCE sorption was to nonreactive sites such as carbon impurities that sequester the contaminant from the reduction reaction. In addition, their results indicated that the aqueous concentration of the contaminant appeared to be the portion of the total concentration that was available for reduction. Interestingly, Arnolds and Roberts (*54*) suggested that cast and electrolytic irons might possess different reactivity towards TCE because of the difference among the yields of vinyl chloride (VC) resulting from the transformation of TCE by irons of distinct purities.

The selectivity and rates of chlorinated contaminant reduction at Fe^0 surfaces could be influenced by the presence of transition metal impurities such as copper (Cu), chromium (Cr), and Mn that exhibit catalytic properties, potential reactive and nonreactive species (e.g., S, Si, and C), and oxide coatings (Si, Mn, and Fe oxides) because reductive dechlorination is a surface-mediated reaction (*4*, *17, 58*). For instance, in one study, trichloroethylene (TCE) degradation did not occur at high purity iron surfaces (*45*), whereas the presence of bulk sulfur and addition of sulfide species (Na_2S, NaHS) enhanced the rates of TCE and CT degradation by Fe^0 (*19-20, 45*). Impurities are also expected to influence the extent of iron corrosion, which in turn may affect the rates

of contaminant reduction. Localized corrosion can occur when two different metals are in contact; for example, at a bimetallic Mn-Fe^0 spot on a Fe^0 particle, corrosion of Fe^0 can be hindered since Mn is more electropositive than Fe^0, making Mn sites become preferential anodes, protecting Fe^0 against oxidation (*59*). Currently, research on how different kinds of Fe^0 may alter the distribution of reaction products in the transformation of chlorinated organic compounds has not been conducted. This is an important topic to address since cast irons are the preferred choice in groundwater remediation with PRBs due to their low cost.

1.6.4 Effect of Iron Surface Composition. An oxide layer covers iron metal exposed either to air or to aqueous environments. Since reductive dehalogenation of chlorinated solvents by Fe^0 is a surface-mediated process, the role of the oxide layer in such processes has been the subject of several investigations (*52*). Spectroscopic analyses of air-exposed commercial iron reveal that the oxide layer consists of two main phases: an inner layer of magnetite (Fe_3O_4), a Fe(II)/Fe(III) oxide, and an outer layer of maghemite (γ-Fe_2O_3), a Fe(III) oxide (*60*). In aqueous systems, however, ferrous hydroxide ($Fe(OH)_2$), the first corrosion product of Fe^0, is the precursor of magnetite and maghemite. Green rusts, or mixed valent Fe(II)/Fe(III) salts, are considered intermediates in the formation of magnetite at neutral pH. Since green rusts are stable only at low reduction potentials, their oxidation commonly leads to γ-Fe_2O_3 or lepidocrocite (γ-FeOOH), which passivates the surface or inhibits corrosion. On the contrary, magnetite is not a passivating oxide because it behaves as a semiconductor material (*61*).

Although the discussion above focused on the possible types of oxides that may form in the aqueous corrosion of iron, dissolution of the oxides initially covering the

metal may occur upon immersion in water. Dissolution refers to the detachment of metal species from the surface of the crystalline lattice into the solution. In fact, Stumm (*47*) points out that water, H^+, OH^-, ligands (surface complexing structures), and reductants and oxidants (in the case of reducible or oxidizable minerals) are the most important species participating the dissolution of solid minerals. In groundwater systems, however, metal cations (e.g., Cr^{3+}) and polymeric molecules (e.g., fatty acids, humic acids) may inhibit the oxide layer dissolution by adsorbing to Fe(II) surface groups.

Natural mineral oxides and the (oxy)hydroxides on Fe^0 carry positive or negative charge depending on pH (*47*). Consequently, sorption of metal cations (e.g., Fe^{2+}) is likely to take place at negatively charged sites. Klausen et al. (*62*) showed that increasing the sorbed concentration of ferrous iron (Fe(II)) on mineral surfaces (magnetite and goethite) increased the rate of reduction of nitroaromatic compounds (NACs). It was concluded that sorbed Fe(II) on minerals is a powerful reductant effecting the transformation of NAC. Given that mineral oxides of the type used in that investigation make up the oxide layer of iron metal used in remediation applications, it was suggested that sorbed Fe(II) on the iron metal oxide layer could be responsible for the reduction of polyhalogenated alkanes (*62*).

In order to get insight into the role of the oxide layer on the rates of CT reduction by oxide-covered Fe^0, Johnson et al. (*34*) carried out CT transformation in the presence of several ligands. Cathechol, ascorbate, and oxalate, which form mononuclear surface complexes with metal cations, and borate, which forms binuclear complexes, decreased the overall rate constant for CT transformation. Conversely, chloride, which depassivates the iron oxide layer, increased the rate constant for CT disappearance. The decrease in the

rate constants was explained by the fact that all the tested ligands formed inner-sphere complexes with the reactive sites (Fe(II) centers), thus blocking the access of CT to those sites. Then, it was inferred that formation of a precursor complex, presumably an outer sphere complex, between CT and the reactive sites is a requirement for reduction of CT to take place. It was also stated that metal ions (e.g., Cr^{3+}) might constrain the reduction of chlorinated solvents by Fe^0.

Pecher et al. (*63*) examined the degradation of CT and dibromodichloromethane (CBr_2Cl_2) in suspensions of Fe(II) and goethite at fixed pH. At low pH values, increasing the concentration of sorbed Fe(II) resulted in a change in the product distribution and increased the reaction rate constant for the contaminants' disappearance. In the case of CT, the ratio of CF to HCOOH was found to decrease with increasing surface coverage of Fe(II) on oxide surfaces. However, this trend was not observed at high pH where formation of green rusts from the homogenous ferrous iron solution occurred. In this system, CF was the main product of the reaction accounting for 90% of the mass balance. Thus, it was deduced that the speciation of the reactive ferrous iron centers at the oxide surface might dictate which pathway (i.e., dihaloelimination vs hydrogenolysis) predominates in the transformation of polyhalogenated alkanes.

Finally, Balko and Tratnyek (*38*) cited that more negative reduction potentials of the reductant, the use of iron alloys, which increase the number of defects in the oxide layer, and increasing the concentration of Fe(II) surface sites on the oxide layer may enhance the rate of CT degradation. The enhancement in degradation rates could possibly be due to increased rates of electron transfer via electron tunneling through the oxide

layer and defects such as crevices to CT or to the presence of highly reducing Fe(II) sites on the iron oxide surface (*38*).

Therefore, factors such as pH, the presence of Fe(II) sites on the oxide layer, the presence of defects (e.g., crevices), the presence of impurities (e.g., sulfur), iron surface precipitates of FeS and $FeCO_3$, iron oxide composition, and sorbed metallic cations (e.g., Mn^{2+}) are expected to influence which pathway (dichloroelimination vs hydrogenolysis) predominates in the transformation of CT by Fe^0.

1.7 Electron Transfer Theories

Although reductive dechlorination of CT and other halocarbons by iron surfaces was shown as an electrochemical process (eqs 1.1 and 1.2), Matheson and Trantyek (*4*) postulated three different mechanisms that could explain reduction of halogenated solvents: (i) direct electron transfer from iron metal at the metal surface; (ii) reduction by Fe (II), which results from corrosion of the metal; and (iii) reduction catalyzed by the molecular hydrogen that is formed from reduction of water during anaerobic corrosion.

Scherer et al. (*52*) suggested that, from all mechanisms, direct electron transfer plays the most significant role in the reduction process. As a result, three conceptual models of electron transfer were proposed (i) direct electron transfer from the bare metal exposed to solution at pits in the oxide layer, where the source of electrons is the corrosion of Fe^0 or electron tunneling; (ii) electron transfer from the conduction band of the iron oxide covering Fe^0, with the oxide possibly behaving as a semiconductor; and (iii) reduction by sorbed or lattice Fe(II) surface sites (*52*). Balko and Tratnyek (*38*) investigated the role of the oxide conduction band electrons on the reduction of CT by

conducting parallel experiments in the presence and absence of light with Fe^0. They found an increase of the pseudo-first order reaction rate constant for CT disappearance in the presence of light compared to the rate constant for the experiment carried out in the dark; however, the estimated rate constant due solely to the effect of light (k_L) was one third of the rate constant associated in the dark (k_D). In addition, in the presence of light, there was a shift in the product distribution towards more completely dechlorinated products that may originate from the hydrolysis of a dichlorocarbene intermediate; the shift was attributed to the oxide photogenerated conduction band electrons. Since the photogenerated conduction band electrons gave different reaction products, the authors concluded that conduction band electrons were not responsible for CT reduction in the dark. Instead, direct electron transfer via tunneling or defects in the oxide layer as well as reduction by Fe(II) sites on the oxide layer were postulated to be the mechanisms responsible for CT transformation.

Li and Farell (*41*) showed that the CT reduction rate at an oxide-free Fe^0 electrode was limited by the rate of outer-sphere electron transfer. Direct electron transfer, possibly via electron tunneling, was suggested to be the mechanism explaining CT reduction in this system. It was also hypothesized that chloroalkanes (e.g., CT) may predominantly undergo sequential dechlorination and produce chlorinated products because their interactions with the iron surface are weak (i.e., mainly by physical adsorption), brief, and electrons are transferred one at a time.

1.8 Surface Characterization Techniques

Surface characterization techniques have become useful tools when attempting to study the role of solid surfaces on the reduction of aqueous contaminants. Techniques such as X-ray photoelectron spectroscopy (XPS) and scanning electron microscopy (SEM) allow the characterization of materials in terms of their surface and morphological features. A brief discussion of the XPS and SEM techniques follows.

1.8.1 X-ray photoelectron Spectroscopy (XPS). XPS was the first vacuum-based surface chemical analysis technique to be developed. In XPS, a sample is bombarded with soft X-rays, generally AlKα or MgKα rays, which causes electrons to be ejected from core levels of the sample. The energy of the emitted photoelectrons is then analyzed by an electron spectrometer and the data presented as a graph of intensity (or counts per second) vs binding energy (eV), a graph known as the photoelectron spectrum. The binding energy is the parameter employed to describe the energy of an electron from a specific core of an element. Thus, the photoelectron spectrum of a sample enables the identification of the elements present and their chemical oxidation state as well as the calculation of the surface atomic composition. Analysis depth ranges from a few to more than 100 Angstroms (Å), depending on the type of sample, the energy of the photoelectron measured, and the instrumental setup. XPS can also provide compositional information as a function of depth by means of destructive and nondestructive depth profiling methods (*64*).

1.8.2 Scanning Electron Microscopy (SEM). SEM is widely used for the study of grain shapes and the physical characteristics of solid surfaces. It has a broad magnification range capable of image resolution from light microscope capabilities down into the neighborhood of 10 to 20 Å. In SEM, a highly focused electron beam, with accelerating potential between 3 and 20 kV, scans a sample surface. The bombarding electrons interact with the sample producing backscattered primary electrons (high-energy electrons), secondary electrons (those from the sample), and Auger electrons. The SEM detector measures the flux of low-energy electrons that originate from the valence and conduction bands of the near-surface atoms. Secondary electron production is a function of composition and the angle at which the incident beam strikes the surface. Contrast in a typical SEM image is attributed to secondary electron production along with the shadowing effects on rough surfaces (*65*).

Emission of backscattered electrons is the basis for backscattered electron imaging (BEI). BEI is well suited for imaging specimens that consist of phases with different atomic composition. The element of higher atomic number will show stronger emission, resulting in brighter areas on the screen, which permits one to distinguish the phases.

1.9 Research Hypothesis

Hypothesis: Solution pH, iron purity, precipitates of FeS and $FeCO_3$, cations such as Mn(II), and the types of iron oxides on the surface of Fe^0 are expected to affect not only rates, but also the products of chlorinated organic compounds transformation because the

reduction potential, electron donating capacity, structure and morphology of the Fe^0 surface depend on these variables.

Identifying experimental conditions that enhance the rates of CT transformation and lead to benign products is desirable for a better design of Fe^0 PRBs. The goal of this research was to get a better understanding of the factors that may influence rates and products, so that recommendations about how to manipulate Fe^0 surface properties, either in situ or ex situ, and how to choose the type of Fe^0 for groundwater remediation could be made. In addition, understanding how the groundwater chemistry affects rates and products is necessary for a more realistic assessment of the fate of chlorinated contaminants in Fe^0 PRBs.

Anaerobic batch experiments were conducted to study the kinetics of CT reduction and product formation in Fe^0 systems. Specific tasks included:

1. CT reduction experiments with four as-received commercial iron metals, two electrolytic and two cast irons, for at least two different pH values.
2. CT reduction experiments with Peerless Fe^0 in the pH range from 7 to 12.9. Peerless Fe^0 was chosen to conduct CT degradation over a wide range of pH because it is a cast Fe^0 commonly used in groundwater remediation. The pH range 7-12.9 was selected in order to (1) simulate the pH values expected to occur in the vicinity of Fe^0 barriers and, (2) assess whether the solubility and types of oxides covering Peerless Fe^0 had any influence on rates and products.
3. CT reduction experiments with acid-washed irons at pH 7.
4. Generation of coatings of $FeCO_3$, FeS, and sorbed Mn(II) on a high purity Fe^0, Fisher Electrolytic with a content of metallic iron greater than 99%, to conduct

CT reduction experiments with these pretreated irons pH 7. A high purity Fe^0 was chosen to carry out the pretreatments in order to better determine the effects of these pretreatments on rates and products without being concerned about the background contribution of potential impurities such as S and C, which are present in low purity Fe^0.

5. Performance of XPS analyses on selected Fe^0 surfaces to characterize them in terms of their content of impurities, oxidation state of iron in the surface oxides, and thickness of the oxide layer.
6. Performance of SEM microscopy analysis on selected Fe^0 samples to obtain information about their morphology (i.e., oxide layer thickness and extent of oxidation).

2. MATERIALS AND METHODS

2.1 Iron Metals and Chemicals

Electrolytic irons (99% and 93.3% purity) and 40 mesh cast iron filings were obtained from Fisher Scientific (Fairlawn, NJ). Peerless cast iron was supplied by Peerless Metal Powders and Abrasives (Detroit, MI). Average specific surface areas measured by single point BET with a Flowsorb II 2300 (Micromeritics, GA) were 0.195 ± 0.0195, 0.089 ± 0.027, 7.42 ± 0.2, and 1.785 ± 0.069 m^2/g for Fisher Electrolytic (FE) 93%, FE 99%, Fisher Filings 40 (FF-40) mesh, and Peerless irons, respectively. Uncertainties in these surface area values represent 95% confidence intervals calculated from four replicate measurements. Qualitative examination of the four iron metals with electron probe X-ray microanalysis–wave-length dispersive spectrometry (EPMA-WDS) was conducted on a Cameca SX50 electron microprobe. The electron beam operated at an accelerating voltage of 20 kV and a current of 100nA. Scanning of a 20-μm diameter spot in each sample was performed over nearly the full range of WDS motion using LiF, PET, TAP, and PC1 diffraction crystals, which together cover essentially the complete wavelength from C to U. The backscattered electron imaging capabilities of the electron microprobe were used to obtain micrographs of untreated iron samples. Bulk chemical composition of the metals was determined by Inductively Coupled Plasma/Atomic Absorption Spectroscopy (ICP/AA) (Arrow Laboratory Inc., Wichita, KS).

All reagents were ACS grade and all aqueous solutions were prepared with nanopure water (18 MΩ·cm resistivity, Barnstead Ultrapure Water System, IA). The following Good's buffers (*66*) (0.05 M) were used for pH control (7 < pH < 10.5): N-[2-

hydroxyethyl]piperazine-N'-[2-ethanesulfonic acid] (HEPES) for 7< pH < 8.4, N-cyclohexylamino-ethanesulfonic acid (CHES) for 8.4 < pH < 9.3, and 3-cyclohexylamino-1-propanesulfonic acid (CAPS) for pH = 10.2. Sodium hydroxide solutions were used for pH values greater than 12. The ionic strengths of the buffer solutions were 0.012 M, 0.04 M, 0.006 M, 0.025 M, 0.02 M, 0.02 M, and 0.1 M for the pH 7 with HEPES, pH 8.4 with HEPES, pH 8.4 with CHES, pH 9.3 with CHES, pH 10.2 with CAPS, pH 12 with 0.02 M NaOH, and pH 12.9 with 0.1 M NaOH solutions, respectively. CT stock solutions (33 – 37 mM) were prepared in methanol sparged with 99.998% purity nitrogen. Recipes for the preparation of the buffer and methanolic CT solutions used in this work are given in Appendix A. Aqueous solutions were deoxygenated with ultra high purity nitrogen (99.999%) and then placed inside an anaerobic glovebox (Coy Laboratory Products, Inc., Grass Lake, MI) with a catalytic oxygen removal system (atmosphere 97% N_2, 3% H_2).

2.2 Kinetic Experiments

Batch experiments were conducted in 8-mL vials containing 152 g/L of Fe^0 and 7.8 mL of pH buffer (or NaOH solution for pH ≥ 12). This resulted in essentially no headspace. Vials were spiked with the CT stock solution to give an initial aqueous concentration of 0.33-0.37 mM and 1 % v/v in methanol. A step-by-step procedure describing how to set up a typical kinetic batch experiment is provided in Appendix A.

Selected CT degradation experiments were done by using a saturated solution of CT (4×10^{-3} M) prepared in nanopure water. These experiments were done to assess

possible effects of the buffer and methanol on the product distribution as well as to yield $HCOO^-$ concentrations well above detection limits of the ion chromatograph.

CT degradation experiments were also done with FE 99% equilibrated overnight in 1 mM solutions of NaHS, $NaHCO_3$, and $MnBr_2$ and with all four acid-washed irons at neutral pH. Iron metals were acid-washed for 20 minutes with 1 M HCl and Cl^- residuals were removed by rinsing 10 times with deoxygenated nanopure water. Blank and control vials containing Fe^0 and no CT, and no Fe^0 but CT, respectively, were also prepared, so that background Cl^- coming from the metal could be measured and to ensure that significant CT loss due to volatilization was not occurring. All oxygen-sensitive procedures were carried out inside the anaerobic glovebox. Spiked vials were crimp-sealed with a Teflon-coated stopper and aluminum crimp seal, placed in an incubator at 25 °C in the dark and mixed on a rocking platform shaker.

At regular time intervals, vials were centrifuged and then sacrificed to measure CT, CF, Cl^- and $HCOO^-$. The volume ratio of extraction solvent (isooctane) to aqueous solution was 40 so that 25 μL of sample were extracted in 1000 μL of isooctane. For some experiments, samples were also prepared for analysis of CO and CH_4. These samples were prepared in 60-mL vials with the same Fe^0 mass loading (152 g Fe^0/L solution) as the 8-mL vials, and zero headspace. At sampling times, an 18 mL aliquot of the aqueous supernatant from these vials was transferred to a 22-mL vial that was rapidly capped with Teflon-coated septum, crimp-sealed and allowed to equilibrate at room temperature for a 2-hour period to allow partitioning of CO and CH_4 between the aqueous and gas phases. Then, 500 μL of the headspace was manually withdrawn with a gas-tight syringe and injected into the GC-TCD. Duplicate 22-mL vials were sampled at each

reaction time. Kinetic data for the transformation of CT were collected over the course of 2 – 3 half-lives.

2.3 Analytical Methods

Chlorinated compounds were quantified by GC-ECD on a Shimadzu GC-17A equipped with a J&W Scientific DB-624 capillary column (30 m × 0.53 mm × 3 μm). The method used direct injection of 1 μL of sample. The oven temperature program was isothermal at 40 °C for 2 minutes, ramped at 5 °C/min to 55 °C, and isothermal at 55 °C for 2 minutes. Cl^- and $HCOO^-$ were measured by ion chromatography using a Dionex LC20 instrument with a Dionex AS11 column and a ED50 conductivity detector. The analytical method used NaOH gradient elution thus: 0.5 mM NaOH for 2 min, ramp NaOH concentration from 0.5 to 5.0 mM over 3.5 min, and finally increase NaOH concentration from 5 to 38 mM over 12 min. The eluent flow rate was 2 mL/min and the sample loop volume was 10 μL (*67*).

The concentrations of CO and CH_4 were measured on a GC-TCD with a J&W HP-molesieve column (30 m × 0.321 mm × 12.00 μm). Oven and detector temperatures were 40 °C and 110 °C, respectively; the split ratio was 30:1, and Helium as the carrier gas. Gas mixtures of 4.5% CO (v/v) in N_2, and 1000 ppm and 10% of CH_4 (v/v) in N_2 were purchased from Scott Specialty gases (Plumsteadville, PA) and used to prepare calibration standards. These standards were prepared by injecting known volumes of the gases into the headspace of the 22-mL vials that had been crimp-sealed after addition of 18 mL of buffer solution, allowing the samples to equilibrate and then sampling the headspace. At least five standards for each compound of interest were used to prepare a

calibration curve. Details on the preparation of standards for GC and IC analysis are given in Appendix A. Moreover, sample chromatograms of the compounds measured in this work are presented in Appendix B.

2.4 X-ray Photoelectron Spectroscopy (XPS) and Scanning Electron Microscopy (SEM) Analyses

SEM and XPS analyses were done on untreated irons and Peerless Fe^0 filings equilibrated in pH 7 and pH 9.3 anoxic buffers for a 24-h period to characterize their morphology and atomic surface composition. The pH-equilibrated filings were dried by mild heating on a hot plate inside an anaerobic glovebox before analysis. We analyzed Peerless Fe^0 filings because their coarser size made it possible to prepare cross-sections for SEM analysis. Coarse iron filings were embedded in a commercial resin (Embed 812 – DER 736, Electron Microscopy Sciences, Fort Washington, PA), machined on a lathe to have a flat base surface, and polished with diamond lapping films (Allied, High Tech Products, Inc., Rancho Dominguez, CA) of different grit sizes ranging from 30 μm to 1 μm to ensure a smooth finish for adequate optical reflection. Once polished, the cross sections were covered with a conductive layer of either carbon or gold-palladium and analyzed with SEM (ETEC Autoscan) both in the secondary and backscattered modes. Images were collected with a beam potential of 15 or 20 kV.

Atomic composition as function of depth was measured by XPS depth profiling analysis. Samples were analyzed with a Physical Electronics PHI 5800 X-ray photoelectron spectrometer operating under vacuum ($2x10^{-9}$ Torr). Fe^0 samples were mounted on a sample holder by pressing them against adhesive graphite tape inside the glovebox. An air-tight transfer device was then used to transfer the samples from the

glovebox to the XPS vacuum chamber. Once inside the XPS vacuum chamber, surfaces were irradiated with monochromatic Aluminum Kα x-rays (1486.6 eV) of 350 W and analyzed at an electron take-off angle of 45 ° with respect to the plane of the sample. Survey scans in the binding energy range from 50 – 1150 eV were used to identify all detectable elements on the samples. Next, detailed scans were obtained for the major elements detected in the survey scan (C, Fe, O, S, Si, Mn, N) in order to estimate surface atomic composition. A 800-μm spot size and 23 eV pass energy were used for the analysis. Binding energies were corrected by reference to the C1s line at 284.8 eV for hydrocarbon. Quantification of the surface atomic composition for each element was carried out by integrating the peaks corresponding to each element with the aid of the Shirley background subtraction algorithm, and then converting these peak areas to atomic percentage composition by using the sensitivity factors provided for each element by the PHI 5800 system software.

Depth profiling analysis by Argon ion (Ar^+) sputtering was conducted on the pH-equilibrated Peerless iron samples to estimate the thickness of the oxide layer. The Argon (Ar^+) gun operated at a gas pressure of 15 MPa, ion current of 0.73 μA, accelerating voltage of 500 eV, and sputtering rate of 1 nm/min. Depth profiles were obtained by atomic composition analysis after every 0.2 minutes of sputtering.

3. RESULTS AND DISCUSSION

3.1 Reaction Products and Modeling of CT Reduction Kinetics

Several pathways have been reported for the degradation of CT in abiotic and biotic reducing systems (*3*, *6-15*, *27*) (see Figure 1.1). CF and Cl^- were measured as major products in all of our experimental systems whereas CO and CH_4 formation accounted for a small percentage of the initial amount of CT (CT_0) in the experiments designed to measure these two products (see Table 3.1, rows 1, 2, and 3).

Table 3.1. Product distribution in selected CT - Fe^0 systems

Type of Fe^0	Elapsed time (h)	pH	Buffer	CT_0 (mM)	Products (%)[a]				
					CT remaining	CF	CO	CH_4	$HCOO^-$
Peerless	2.4	7	HEPES	0.37	16	72	ND[b]	< 1	NM[c]
Peerless	20	9	CHES	0.35	1	59	2	1.7	NM
FF- 40 mesh	9	unbuffered[d]	NONE	0.26	9	40	ND	< 2	NM
Peerless	26	unbuffered[d]	NONE	4.0[e]	0	63	NM	NM	< 0.1[f]
FE 99%	26	unbuffered[d]	NONE	4.0[e]	0	77	NM	NM	< 0.1[f]

[a] Mass recovery of compound with respect to initial CT in system. Detection limits for CO, CH_4, and $HCOO^-$ were 10 μM, 4.5 μM, and 4.4 μM, respectively
[b] Not detected
[c] Not measured
[d] Initial pH = 5.2
[e] Aqueous solution does not contain methanol
[f] Percentage of $HCOO^-$ in blank vials (only buffer plus Fe^0) is the same as percentage in CT- Fe^0 systems.

It is possible that the low yields of aqueous CO arise from: (i) adsorption onto Fe^0 (CO is used as an adsorbate in chemisorption studies on Fe^0 (*68*)); or (ii) oxidation to CO_2 by a water-gas shift reaction: $CO + H_2O \rightarrow CO_2 + H_2$ (*69*). $HCOO^-$ was detected in Fe^0 blanks as well as in the reaction vials at the same concentrations. Background $HCOO^-$ in blank vials may come from the reduction of dissolved CO_2 via radical reactions (*70*).

Experiments done in unbuffered systems, in the absence of methanol and at high CT_0 (4×10^{-3} M) (Table 3.1, rows 4 and 5) to measure $HCOO^-$ above its detection limits indicated that this anion is not a major final reaction product in our systems.

Although CO and $HCOO^-$ were not major reaction products, indirect evidence suggests that the unidentified carbon, or carbon not accounted for by the measured chlorinated products, in our systems was completely dechlorinated. Plots of excess free Cl^-, or Cl^- in solution due to pathways other than hydrogenolysis to form CF (pathways a and b in Figure 1.1), vs unidentified carbon at each reaction time were constructed for each experiment (*71*). Mathematically,

$$[\text{Excess Free } Cl^-]_t = [\text{Total } Cl^-]_t - [Cl^-(CF)]_t \qquad (3.1)$$

$$[\text{Unidentified Carbon}]_t = [CT]_0 - [CT]_t - [CF]_t \qquad (3.2)$$

where $[\text{Total } Cl^-]_t$ is the total concentration of Cl^- measured by ion chromatography and $[Cl^-(CF)]_t$ is the amount of Cl^- released to yield CF, which was assumed equal to the amount of CF produced. Dichloromethane (DCM), the product of CF hydrogenolysis (pathway i in Figure 1.1), was not detected in our experiments. Least-squares linear regression of excess free Cl^- vs unidentified carbon for most experiments gave slopes close to four (Table 3.2), indicating that approximately four moles of Cl^- were produced per mole of unidentified carbon. Figure 3.1 shows the linear fit for the FF-40 mesh system at pH 7; plots for the remaining systems are presented in Appendix C. Some slopes in Table 3.2 deviate from 4; this is due to high uncertainty because of scatter in the experimental data.

Table 3.2. Slopes of Excess Free Chloride vs Unidentified Carbon for CT - Fe^0 systems

Type of Fe^0	Pretreatment	pH	Buffer	Slope[a]
FF-40 mesh	None	7	HEPES	4.7 ± 1.0
Peerless	None	7	HEPES	2.4 ± 2.4
FE 93%	None	7	HEPES	2.0 ± 2.0
FE 99%	None	7	HEPES	5.5 ± 1.8
Peerless	None	8.4	HEPES	4.7 ± 0.6
Peerless	None	8.4	CHES	4.0 ± 0.9
FF-40 mesh	None	9.3	CHES	4.0 ± 3.3
Peerless	None	9.3	CHES	4.0 ± 1.0
FE 99%	None	9.3	CHES	1.3 ± 4.0
Peerless	None	10.2	CAPS	3.3 ± 1.4
Peerless	None (0.02 M NaOH)	12	None	3.3 ± 0.9
FE 99%	1 mM NaHS	7	HEPES	4.3 ± 1.4
FE 99%	1 mM $MnBr_2$	7	HEPES	3.9 ± 1.4
FE 99%	1 mM $NaHCO_3$	7	HEPES	2.2 ± 0.6
FF-40 mesh	acid-washed	7	HEPES	3.0 ± 0.8
Peerless	acid-washed	7	HEPES	4.5 ± 1.3
FE 93%	acid-washed	7	HEPES	2.7 ± 0.3
FE 99%	acid-washed	7	HEPES	3.0 ± 1.4

[a] calculated from linear least-squares regression with Microsoft Excel. Values are reported with 95% confidence

CT direct hydrolysis to CO_2 (pathway g in Figure 1.1) is an alternative transformation pathway that also could explain the approximate 4:1 ratio of excess free Cl^- to unidentified carbon (*7*); however, there are no reports of this pathway occurring in similar systems, except for the homogeneous pH-independent hydrolysis of CT with a half-life of 40.5 years (*72*) and the mineralization of CT and dichlorodifluoromethane (CCl_2F_2) to CO_2 at semi-dry mineral surfaces (i.e., alumina, sand, silica gel) under anoxic conditions in the dark (*73*).

Thus, most likely dichloroelimination (pathways c and d in Figure 1.1) followed by hydrolysis of the dichlorocarbene intermediate ($:CCl_2$) is the pathway competing with CT hydrogenolysis to CF in our systems.

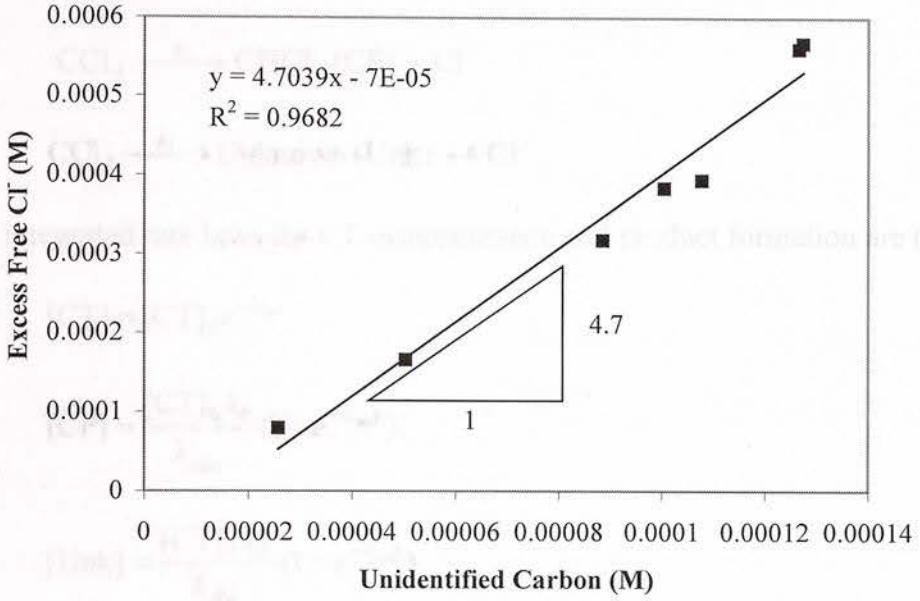

Figure 3.1. Excess Free Cl^- vs Unidentified Carbon for FF-40 mesh Fe^0 system at pH 7

We attempted to measure total organic and inorganic carbon (TOC/TIC) in Fe^0 buffered systems to get insight into the nature of the unidentified carbon fraction (organic vs inorganic); however, the high background carbon concentration of the buffer and methanol (greater than 3000 mg C/L) with respect to the carbon concentration (4.8 mg C/L) from CT_0, prevented us from pursuing further testing. Thus, we hypothesize that the unidentified carbon fraction, hereafter called "unknown" products, consists of low molecular weight organic or inorganic compounds like carbonate species (HCO_3^- and CO_3^{2-}) or organic acids, or short-length hydrocarbons such as ethane, ethane, and

acetylene, which may originate from coupling of carbene/carbenoid species produced by sequential reduction of the dichlorocarbene (*58*).

Based on this hypothesis, we used a pseudo-first order model for parallel reactions to describe the kinetics of CT reduction by Fe^0 (*74*). The two parallel reactions considered were:

$$CCl_4 \xrightarrow{k_1} CHCl_3(CF) + Cl^- \quad (3.3)$$

$$CCl_4 \xrightarrow{k_2} \text{Unknown (Unk)} + 4\,Cl^- \quad (3.4)$$

The integrated rate laws for CT disappearance and product formation are (*74*):

$$[CT] = [CT]_0 e^{-k_{obs}t} \quad (3.5)$$

$$[CF] = \frac{[CT]_0 k_1}{k_{obs}}(1 - e^{-k_{obs}t}) \quad (3.6)$$

$$[Unk] = \frac{[CT]_0 k_2}{k_{obs}}(1 - e^{-k_{obs}t}) \quad (3.7)$$

where k_{obs} is the overall pseudo-first order reaction rate constant for CT disappearance; k_1 and k_2 are the rate constants for the formation of CF and the unknown, respectively. The concentration of the unknown product was estimated with

$$[Unk] = \frac{[\text{Excess Free } Cl^-]}{4} \quad (3.8)$$

This kinetic treatment assumes that

$$k_{obs} = k_1 + k_2 \quad (3.9)$$

Values of k_{obs}, k_1, and k_2 in equations 3.5-3.7 were calculated by nonlinear regression of concentration vs time data using Sigma Plot v. 4.0. The yields of CF and Unk were calculated as follows:

$$\text{CF yield} = \frac{k_1}{k_{obs}} \quad ; \qquad \text{Unk yield} = \frac{k_2}{k_{obs}} \tag{3.10}$$

Examples of the model fits for the untreated Fe^0 systems at pH 7 are presented in Figures 3.2 - 3.5. In these figures the y-axis corresponds to the normalized concentrations of products with respect to the initial concentration of CT and the solid lines represent the nonlinear fits. In general, the model fits the experimental data quite well for all of our systems. Mass recovery in these graphs and the ones that will be presented in the following sections correspond the sum of the concentrations of CT, CF, and the Unknown.

Table 3.3 compiles the kinetic data for all the CT transformation experiments performed in this research. k_{obs}, k_1, and k_2 as well as the yields of CF and Unk are reported with 95% confidence intervals (See Appendix D for details on uncertainty calculations.) In most systems, carbon and chlorine mass balances, i.e., ([CT] + [CF] + [Unk]) and ($[Cl^-]$ + 4 × [CT] + 3 × [CF]), at each reaction time were 90-110% of CT_0 and Cl_0 (4 × CT_0), respectively, indicating that that losses due to physical processes (e.g., sorption and volatilization) were not significant during the course of the experiments. Finally, the concentration of CT did not change with time in the control vials (only CT + buffer), so that the disappearance of CT can be entirely attributed to the reductive capacity of untreated or pretreated Fe^0.

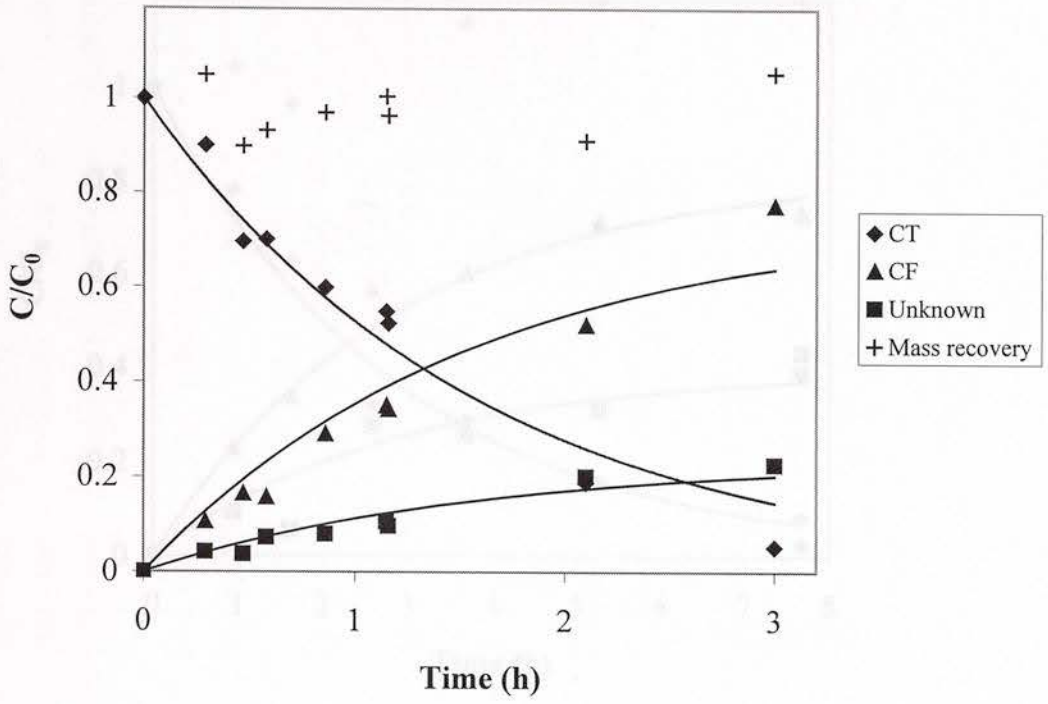

Figure 3.2. CT degradation by Peerless Fe^0at pH 7

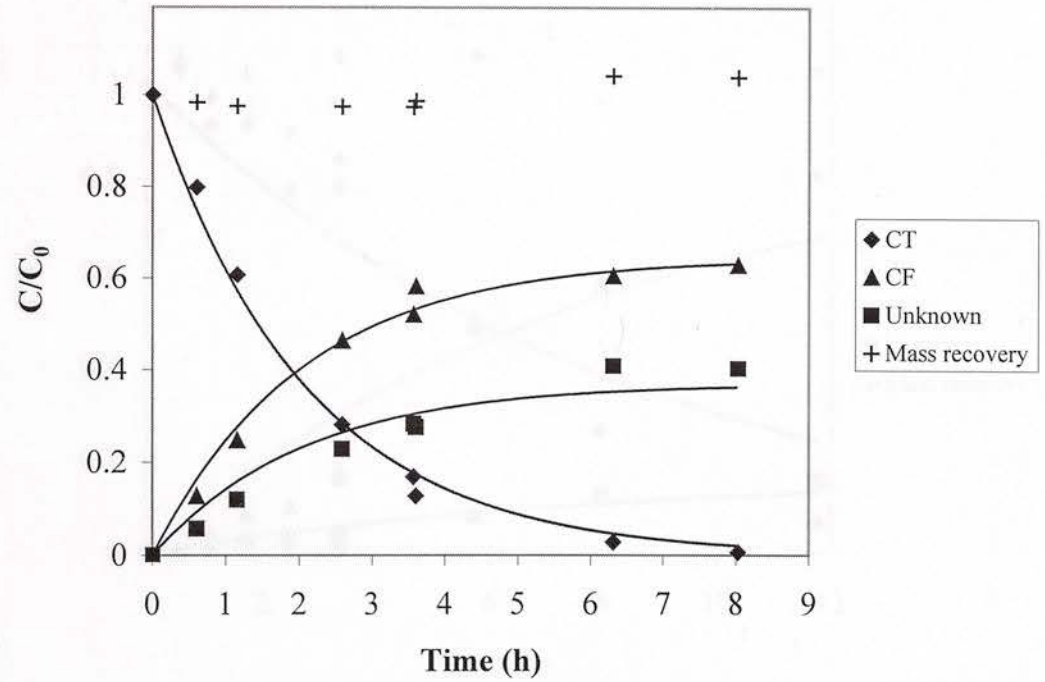

Figure 3.3. CT degradation by FF-40 mesh Fe^0at pH 7

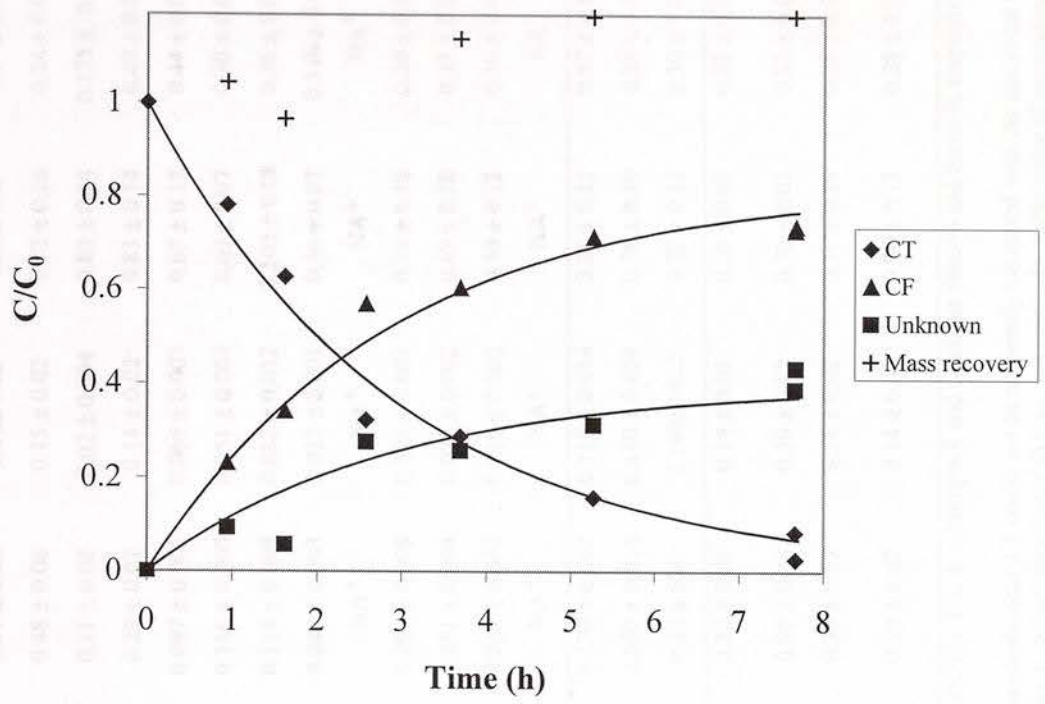

Figure 3.4. CT degradation by FE 99% Fe^0at pH 7

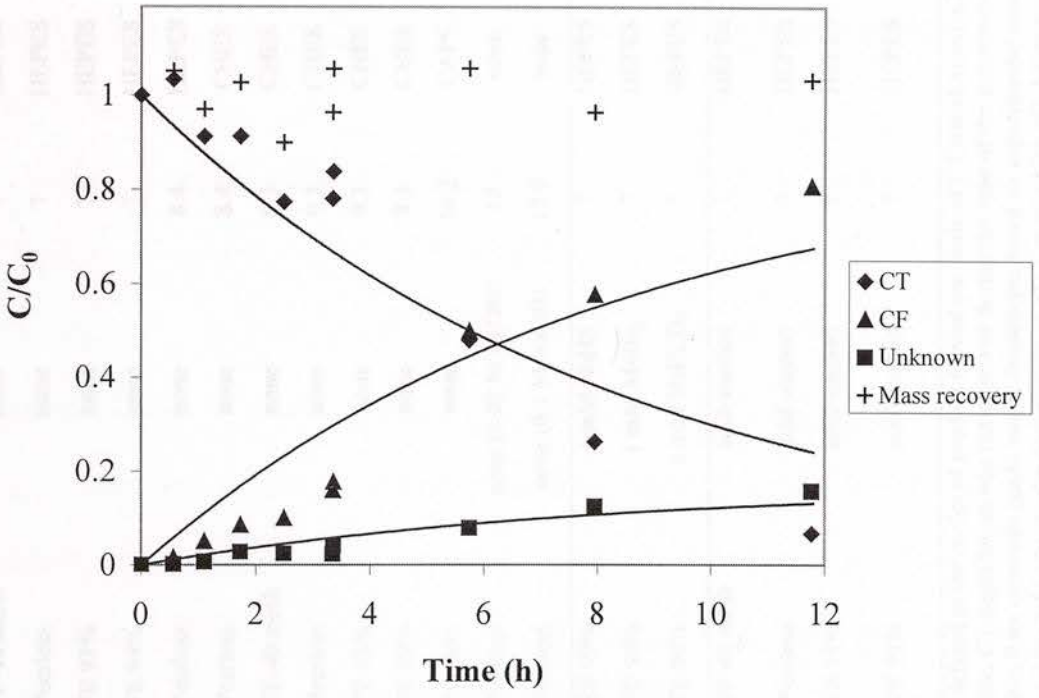

Figure 3.5. CT degradation by FE 93% Fe^0at pH 7

Table 3.3 Summary of kinetic data for CT degradation by Fe^0 under different experimental conditions

Row	Type of Fe^0	Pretreatment	pH	Buffer	k_{obs} (h^{-1})	k_1 (h^{-1})	k_2 (h^{-1})	CF Yield [a]	Unk Yield [a]
1	FF-40 mesh	none	7	HEPES	0.48 ± 0.05	0.31 ± 0.02	0.18± 0.02	0.65± 0.08	0.37± 0.06
2	Peerless	none	7	HEPES	0.64 ± 0.11	0.48 ± 0.06	0.15 ± 0.02	0.72 ± 0.16	0.24 ± 0.05
3	FE 93%	none	7	HEPES	0.12 ± 0.04	0.11 ± 0.02	0.02 ± 0.004	0.89 ± 0.34	0.175 ± 0.07
4	FE 99%	none	7	HEPES	0.35 ± 0.05	0.29 ± 0.02	0.14 ± 0.02	0.83 ± 0.14	0.40 ± 0.09
5	Peerless	none	8.4	HEPES	0.150 ± 0.024	0.097 ± 0.007	0.065 ± 0.007	0.65 ± 0.12	0.44 ± 0.08
6	Peerless	none	8.4	CHES	0.169 ± 0.014	0.116 ± 0.008	0.051 ± 0.004	0.69 ± 0.07	0.30 ± 0.03
7	FF-40 mesh	none	9.3	CHES	0.226 ± 0.029	0.114 ± 0.008	0.082 ± 0.012	0.505 ± 0.08	0.36 ± 0.07
8	Peerless	none	9.3	CHES	0.085 ± 0.009	0.048 ± 0.003	0.027 ± 0.001	0.56 ± 0.07	0.310 ± 0.03
9	FE 93%	none	9.3	CHES	NA [b]	NA [b]	NA [b]	NA [b]	NA [b]
10	FE 99%	none	9.3	CHES	0.128 ± 0.013	0.095 ± 0.008	0.025 ± 0.001	0.74 ± 0.10	0.20 ± 0.02
11	Peerless	none	10.2	CAPS	0.0765 ± 0.01	0.051 ± 0.004	0.022 ± 0.002	0.67 ± 0.10	0.33 ± 0.07
12	Peerless	none (0.02 M NaOH)	12	none	0.0442 ± 0.01	0.022 ± 0.002	0.016 ± 0.002	0.50 ± 0.12	0.36 ± 0.09
13	Peerless	none (0.1 M NaOH)	12.9	none	0.0224 ± 0.002	NA [c]	NA [c]	NA [c]	NA [c]
14	FE 99%	1 mM NaHS	7	HEPES	0.20 ± 0.03	0.130 ± 0.007	0.115 ± 0.014	0.66 ± 0.11	0.57 ± 0.11
15	FE 99%	1 mM $MnBr_2$	7	HEPES	0.46 ± 0.09	0.360 ± 0.016	0.110 ± 0.054	0.78 ± 0.10	0.23 ± 0.12
16	FE 99%	1 mM $NaHCO_3$	7	HEPES	0.45 ± 0.07	0.32 ± 0.01	0.140±0.025	0.72 ± 0.11	0.30 ± 0.07
17	FF-40 mesh	acid-washed	7	HEPES	0.34 ± 0.04	0.22 ± 0.01	0.14 ± 0.01	0.66 ± 0.08	0.42 ± 0.06
18	Peerless	acid-washed	7	HEPES	1.21 ± 0.10	0.95 ± 0.03	0.39 ± 0.02	0.78 ± 0.07	0.32 ± 0.03
19	FE 93%	acid-washed	7	HEPES	0.50 ± 0.13	0.36 ± 0.03	0.14 ± 0.02	0.71 ± 0.19	0.28 ± 0.09
20	FE 99%	acid-washed	7	HEPES	0.50 ± 0.08	0.39 ± 0.02	0.14 ± 0.03	0.78 ± 0.13	0.28 ± 0.07

[a] Yields are defined as the moles of product formed per mole of CT transformed: $CF_t/(CT_0 - CT_t)$, $Unk_t/(CT_0 - CT_t)$; subscripts 0 and t indicate time=0 and time> 0, respectively;
[b] Not available. CT degradation was not observed during the time of the experiment.
[c] Not available. Rate constants could not be determined based on experimental concentration vs time data points since Cl^- could not be accurately measured with the analytical IC method. This is probably due to the decomposition of Cl^- at this high pH. Moreover, the concentration of CF did not increase with time, but reached a stable value of approximately 25% of CT_0 at 28 h, probably due to alkaline hydrolysis at this high pH value over the course of the experiment (duration = 70 h). The half-life for CF alkaline hydrolysis at pH 12.9 is 28 h, based on the homogenous hydrolysis rate constants reported by Jeffers (*72*).

3.2 Effect of Iron Purity and Surface Oxidation on Rates and Products

3.2.1. Effect of Iron Purity on Rates. The four commercial iron metals tested in this study had different total amounts and types of impurities as shown in Table 3.4. Micrographs and EPMA-WDS spectra of the iron metals indicated that these metals contained oxygen as an impurity. As an example, Figure 3.6 shows the backscattered electron image and the WDS spectrum for FF-40 mesh Fe^0. In Figure 3.6a, oxidized regions in Fe^0 particles are represented by a dark gray tone whereas nonoxidized regions appear in a brighter gray tone. Oxygen, however, could not be quantitatively measured by ICP/AA. Thus, the percentage of oxygen reported in Table 3.4 is an approximate value estimated after accounting for all other elements.

Table 3.4 indicates that FE 99% is a high purity Fe^0 with the lowest content of impurities. In contrast, FE 93%, and the cast irons FF-40 mesh and Peerless contain significant amounts of C, Mn, Si, and O as well as traces of transition metal impurities such as Cr, Ni, and Cu.

Surface area normalized rate constants ($k_{obs,SA}$) were calculated for the reduction of CT by the untreated metals at pH 7 and pH 9.3 to compare their reactivity (see Table 3.5). The highest $k_{obs,SA}$ for FE 99% at both pH values indicates that this high purity Fe^0 is the most reactive in transforming CT; $k_{obs,SA}$ values for FE 93%, Peerless, and FF-40 mesh Fe^0 were one to two orders of magnitude lower than that for FE 99%. As a comparison, $k_{obs,SA}$ values for the reduction of TCE by untreated FE 99% and Peerless Fe^0 differed one order of magnitude, with FE 99% being more reactive (*26*). This suggests that the transformation of CT and TCE is similarly affected by the initial condition of the iron surface and bulk composition.

Table 3.4 Bulk composition (wt %) of untreated Fe^0 metals from ICP/AA

Element	Type of Fe^0			
	FF-40 mesh [a]	Peerless [b]	FE 93% [c]	FE 99% [d]
C (Austenitic) [e]	1.13	0.99	0.014	0.009
C (Graphitic)	1.63	2.78	-- [f]	--
Manganese	0.45	0.60	0.37	0.001
Phosphorus	--	0.057	--	--
Sulfur	0.10	0.088	0.009	--
Silicon	1.88	2.10	--	0.019
Copper	0.36	0.20	0.022	0.001
Nickel	0.18	--	--	--
Chromium	--	0.15	0.013	0.001
Molybdenum	--	0.032	--	--
Magnesium	--	--	0.011	--
Aluminum	--	--	0.046	0.003
Vanadium	--	0.016	--	--
Titanium	--	0.015	0.004	--
Iron [g]	89.00	90.00	93.30	99.00
Oxygen [h]	5.00	2.00	6.00	0.00

[a] Brownish gray to gray filings passing a 40 mesh sieve. Elemental composition provided by Fisher is 89% Fe, 3% C, 0.5% S, 0.5% P, 1% Mn

[b] Cast iron aggregate ETI 8/50 in the form of coarse iron filings. Elemental composition provided by Peerless Metal Powders and Abrasives is >90% Fe, 2.5% C, 2.0 % Si, 0.6% Mn, 0.12% S, 0.14% P, 0.20% Ni, 0.20% Cr, 0.15% Mo, 0.20 % Cu.

[c] Fine, gray metallic powder passing a mesh size finer than 100 mesh. 93.3% Fe minimum, 0.02% S, 0.003% N as reported by Fisher

[d] Fine, gray metallic powder. > 99% Fe content as reported by Fisher

[e] Austenitic carbon is a solution of carbon in iron formed at temperatures between 900 and 1400 °C. The maximum solubility of carbon in austenite is 1.7%. Carbon, manganese, silicon are austenite stabilizers.

[f] Not measured

[g] The percentage of iron reported is the value provided by the vendor

[h] Oxygen equals the balance after accounting for all other elements

The trend in $k_{obs,SA}$ values parallels the content of metallic iron of the four metals with FF-40 mesh and FE 99% Fe^0 being the least and most reactive in transforming CT, respectively. Previous studies have suggested that carbon and sulfur impurities may play a significant role in the rates of transformation of chlorinated organic compounds by Fe^0 (*17, 45*).

a

b

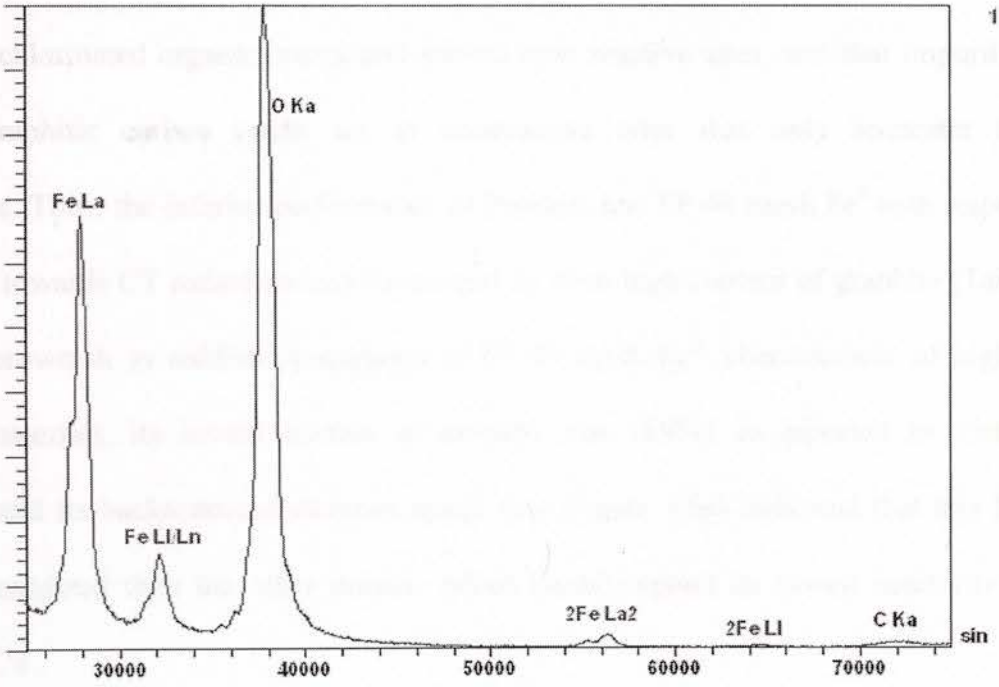

Figure 3.6. (a) Backscattered electron image of FF-40 mesh Fe^0 taken with EPMA; (b) EPMA-WDS spectrum of FF-40 mesh Fe^0 from slow scan on PC1 diffraction crystal, illustrating that significant oxygen is present (O Ka peak).

Table 3.5. Surface area normalized rate constants for CT degradation by untreated Fe^0 metals at pH values of 7 and 9.3

Type of Fe^0	$k_{obs, SA}$ ($L\ h^{-1}\ m^{-2}$) [a]	
	pH 7	pH 9.3
FF-40 mesh	$(4.2 \pm 0.5) \times 10^{-4}$	$(2.0 \pm 0.26) \times 10^{-4}$
Peerless	$(2.3 \pm 0.4) \times 10^{-3}$	$(3.1 \pm 0.35) \times 10^{-4}$
FE 93%	$(4.0 \pm 1.4) \times 10^{-3}$	NA [b]
FE 99%	$(2.6 \pm 0.9) \times 10^{-2}$	$(9.4 \pm 3.0) \times 10^{-3}$

[a] $k_{obs, SA} = (k_{obs} / (SA \times Fe^0 \text{ mass loading}))$; $k_{obs, SA}$, h^{-1}; specific surface area (SA), m^2/g; Fe^0 mass loading = 152 g/L.
[b] Not available. FE 93% Fe^0 did not degrade CT over a 40 h period.

Deng and Hu (*17*) have proposed that reduction rates are proportional to the amount of chlorinated organic compound sorbed onto reactive sites, and that impurities such as graphitic carbon could act as nonreactive sites that only sequester the contaminant. Thus, the inferior performance of Peerless and FF-40 mesh Fe^0 with respect to FE 99% towards CT reduction may be caused by their high content of graphite (Table 3.4). The brownish to reddish appearance of FF-40 mesh Fe^0, characteristic of highly corroded materials, its lowest content of metallic iron (89%), as reported by Fisher Scientific, and its backscattered electron image (see Figure 3.6a) indicated that this Fe^0 was more oxidized than the other metals, which could explain its lowest reactivity in degrading CT.

Sulfur, on the other hand, has been associated with faster rates of TCE reduction in unbuffered, aerobic aqueous systems as reported by Hassan (*45*). In his work, FF-40 mesh Fe^0, which contained 180.5 ppm of S, was more reactive in transforming TCE than 99.9% iron from AlfaAesar (a high purity material with 20.1 ppb of sulfur). However, we

observed the opposite pattern in our systems; increasing the content of sulfur (FE 99% < FE 93% < Peerless < FF-40 mesh) led to slower rates of CT reduction in our buffered systems. This trend may be due to decreasing iron purity for these irons, rather than to sulfur content.

Transition metal impurities such as Cr and Ni present in cast Fe^0 provide corrosion resistance by forming a protective layer of oxide (e.g., Cr_2O_3, NiO) (*59*). As a result, high purity irons are expected to undergo faster initial corrosion and passivation in both air and aqueous unbuffered environments than low purity irons since the former contain only trace amounts of transition metals. Table 3.4 shows that the cast irons, Peerless and FF-40 mesh, had 0.15% Ni and 0.18% Cr, respectively, whereas the electrolytic ones had traces of Cr only, suggesting that transition metals may affect rate constants.

Corrosion of Fe^0 in unbuffered aerobic and anaerobic systems leads to a pH increase due to the reduction of oxygen and water that releases hydroxyl species. Thus, if the magnitude of the initial pH increase is higher for the high purity iron aqueous system, due to the lack of corrosion resistance provided by transition metals, it is possible that the trend observed by Hassan (*45*) in his unbuffered systems is due to pH effects rather than to the sulfur content. High pH values are expected to passivate the iron surface much more than low pH values, so that the contaminant would be slowly transformed, if at all, in the high purity system. In fact, Su and Puls (*26*) reported that pH rose abruptly to a value of approximately 10 in the reduction of TCE by untreated FE 99%, a high purity Fe^0, whereas a more gradual pH increase up to 8.5 was observed in the reduction of TCE by untreated Peerless iron.

3.2.2. Effect of Iron Purity on Products. There is a pattern of higher yields of CF for the FE 99% and 93% Fe^0 systems at pH values of 7 and 9.3 (see Table 3.3 and Figure 3.7), so purity may have some influence on products. The reason for this result is unclear, but as suggested by Balko and Trantyek (*38*), the presence of alloying elements in iron, as in cast irons, may favor dichloroelimination products due to a consecutive two-electron transfer to CT (pathway c in Figure 1.1). In addition, it is possible that the type of predominant surface oxides on FE 99% and cast irons were different at both pH values even though there is no experimental evidence to corroborate this hypothesis. This would affect the distribution of surface oxide protonated and deprotonated hydroxyl groups, which depends on the type of oxide, because different iron oxides exhibit a specific acid-base equilibrium. For example, the pK_{as} for magnetite are $pK_{a1} = 4.4$ and $pK_{a2} = 9.0$, the pK_{as} for goethite are $pK_{a1} = 6.4$ and $pK_{a2} = 9.25$, and the pK_{as} for hematite are $pK_{a1} = 7.3$ and $pK_{a2} = 8.1$ (*75-77*). Thus, at pH $\geq$ 8.1 the proportion of deprotonated surface hydroxyl groups is anticipated to be greater on hematite than on magnetite and goethite because of the differences in pK_{a2} values. Deprotonated surface hydroxyl groups were hypothesized to be good nucleophiles in effecting the reductive dichloroelimination of TCE to chloroacetylene (*20*); consequently, a high proportion of these nucleophiles on the iron oxide surface could favor CT dichloroelimination.

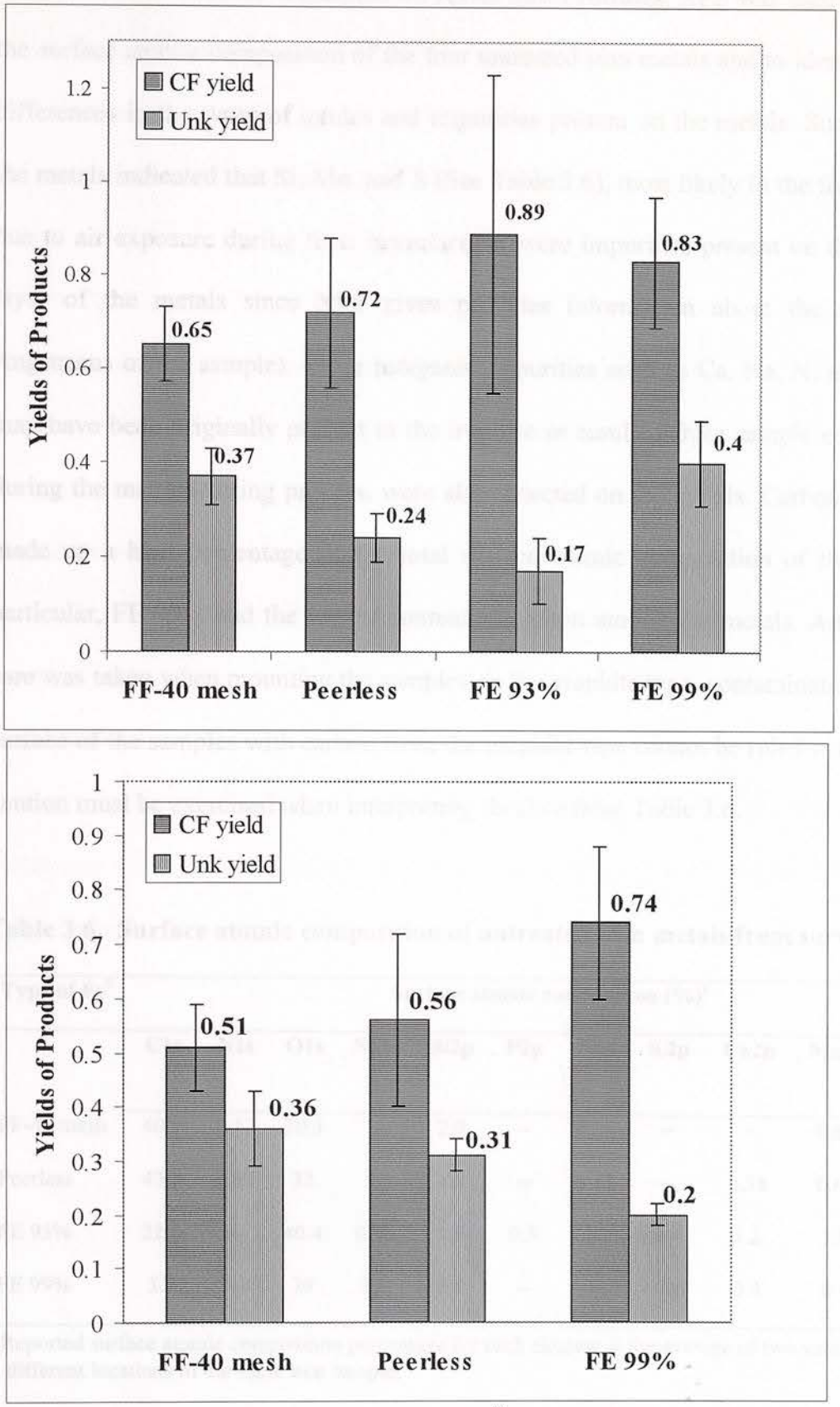

Figure 3.7. Yields of products vs type of Fe^0 for (a) pH 7; (b) pH 9.3

3.2.3. Effect of Surface Oxidation on Rates and Products. XPS was used to determine the surface atomic composition of the four untreated iron metals and to identify potential differences in the types of oxides and impurities present on the metals. Survey scans of the metals indicated that Si, Mn, and S (See Table 3.6), most likely in the form of oxides due to air exposure during their manufacture, were impurities present on the outermost layer of the metals since XPS gives provides information about the top hundred Angstroms of the sample). Other inorganic impurities such as Ca, Na, N, and K, which may have been originally present in the iron ore or resulted from sample contamination during the manufacturing process, were also detected on the metals. Carbon and oxygen made up a high percentage of the total surface atomic composition of the metals. In particular, FE 99% had the lowest content of carbon among the metals. Although strict care was taken when mounting the samples on the graphite tape, contamination of the top surface of the samples with carbon from the graphite tape cannot be ruled out. Therefore, caution must be exercised when interpreting the data from Table 3.6.

Table 3.6. Surface atomic composition of untreated iron metals from survey scans

Type of Fe^0	Surface atomic composition (%)[1]										
	C1s	**N1s**	**O1s**	**Na1s**	**Si2p**	**P2p**	**S2p**	**K2p**	**Ca2p**	**Mn2p**	**Fe2p**
FF-40 mesh	40.7	0.17	30.3	--	2.0	--	0.25	--	--	0.64	25.9
Peerless	43.5	0.07	32	--	1.8	--	0.18	--	0.38	0.67	21.3
FE 93%	22.0	--	40.4	0.94	1.9	0.3	--	0.9	1.2	1.9	30.4
FE 99%	5.5	--	39	3.3	0.8	--	--	0.06	0.4	0.4	50.6

[1] Reported surface atomic composition percentage for each element is the average of two values estimated at different locations of the same iron sample.

Spectra of the iron region of the metals showed that they were similarly covered by Fe(II)/Fe(III) oxides because the binding energies of the Fe $2p_{3/2}$ peak maximum for all four metals ranged from 710.7 to 710.9 eV (see Figure 3.8). Binding energies of 711.3 eV are characteristic of Fe(III) oxides (e.g., hematite (α- Fe_2O_3)) whereas slightly lower values of 710.8-710 eV are indicative of Fe(II) oxides (e.g., magnetite (Fe_3O_4) and wüstite (FeO)) (*78*). In brief, the exact identity of the surface oxides (i.e., whether they are made of maghemite (γ- Fe_2O_3), Fe_3O_4, or α- Fe_2O_3) could not be established from these analyses; a previous study, however, found that both γ-Fe_2O_3 and α-Fe_2O_3 made up the outermost oxide layer of a commercial cast iron, with γ-Fe_2O_3 present in the greatest proportion (*79*).

In summary, the XPS data show that there were not significant differences in the types of iron oxides that made up the oxide layer of the untreated metals, and that impurities such as Si and Mn are present on the outermost surface of the metals. Further research is needed to assess whether the type of oxides covering Fe^0 metals of distinct purity and their oxide layer thickness affect rates and products in the transformation of chlorinated organic compounds.

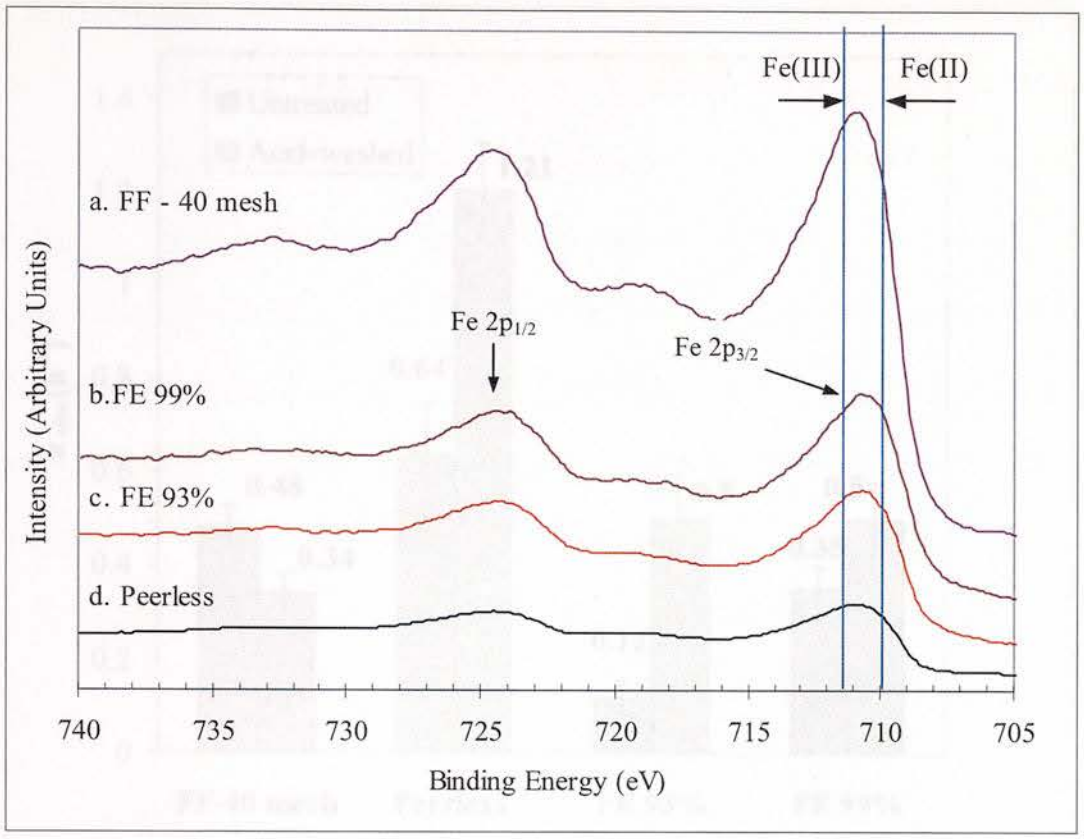

Figure 3.8. XPS spectra of iron region of untreated iron metals. Binding energies for the $Fe2p_{3/2}$ peak of FF-40 mesh, FE 99%, Fe 93%, and Peerless Fe^0 are 710.9 eV, 710.7 eV, 710.7 eV, and 710.9 eV, respectively.

3.3 Effect of Acid-washing Pretreatment on Rates and Products

HCl-washing pretreatment was done to remove oxide layers that could affect reaction rates and products. Note that acid-washing dissolves carbides but not graphitic carbon in Fe^0 as reported by others (*56*). Acid pretreatment increased the k_{obs} values for CT degradation by Peerless, FE 99%, and FE 93% Fe^0 at pH 7, but decreased k_{obs} for CT degradation by FF-40 mesh (see sixth column, last four rows in Table 3.3, and Figure 3.9).

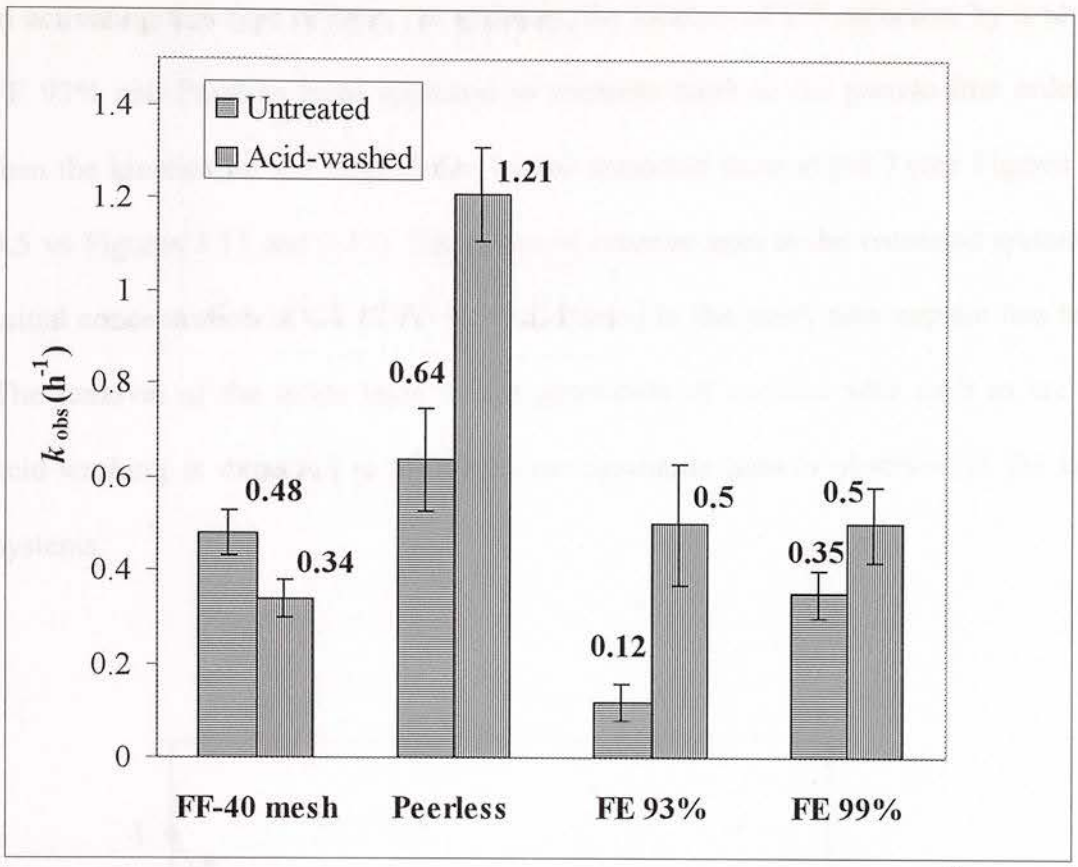

Figure 3.9. Overall rate constants for untreated and acid-washed Fe^0 systems

Figures 3.10-3.13 display the kinetic plots for the acid-washed Fe^0 systems. In general, our results agree with previous studies where faster transformation rates were observed in the reduction of TCE by chloride and acid-treated Fe^0 (*42-44*). Therefore, the enhancement in rates in our systems is most likely due to the removal of nonreactive oxides and/or promotion of pitting corrosion, which increases the density of reactive sites (crevices) on the iron surface. Both of these processes are expected to increase the rate of direct electron transfer from the metal to CT by either eliminating a barrier to electron transfer, due to the removal of the oxide layer, or allowing CT access to the bare metal via crevices (*4, 42, 55*). The k_{obs} value for CT reduction by acid-washed FE 93% was four times the k_{obs} for the untreated FE 93%, indicating that acid-washing was most effective

in activating this type of iron. In addition, the kinetics of CT reduction by acid-washed FE 93% and Peerless irons appeared to conform more to the pseudo-first order model than the kinetics for CT degradation by the untreated irons at pH 7 (see Figures 3.2 and 3.5 vs Figures 3.11 and 3.13). Saturation of reactive sites in the untreated systems at the initial concentration of CT ($CT_0 \sim 0.4$ mM) used in this study may explain this behavior. The removal of the oxide layer or the generation of reactive sites such as crevices by acid-washing is expected to eliminate the saturation pattern observed in the untreated systems.

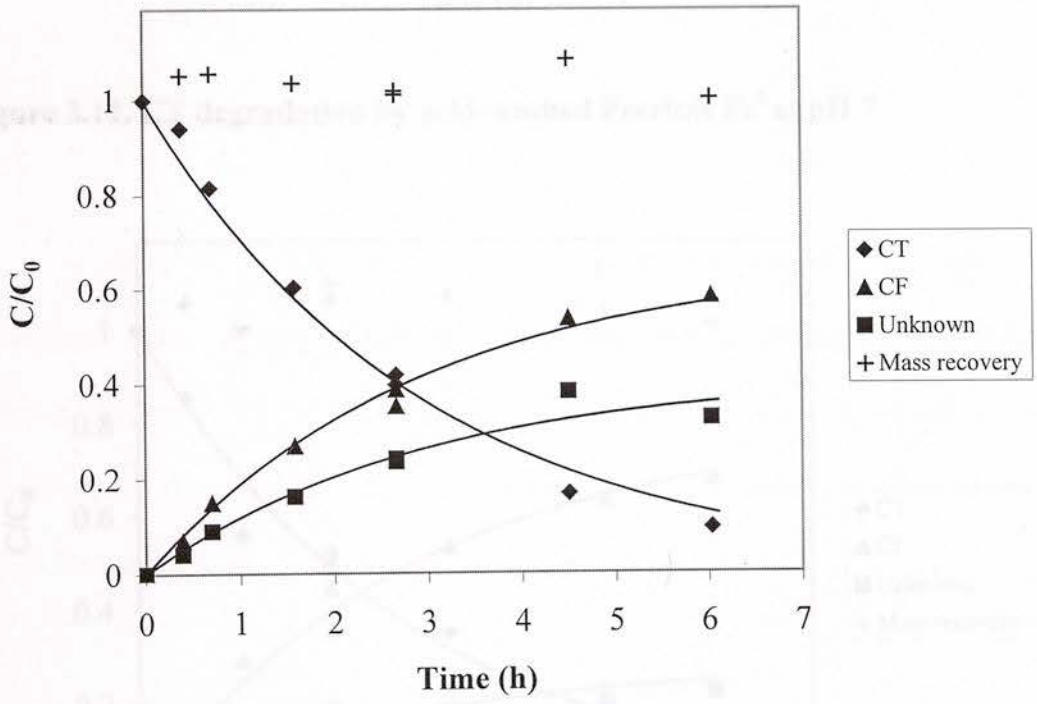

Figure 3.10. CT degradation by acid-washed FF-40 mesh Fe^0 at pH 7

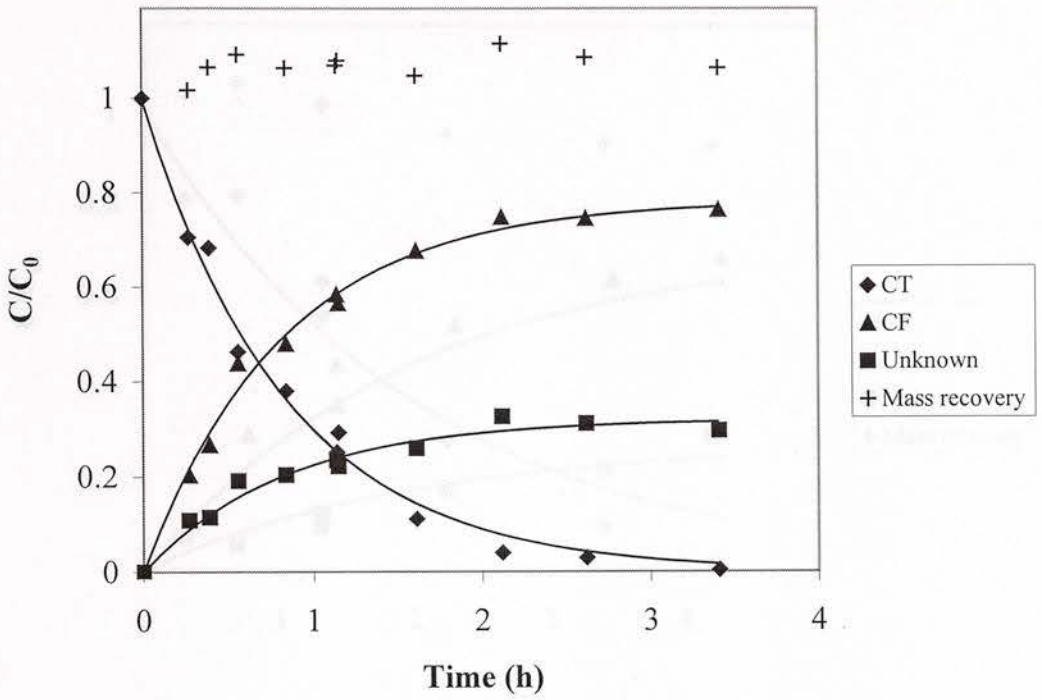

Figure 3.11. CT degradation by acid-washed Peerless Fe^0 at pH 7

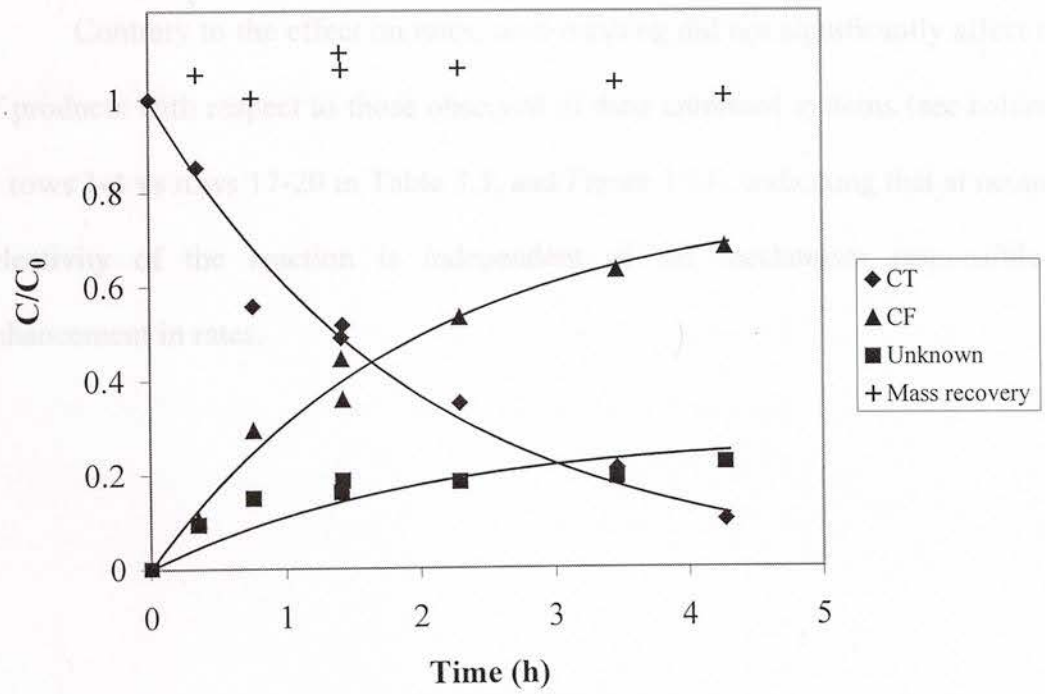

Figure 3.12 CT degradation by acid-washed FE 99% Fe^0 at pH 7

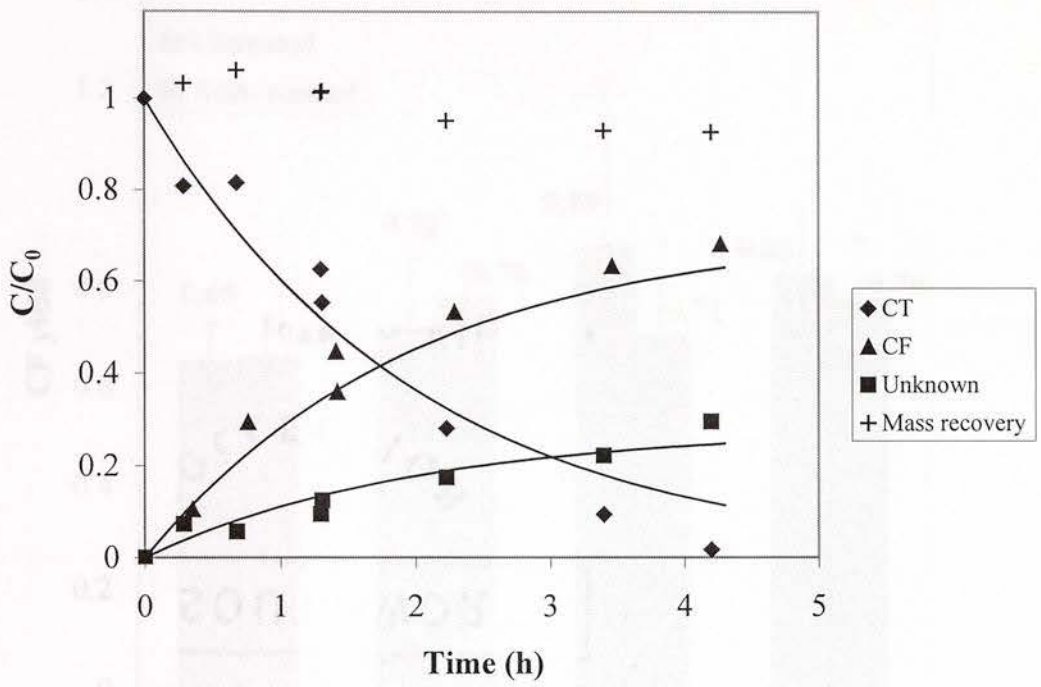

Figure 3.13. CT degradation by acid-washed FE 93% Fe^0 at pH 7

Contrary to the effect on rates, acid-washing did not significantly affect the yields of products with respect to those observed in their untreated systems (see columns 8 and 9, rows 1-4 vs rows 17-20 in Table 3.3, and Figure 3.14), indicating that at neutral pH the selectivity of the reaction is independent of the mechanism responsible for the enhancement in rates.

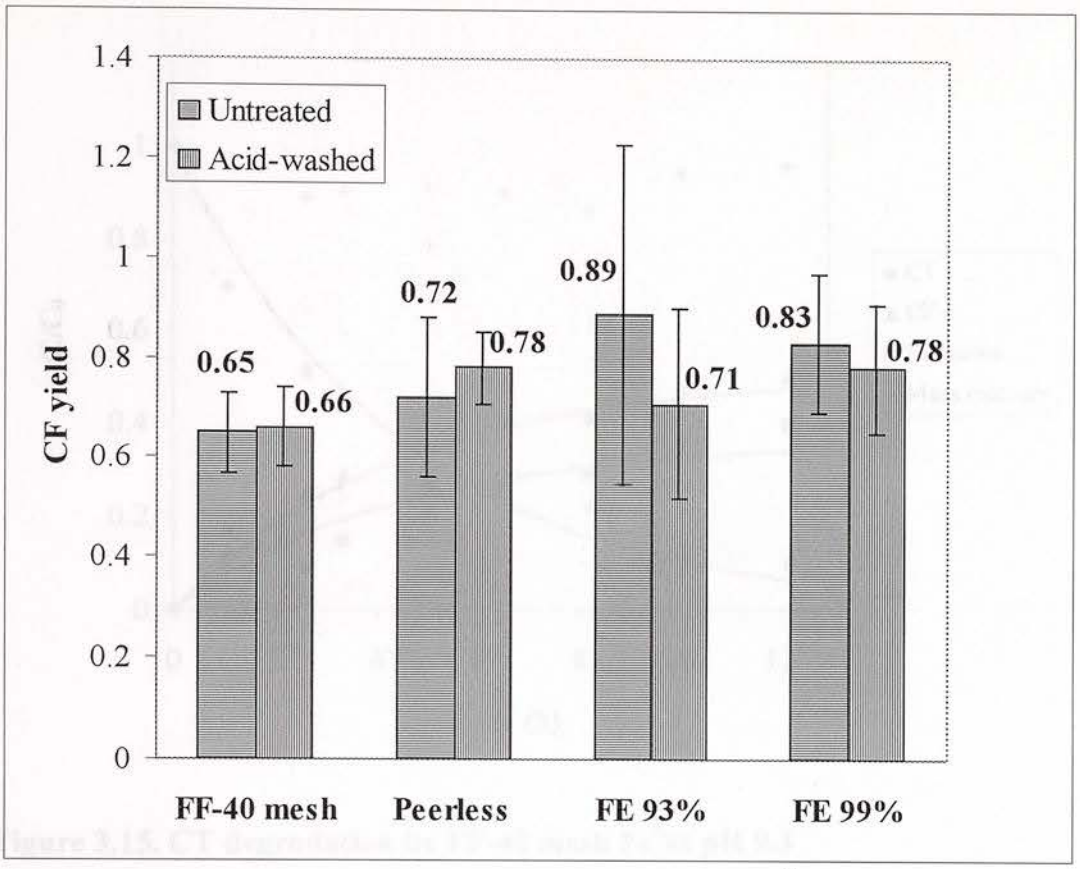

Figure 3.14. CF yields for untreated and acid-washed Fe^0 systems

3.4 Effect of Groundwater Characteristics on Rates and Products

3.4.1. Effect of pH on Rates. As expected k_{obs} values for CT degradation by different types of untreated Fe^0 at pH 9.3 were lower than the values at pH 7 (See column 6, rows 1-4 vs rows 7-10 in Table 3.3). Figures 3.15-3.17 display the kinetics of CT reduction by FF-40 mesh, Peerless, and FE 99% Fe^0 at pH 9.3. CT was not degraded by FE 93% at pH 9.3 during the monitoring time of 40 h.

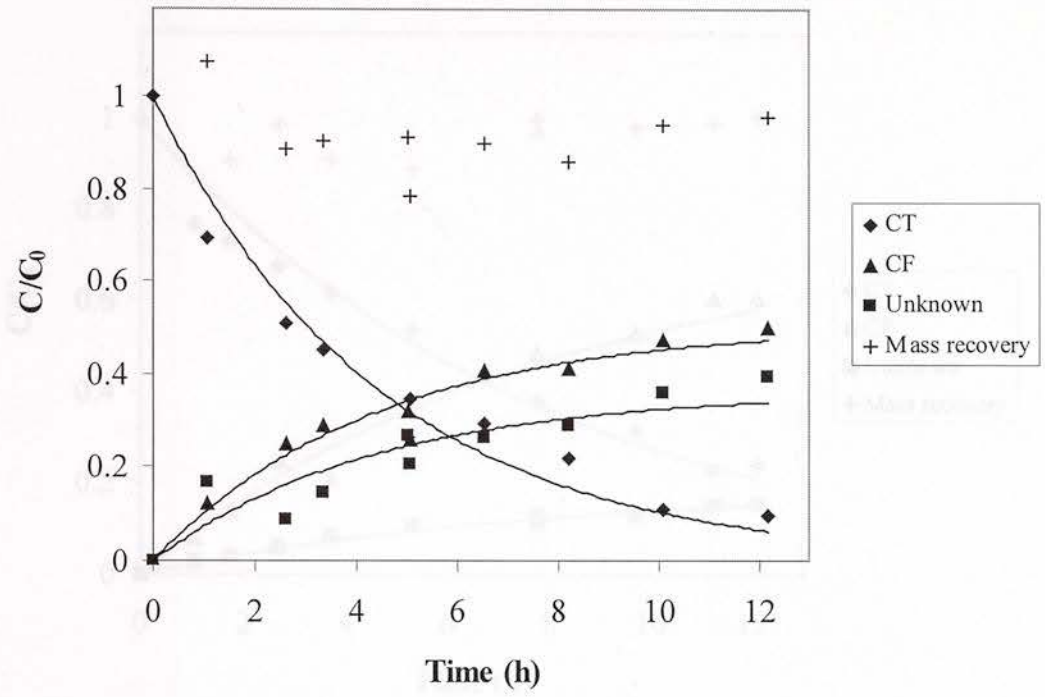

Figure 3.15. CT degradation by FF-40 mesh Fe^0at pH 9.3

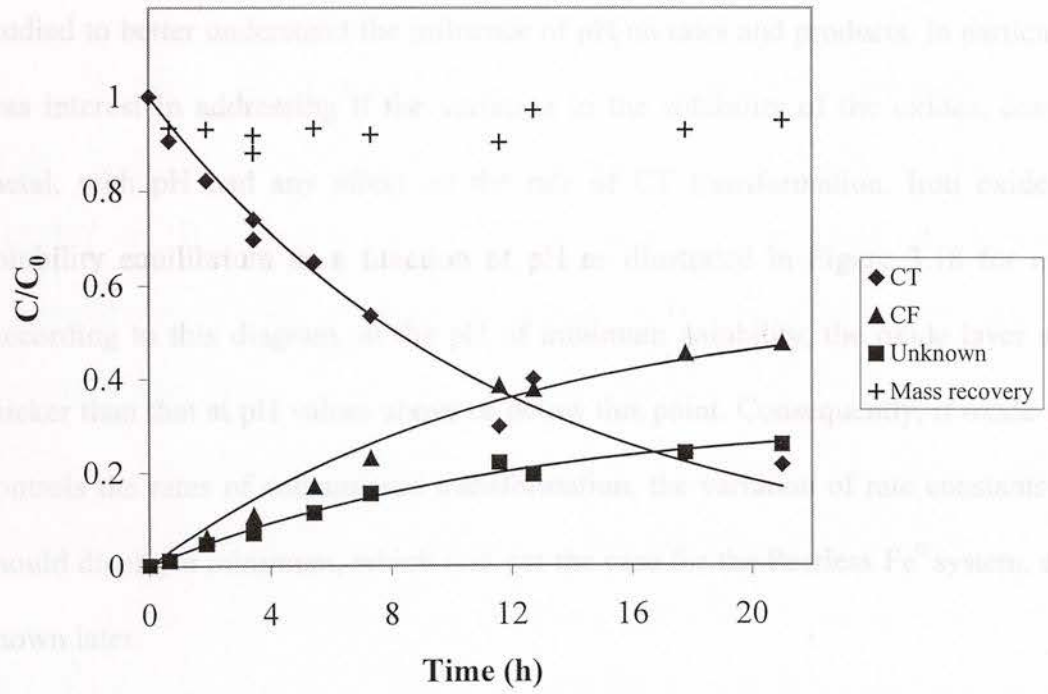

Figure 3.16. CT degradation by Peerless Fe^0at pH 9.3

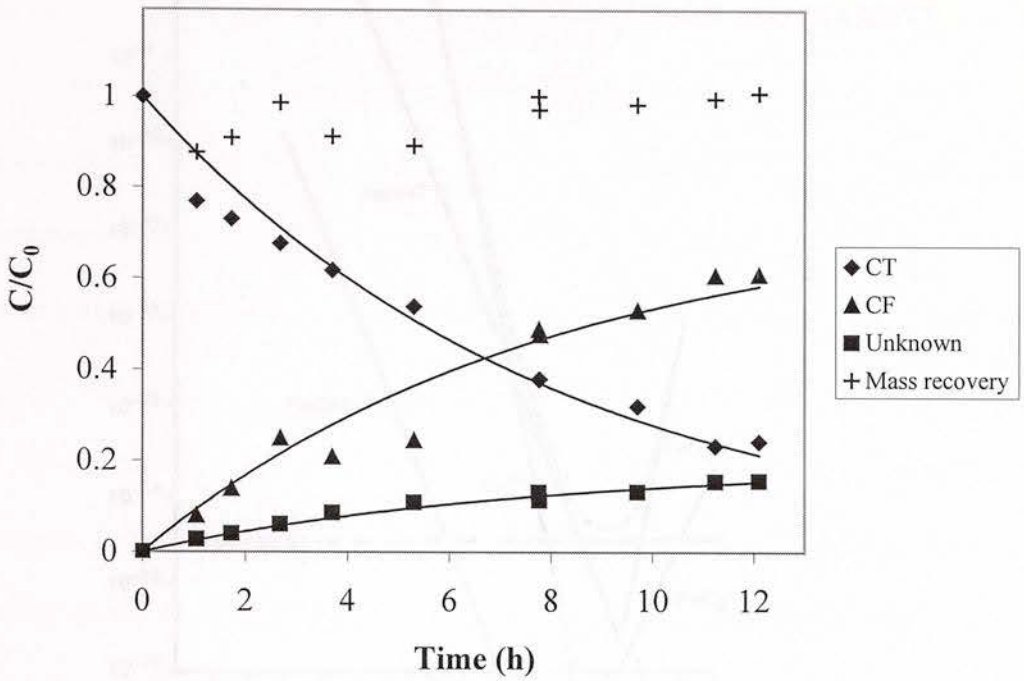

Figure 3.17. CT degradation by FE 99% Fe^0at pH 9.3

The degradation of CT by untreated Peerless Fe^0 at additional pH values was studied to better understand the influence of pH on rates and products. In particular, there was interest in addressing if the variation in the solubility of the oxides, covering the metal, with pH had any affect on the rate of CT transformation. Iron oxides exhibit solubility equilibrium as a function of pH as illustrated in Figure 3.18 for magnetite. According to this diagram, at the pH of minimum solubility, the oxide layer should be thicker than that at pH values above or below this point. Consequently, if oxide solubility controls the rates of contaminant transformation, the variation of rate constants with pH should display a minimum, which was not the case for the Peerless Fe^0 system, as will be shown later.

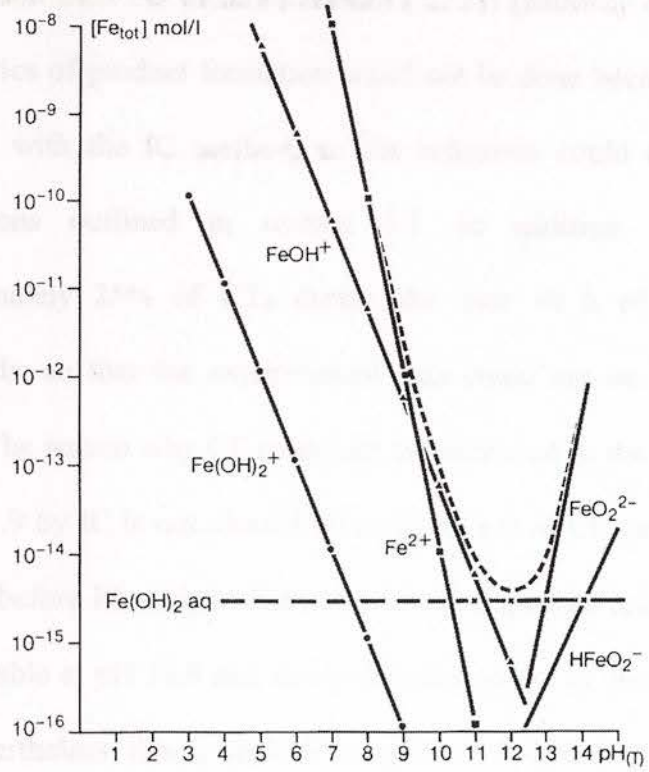

Figure 3.18. Solubility diagram for magnetite at 25° C. Solid lines show the contributions of individual ion species to the solubility of magnetite, represented by the dotted line. Source: Bohnsack (*80*)

Figures 3.19-3.22 show the kinetics of CT reduction by Peerless Fe^0 at pH values of 8.4, 10.2, 12, and 12.9. Figure 3.19 illustrates that regardless of the type of buffer (HEPES vs CHES) used to control pH, the rate of CT degradation was the same in the two systems at pH 8.4 even though the ionic strength of the HEPES aqueous solution was six times that of the CHES solution. Thus, the variation in rates is due the pH itself rather than to the type of buffer. The degradation of CT by Peerless Fe^0 proceeded increasingly slower at pH values of 10.2, 12, and 12.9 as observed in Figures 3.17-3.19.

Although CT degradation by Peerless Fe^0 at pH 12.9 was slow with a half-life = 30 h, the production of CF was minimal most likely due to its alkaline hydrolysis, which proceeds via the reverse of pathway b in Figure 1.1 to form the trichloromethyl carbanion

($^-$:CCl_3) and then the dichlorocarbene (:CCl_2) (pathway d in Figure 1.1) (*81*). Modeling the kinetics of product formation could not be done because neither Cl^- nor $HCOO^-$ was resolved with the IC method, so the unknown could not be estimated based on the calculations outlined in section 3.1. In addition, CF production increased to approximately 25% of CT_0 during the first 10 h of reaction, but stayed constant afterwards, so that the experimental data could not be fitted to the pseudo-first order model. The reason why Cl^- could not be measured in the standards and reaction samples at pH 12.9 by IC is not clear. Lowering the pH of Cl^- standards prepared in the pH 12.9 solution before IC analysis did not result in improved resolution, suggesting that Cl^- may not be stable at pH 12.9 and that it decomposes to an unidentified compound at this high pH. Nevertheless, this is unlikely because Cl^- is stable over a wide range of pH at low to high concentrations unless it is subjected to electrolysis.

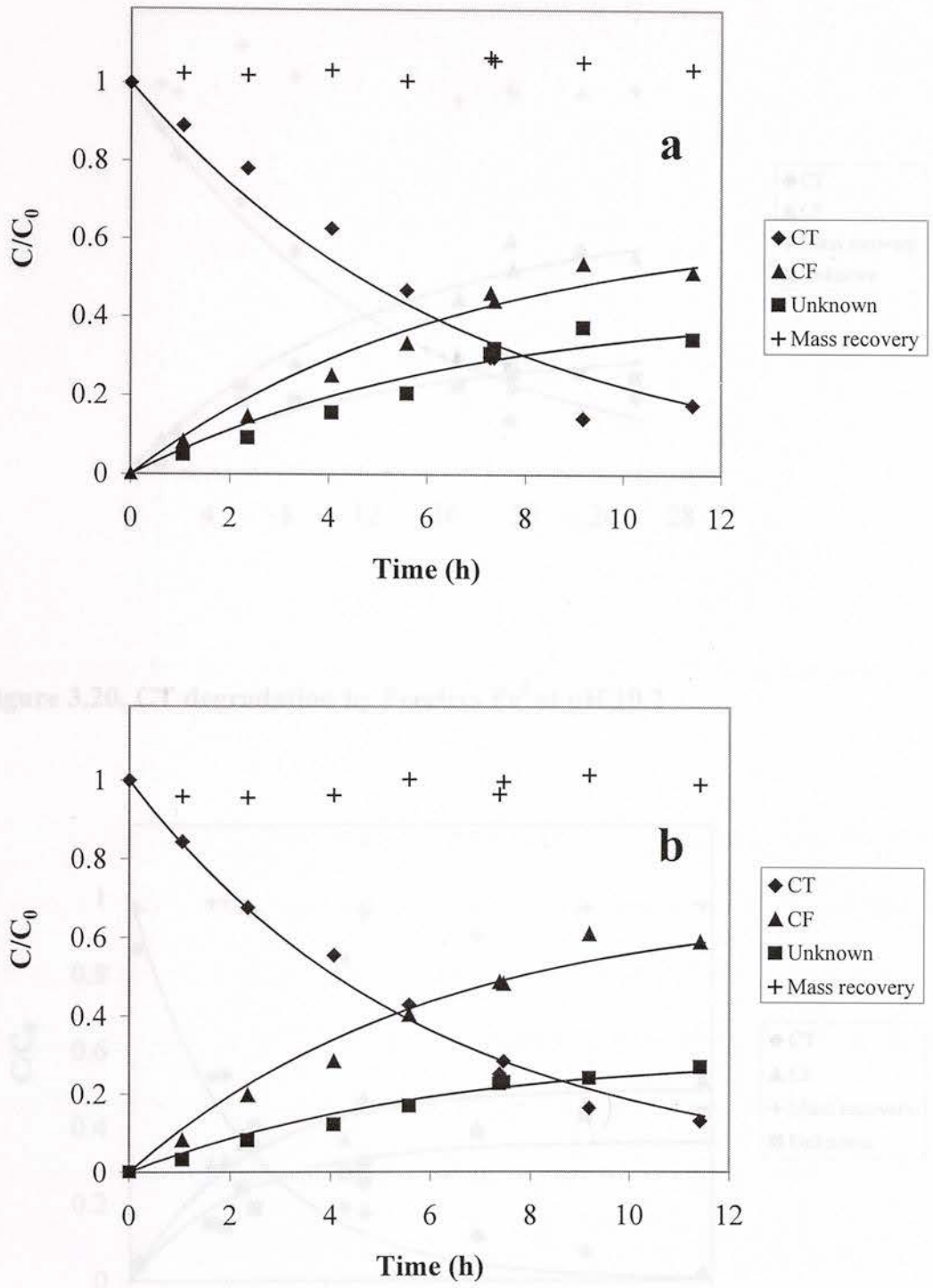

Figure 3.19. CT degradation by Peerless Fe^0 at pH 8.4 with (a) HEPES, and (b) CHES buffers

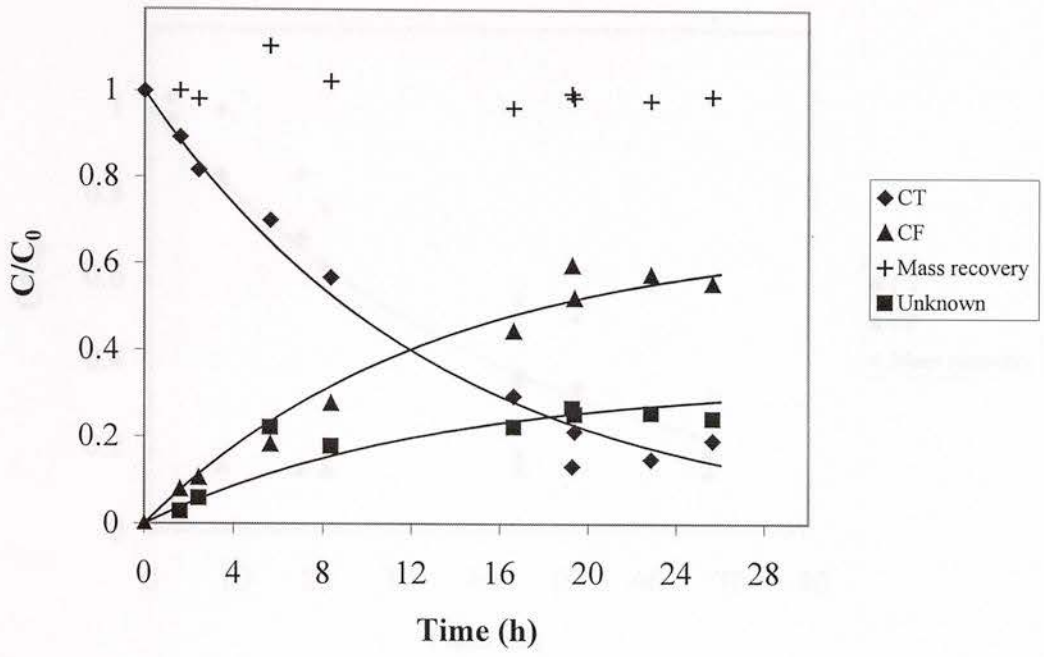

Figure 3.20. CT degradation by Peerless Fe^0 at pH 10.2

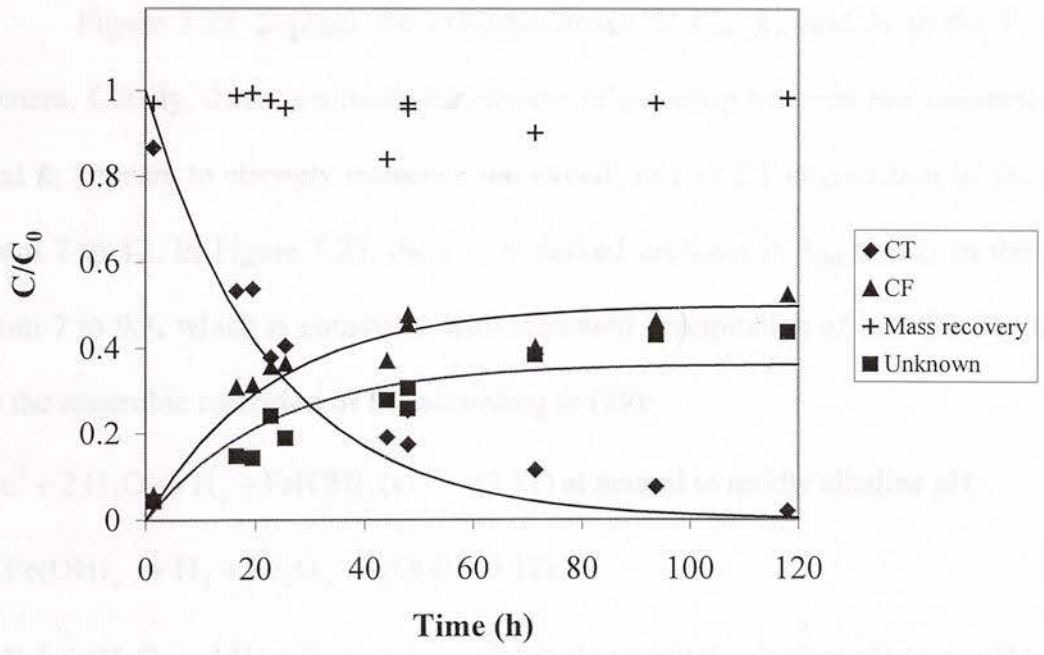

Figure 3.21. CT degradation by Peerless Fe^0 at pH 12

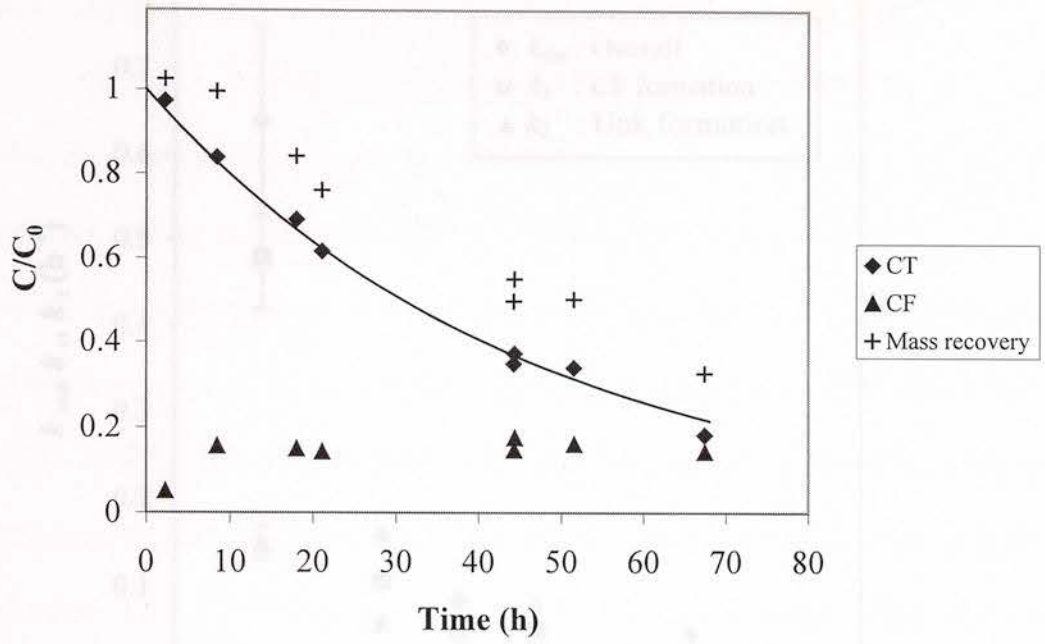

Figure 3.22. CT degradation by Peerless Fe^0 at pH 12.9. Carbon mass recovery is due to CT and CF since the Unk was not estimated.

Figure 3.23 displays the pH-dependence of k_{obs}, k_1, and k_2 in the Peerless Fe^0 system. Clearly, there is a nonlinear inverse relationship between rate constants and pH, and k_1 appears to strongly influence the overall rate of CT degradation in the pH range from 7 to 12. In Figure 3.23, there is a marked decrease in k_{obs} and k_1 in the pH range from 7 to 9.3, which is consistent with increased precipitation of iron (II, III) oxides due to the anaerobic corrosion of Fe^0 according to (*59*):

$$Fe^0 + 2\,H_2O \rightarrow H_2 + Fe(OH)_2(s) \quad (3.11)$$ at neutral to mildly alkaline pH

$$2\,Fe(OH)_2 \rightarrow H_2 + Fe_2O_3 \cdot H_2O(s) \quad (3.12)$$

$$3\,Fe^0 + 4H_2O \rightarrow 4\,H_2 + Fe_3O_4(s) \quad (3.13)$$ above mildly alkaline pH (e.g., pH > 9)

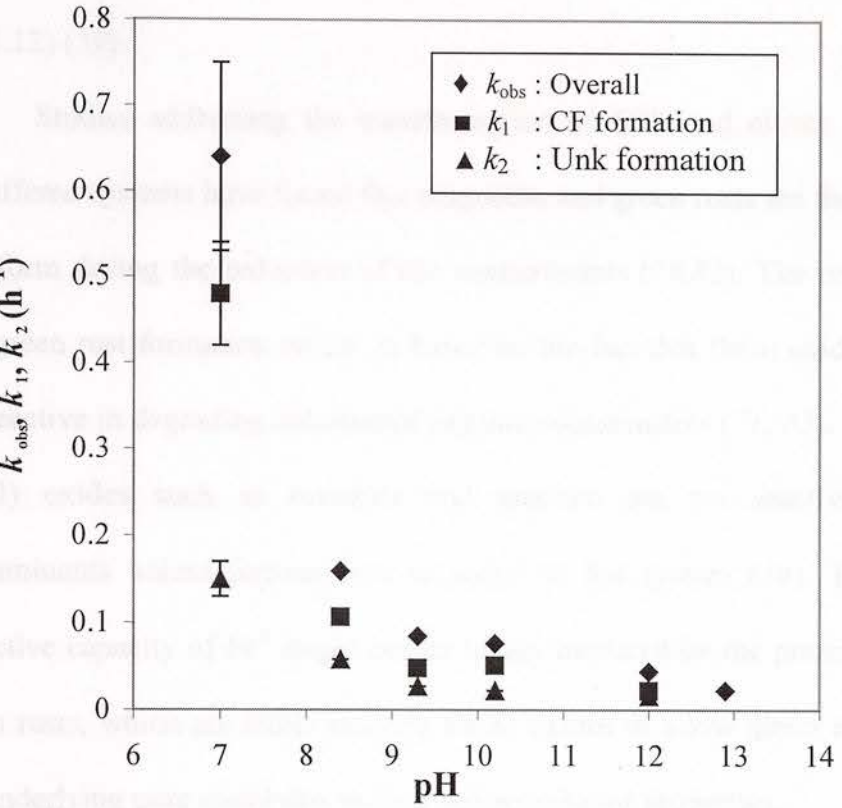

Figure 3.23. Rate constants vs pH for CT degradation by Peerless Fe^0. Error bars display 95% confidence intervals. Data points at pH 8.4 are the average of two values obtained in separate experiments with HEPES and CHES buffer, respectively (see rows 5 and 6 in Table 3.3).

Equations 3.11-3.13 show that ferrous hydroxide ($Fe(OH)_2$), hydrated ferric oxide ($Fe_2O_3 \cdot H_2O$) and magnetite (Fe_3O_4) are solid phases likely to form on iron metal as a result of its corrosion in aqueous solution. Magnetite, though, is expected to form a dense protective layer that inhibits diffusion of potential Fe^0 oxidizing species such as protons and CT to the bare metal, decreasing corrosion and contaminant reduction rates, but it still would allow direct electron transfer from the metal to the contaminant via tunneling (*38*, *79*). $Fe(OH)_2$, however, is not as dense and ordered as Fe_3O_4, which allows corrosion

to occur, and it is eventually transformed to a more stable compound such as $Fe_2O_3 \cdot H_2O$ (eq 3.12) (*59*).

Studies addressing the transformation of TCE and nitrate by Fe^0 in anaerobic, unbuffered systems have found that magnetite and green rusts are the predominant oxides that form during the reduction of the contaminants (*79,82*). The relevance of magnetite and green rust formation on Fe^0 is based on the fact that these oxides in their pure form are reactive in degrading chlorinated organic contaminants (*71, 83*). On the contrary, pure Fe(III) oxides such as hematite and goethite are not reactive in degrading the contaminants unless ferrous iron is added to the system (*14*). This implies that the reductive capacity of Fe^0 might not be totally hindered by the presence of magnetite and green rusts, which are either reactive Fe(II) oxides or allow direct electron transfer from the underlying pure metal due to their semiconductor properties.

Thus, it is possible that more than one mechanism (i.e., localized corrosion, direct electron transfer through the oxide layer, Fe(II) oxide reactive species) could explain the variation in rates of CT transformation as a function pH in our systems as suggested by others (*38*, *52*). Eventually, direct electron transfer through a semiconductor oxide layer or via electron tunneling and mediated reduction by Fe(II) reactive oxides could be the dominant mechanisms at high pH values in our systems. Mediated reduction by Fe(II) oxides, however, would require Fe(II) oxides as the predominant surface species in our systems at high pH. Localized corrosion may not be an important mechanism for CT reduction at high pH values in the absence of aggressive anions and in the presence of a protective oxide layer like Fe_3O_4 since fewer crevices would be present.

Surface characterization of Peerless Fe^0 samples equilibrated in anoxic buffer solutions of pH 7 and 9.3 was conducted to get information about the composition of the surface oxides as well as their thickness. Specifically, these analyses were aimed at identifying potential causes for the observed trend of decreasing rate constants with increasing pH.

The spectra of the iron and oxygen regions for the Peerless surfaces equilibrated in pH 7 and pH 9.3 buffer solutions are presented in Figures 3.24-3.26. These analyses were done in duplicate, so spectra for a first and second set of analyses are displayed in Figures 3.24-3.26. In addition, at least two different locations of the same sample preparation were analyzed and are designated as spots 1 and 2 in Figures 3.24-3.26.

No differences were observed in the binding energies of the Fe $2p_{3/2}$ peak for the two pH-equilibrated Peerless samples in the first set of analyses (see Figure 3.24a). The binding energies for the Fe $2p_{3/2}$ peak of the pH 7-equilibrated surfaces were 711 and 710.7 eV for spots 1 and 2 respectively, and for the pH 9.3-equilibrated surfaces binding energies were 711.2 and 710.7 eV for spots 1 and 2, respectively. This indicates that Fe(III) oxides made up the oxide layer of the two different pH-equilibrated irons. In contrast, the oxygen regions of the pH 7 and pH 9.3-equilibrated samples differed, as illustrated in Figures 3.25a and 3.25b. Two peaks at about 530 and 531.6 eV are seen in the oxygen region of the pH-7.0 equilibrated sample, but for the pH 9.3-equilibrated sample the peak at 531.6 eV either disappeared or was just a shoulder. The peak at 531.7 eV is characteristic of a Fe–OH bond whereas the peak at 530 eV is characteristic of a Fe–O–Fe bond and both of these peaks are present in iron oxyhydroxides like

lepidocrocite (γ-FeOOH) (*84*). Thus, it is likely that the surface of the Peerless samples exposed to pH 7 was made up of iron oxyhydroxides.

On the other hand, marked differences were not seen on the oxygen regions of the second set of samples (See Figure 3.26), but the iron regions were dissimilar (See Figure 3.24b). The binding energies for the Fe $2p_{3/2}$ peak of the pH 7-equilibrated surfaces were were 709.4 eV for both spots. For the pH 9.3-equilibrated surfaces, binding energies were 711.2 eV for both spots. Thus, samples exposed to pH 9.3 appeared to be more oxidized than the ones exposed to pH 7 as inferred from the higher values of their binding energies. Samples for the duplicate analyses were prepared exactly the same way, so it is unclear why the two sets of analyses gave different results regarding the types of oxides present on the pH-equilibrated irons. Recent research, however, has shown that handling and preparation of Fe^0 samples taken from operating PRBs impacts the types of oxides found on the Fe^0 surface (*85*). For this reason, several studies have used in situ techniques (e.g., in situ Raman spectroscopy) to characterize the types of oxides that form during the reduction of contaminants by Fe^0 (*79*).

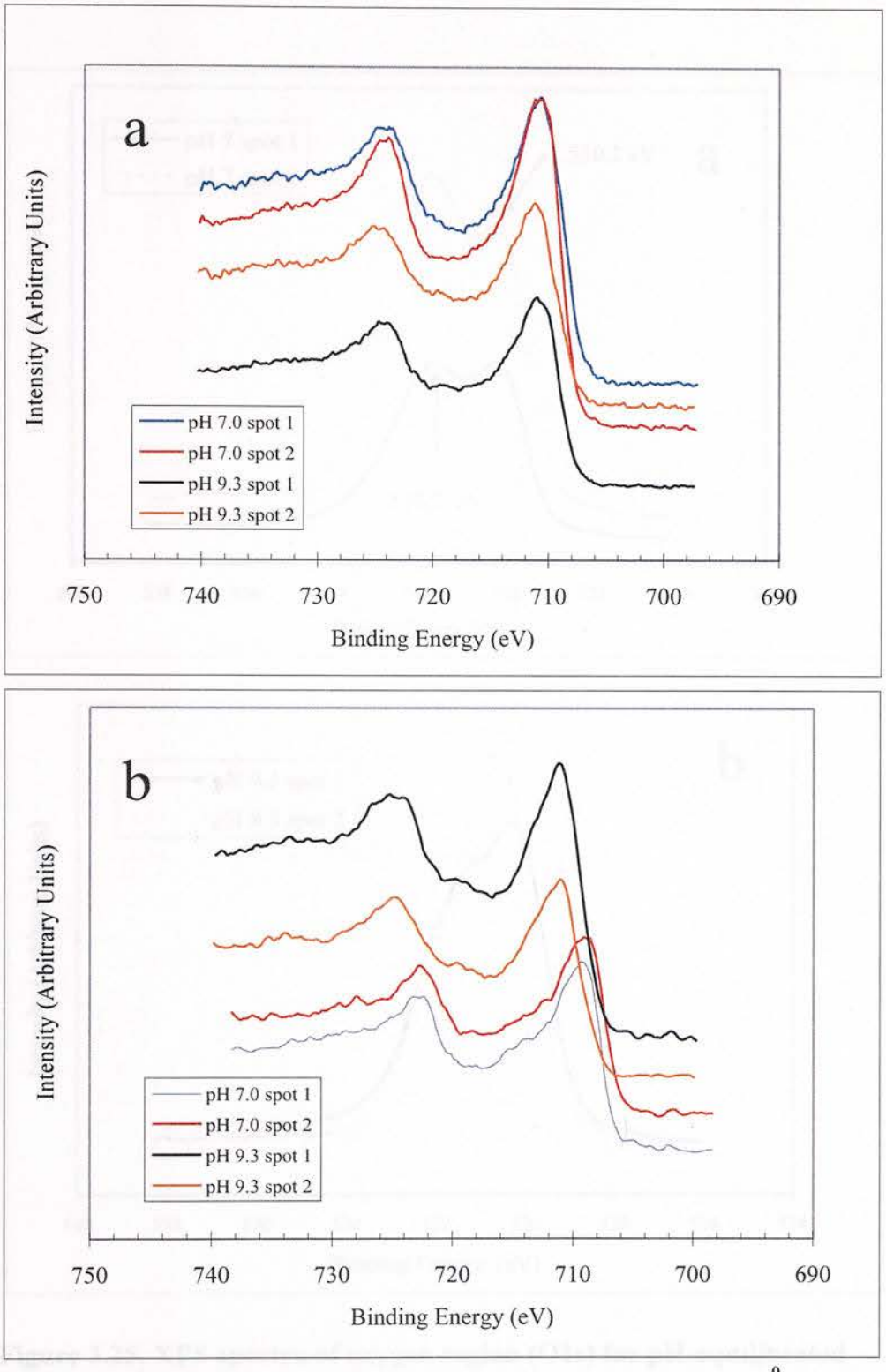

Figure 3.24. XPS spectra of iron region for pH-equilibrated Fe^0 samples. (a) Spectra from first set of analysis; (b) spectra from second set of analysis.

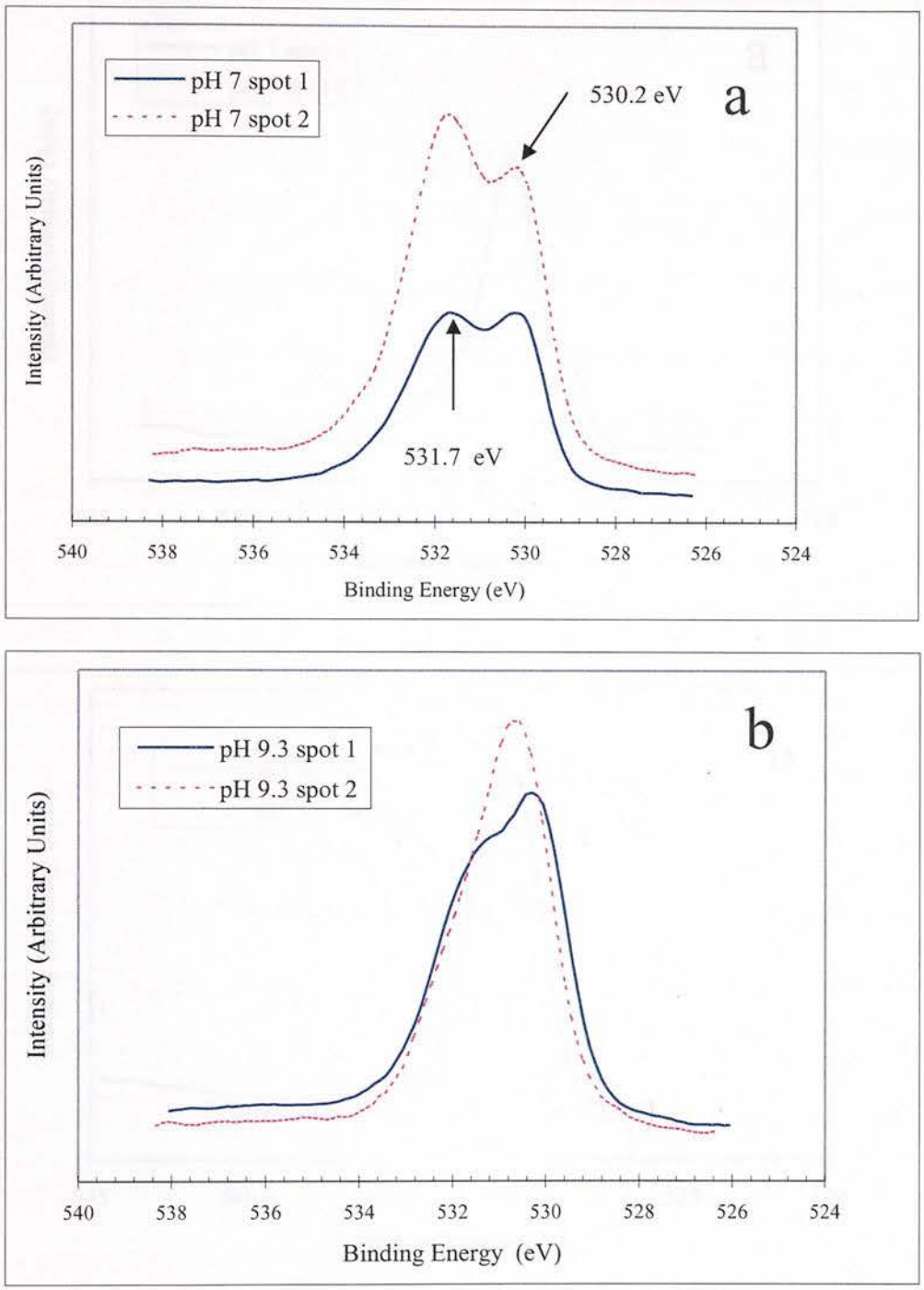

Figure 3.25. XPS spectra of oxygen region (O1s) for pH-equilibrated Peerless Fe^0 samples. (a) pH 7; (b) pH 9.3. First set of analysis. Binding energies for the peaks' maximum were: 531.7 and 530.2 eV for both spots of the pH-7 equilibrated samples; 531.2 and and 530.3 eV for spot 1 of the the pH 9.3-equilibrated sample, and 530.7 for spot 2 of the pH 9.3-equilibrated sample.

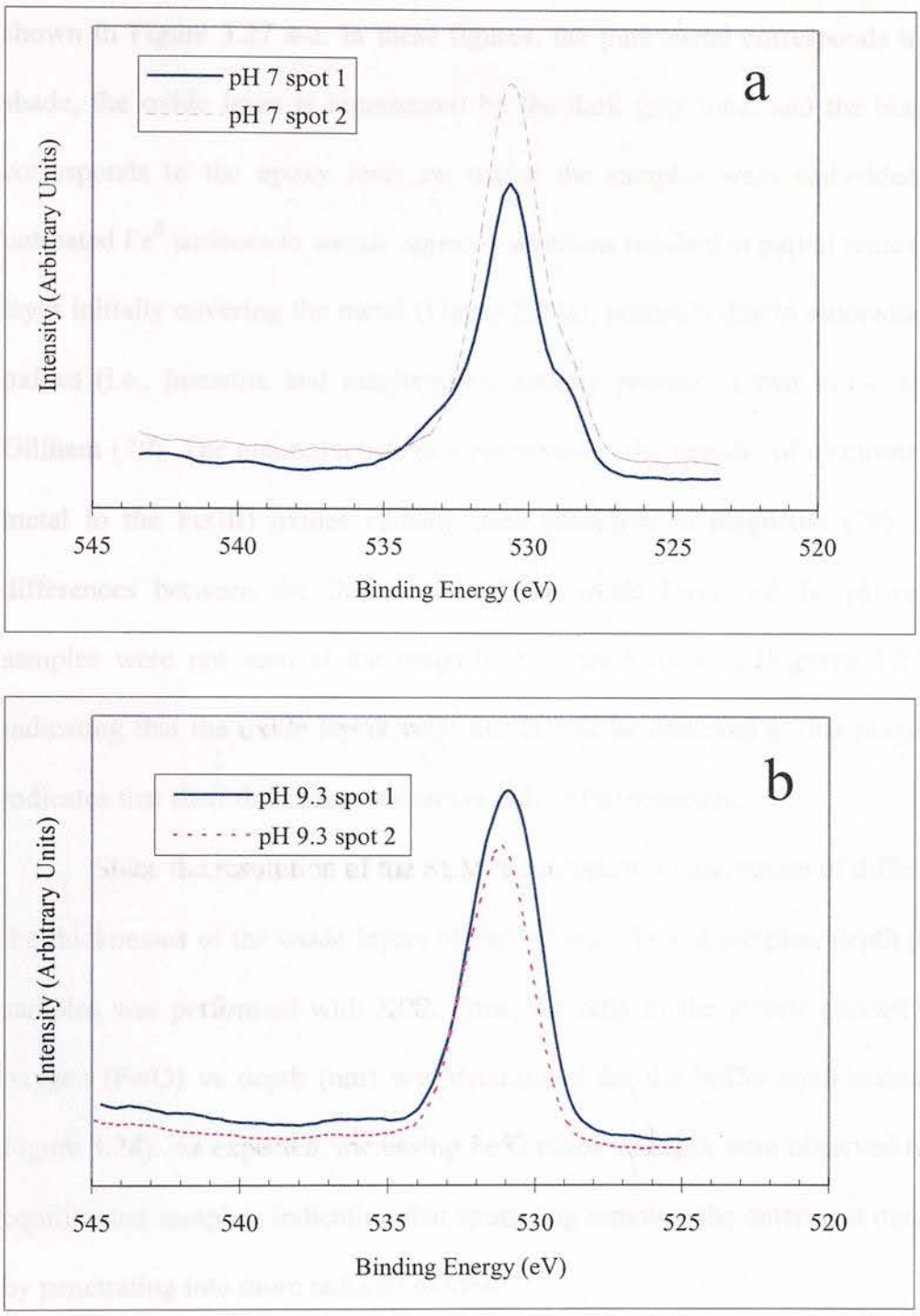

Figure 3.26. XPS spectra of oxygen region (O1s) for pH-equilibrated Peerless Fe^0 samples. (a) pH 7; (b) pH 9.3. Second set of analysis. Binding energies for the peak maximum were: 530.7 eV for both spots of the pH-7 equilibrated samples; 531 and 531.2 eV for spots 1 and 2, respectively, of the pH 9.3-equilibrated sample.

SEM micrographs of untreated and pH-equilibrated Peerless Fe^0 samples are shown in Figure 3.27 a-c. In these figures, the pure metal corresponds to a bright gray shade, the oxide layer is represented by the dark gray tone, and the black background corresponds to the epoxy resin on which the samples were embedded. Exposure of untreated Fe^0 surfaces to anoxic aqueous solutions resulted in partial removal of the oxide layer initially covering the metal (Figure 3.24a), probably due to autoreduction of Fe(III) oxides (i.e., hematite and maghemite), initially present in cast irons, as discussed by Gillham (*79*). The autoreduction process involves the transfer of electrons from the pure metal to the Fe(III) oxides causing their reduction to magnetite (*79*). Nevertheless, differences between the thicknesses of the oxide layers of the pH-equilibrated Fe^0 samples were not seen at the magnification used (6000x) (Figures 3.27b and 3.27c), indicating that the oxide layers were too thin to be observed at that magnification. This indicates that their thickness was on the order of nanometers.

Since the resolution of the SEM did not permit observation of differences between the thicknesses of the oxide layers of the pH-equilibrated samples, depth profiling of the samples was performed with XPS. Thus, the ratio of the atomic percentages of iron to oxygen (Fe/O) vs depth (nm) was determined for the buffer-equilibrated samples (see Figure 3.28). As expected, increasing Fe/O ratios vs depth were observed for the two pH-equilibrated samples, indicating that sputtering removes the outermost oxidized layer (s), by penetrating into more reduced oxides.

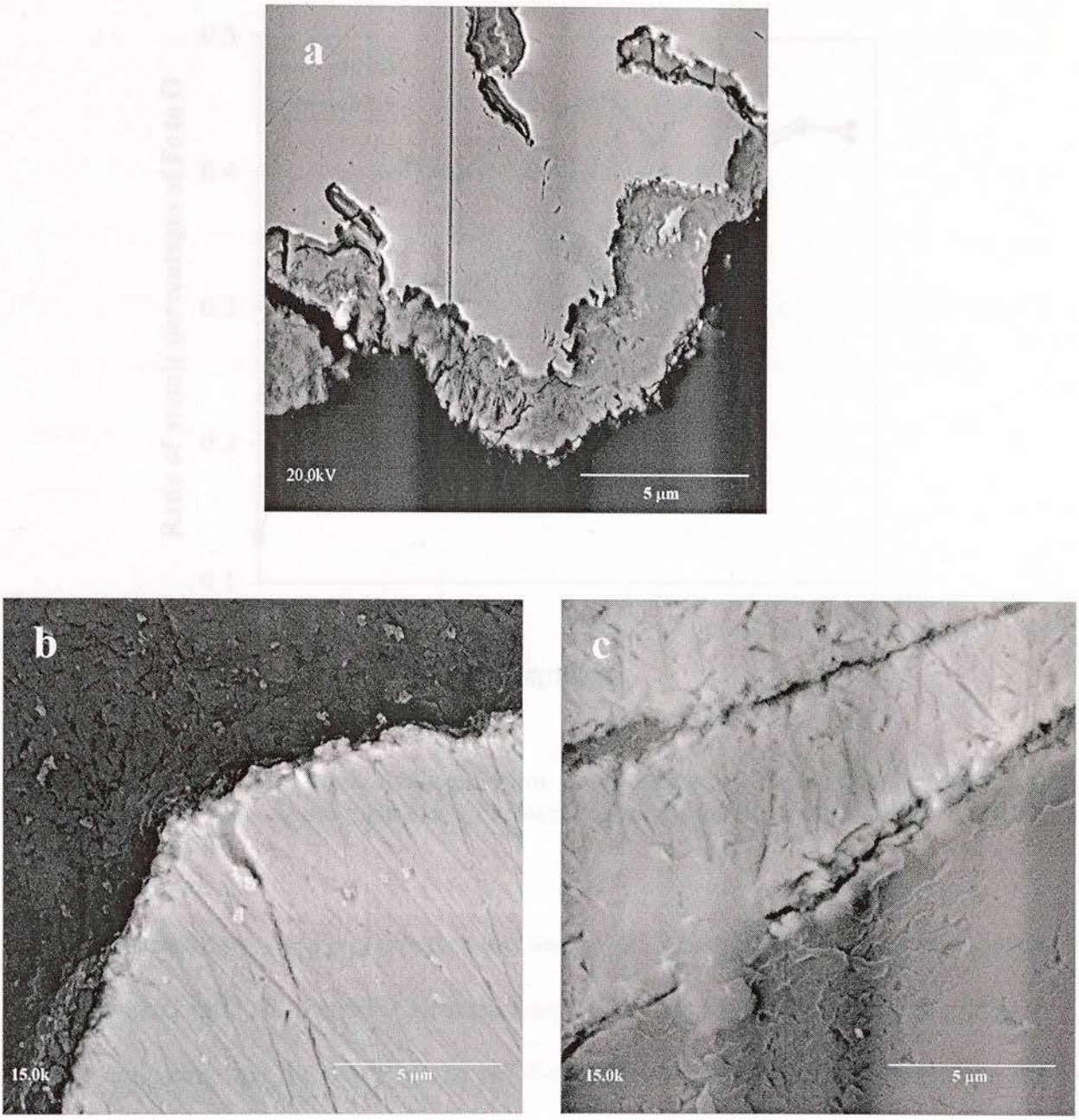

Figure 3.27. SEM backscattered electron images of Peerless Fe^0 samples (a) untreated; (b) pH 7-equilibrated;(c) pH 9.3-equilibrated. Equilibration time = 24 h under anoxic conditions. Pictures taken with ETEC Autoscan.

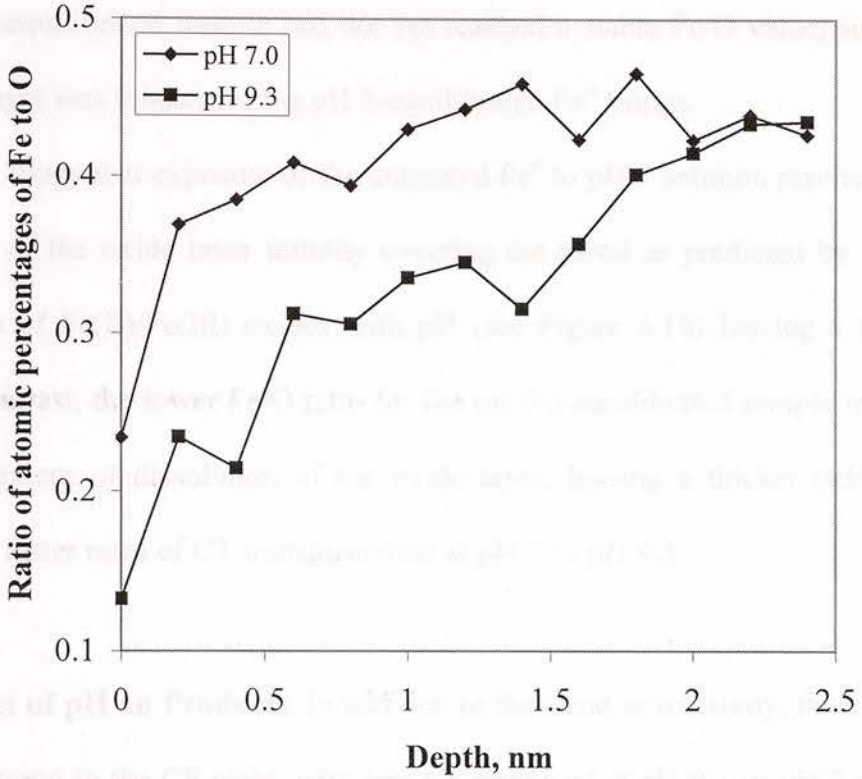

Figure 3.28. Ratio of atomic composition percentages of Fe to O vs depth (nm) obtained from XPS depth profiling. Elements considered in the scan were C, N, O, Si, S, Mn, and Fe.

Interestingly, the Fe/O atomic ratio for the pH 7-equilibrated sample was greater than the Fe/O ratio for the pH 9.3-equilibrated Fe^0 filings for the first 2 nm of sputtered oxide, indicating that the oxide on the pH 7-equilibrated Fe^0 was less oxidized than the oxide on the pH 9.3-equilibrated Fe^0. For example, the Fe/O ratios for wüstite (FeO), an Fe(II) oxide, magnetite (Fe_3O_4), an Fe(II)/Fe(III) oxide, maghemite (γ-Fe_2O_3) and goethite(α-FeOOH), both of which are Fe(III) oxides, are 1.0, 0.75, 0.67, and 0.5, respectively, illustrating that the Fe/O ratio for Fe(II) oxides are higher than the ones for

Fe(III) oxides. Furthermore, the Fe/O atomic ratio for the pH 7-equilibrated sample appeared to plateau to a constant value of 0.4 at about 2 nm of sputtered oxide whereas the pH 9.3-equilibrated sample had not yet reached a stable Fe/O value, suggesting that the oxide layer was thinner for the pH 7-equilibrated Fe^0 filings.

It is likely that exposure of the untreated Fe^0 to pH 7 solution resulted in far more dissolution of the oxide layer initially covering the metal as predicted by the solubility equilibrium of Fe(II)/Fe(III) oxides with pH (see Figure 3.18) leaving a thinner oxide layer. In contrast, the lower Fe/O ratio for the pH 9.3-equilibrated sample may indicate a decreased extent of dissolution of the oxide layer, leaving a thicker oxide. This may explain the faster rates of CT transformation at pH 7 vs pH 9.3.

3.4.2. Effect of pH on Products. In addition to the trend in reactivity, there is also a pH-dependent trend in the CF yield, with less CF produced at pH 9.3 vs pH 7 in all systems (See column 9, rows 1-4 vs rows 7-10 in Table 3.3). Figure 3.29 shows a pattern of generally lower CF yields as the pH increases in the Peerless system.

Since different buffers were used to control the pH in this set of experiments, two independent CT degradation experiments were conducted at pH 8.4 in the presence of 50 mM buffer solutions of HEPES and CHES, respectively, to check whether the buffers' structures were influencing product distribution. Kinetic parameters as well as the yields of products obtained from these two experiments did not differ to a great extent, suggesting that the buffers did not affect product distribution (see columns 9 and 10, rows 5 and 6 in Table 3.3). Moreover, the content of methanol of the aqueous solution (1% v/v) did not influence product distribution as supported by the experiments conducted in

unbuffered systems in the absence of methanol (see Table 3.1, rows 4 and 5) with CF being the major product.

One possible explanation for the observed trend in CF yields as a function of pH is a decrease in the favorability of hydrogenolysis as nascent hydrogen (H·) from the reduction of protons (H^+) and hydrogen atom donors decrease in activity as pH increases (*4*, *20*). Protonated iron oxide hydroxyl species (≡ FeOH) at near neutral pH values could be good hydrogen atom donors given that oxide hydroxyl species exhibit an acid-base equilibrium as a function of pH (*86*):

$$\equiv FeOH_2^+ \xleftarrow{H^+} \equiv FeOH \xrightarrow{OH^-} \equiv FeO^- + H_2O \qquad (3.14)$$

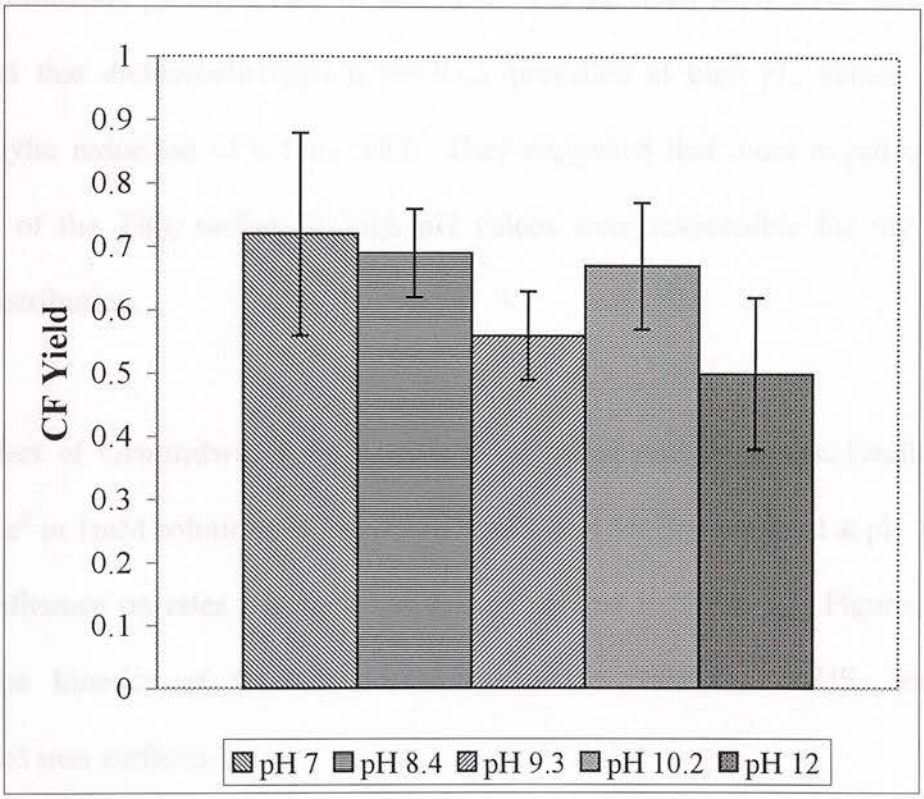

Figure 3.29. Yields of CF vs pH in CT-Peerless Fe^0 systems. Error bars represent 95% confidence intervals.

The electron donating capacity and reduction potential of the iron oxides covering the metal varies with pH (*20*, *86*, *87*), which could also explain the trend in product distribution. For example, electron-rich deprotonated oxide surface hydroxyl groups (≡ FeO^-) and more negative reduction potentials at the iron oxide-water interface at high pH (*38*, *86*, *87*) may increase the favorability of the dichloroelimination pathway followed by hydrolysis (pathways e and f in Figure 1.1) under alkaline conditions. Two previous investigations lend support to this hypothesis. For one thing, Butler and Hayes (20) proposed that deprotonated surface functional groups present on minerals could be nucleophiles mediating the reduction of TCE, leading to the preferential production of dichloroelimination products such as acetylene. On the other hand, Choi and Hoffmann (*87*) found that dichloroelimination products prevailed at high pH values during the photocatalytic reduction of CT by TiO_2. They suggested that more negative reduction potentials of the TiO_2 surface at high pH values were responsible for the change in product distribution.

3.4.3. Effect of Groundwater Constituents on Rates and Products. Equilibration of FE 99% Fe^0 in 1mM solutions of $NaHCO_3$, NaHS, and $MnBr_2$, buffered at pH 7, did have a slight influence on rates and products as summarized in Table 3.3. Figures 3.30-3.32 display the kinetics of CT transformation in the $NaHCO_3$, NaHS, and $MnBr_2$-equilibrated iron surfaces.

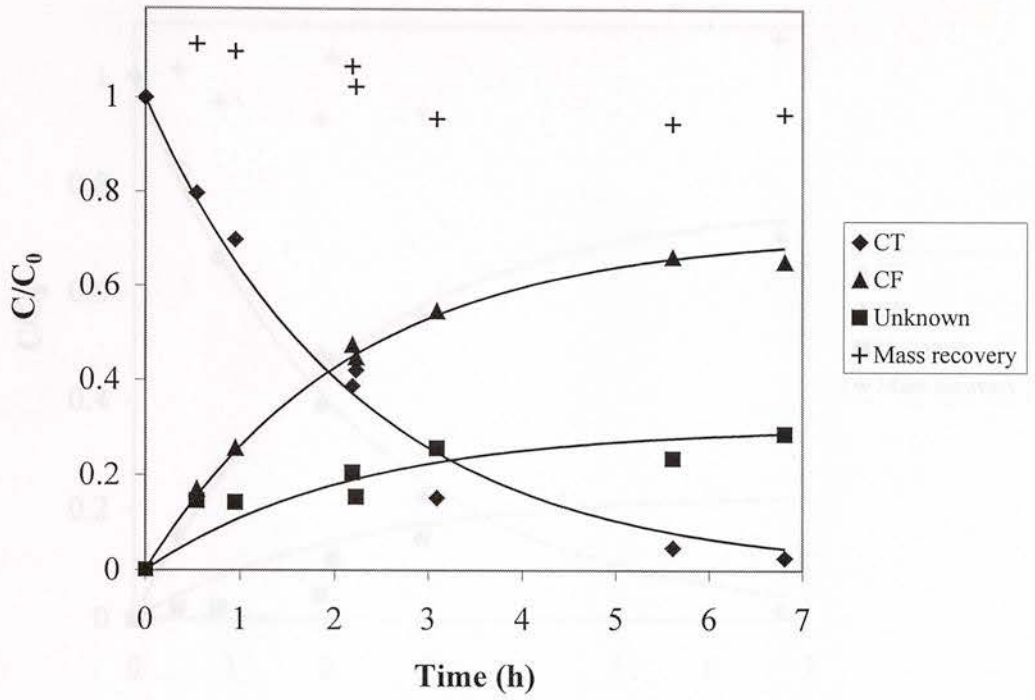

Figure 3.30. CT degradation by FE 99% equilibrated in 1 mM $NaHCO_3$ at pH 7

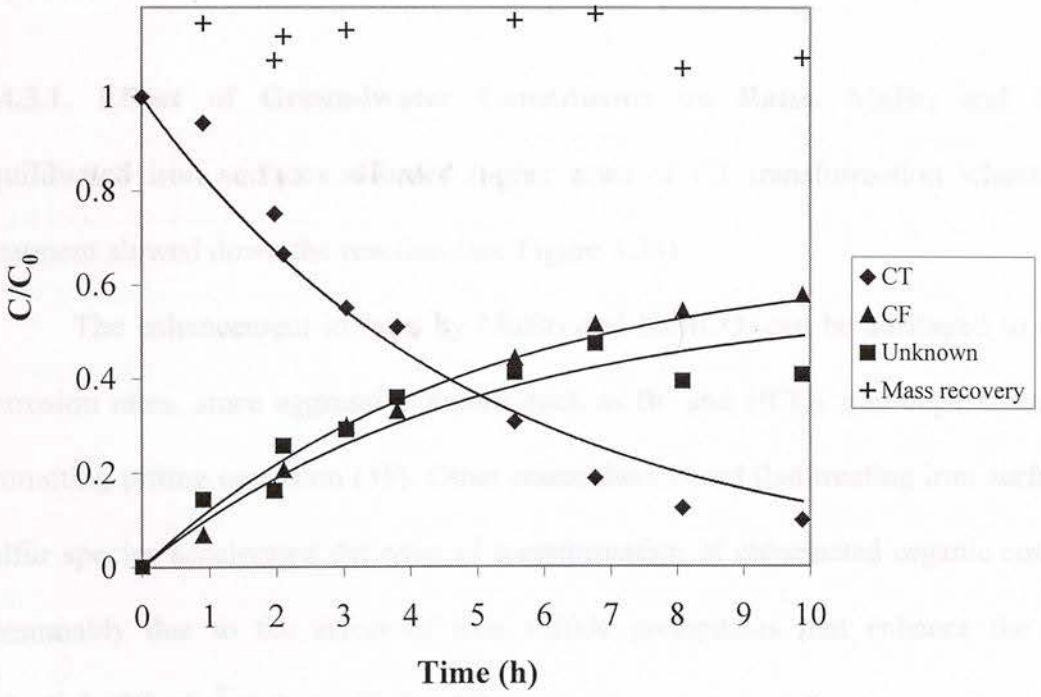

Figure 3.31. CT degradation by FE 99% equilibrated in 1 mM NaHS at pH 7

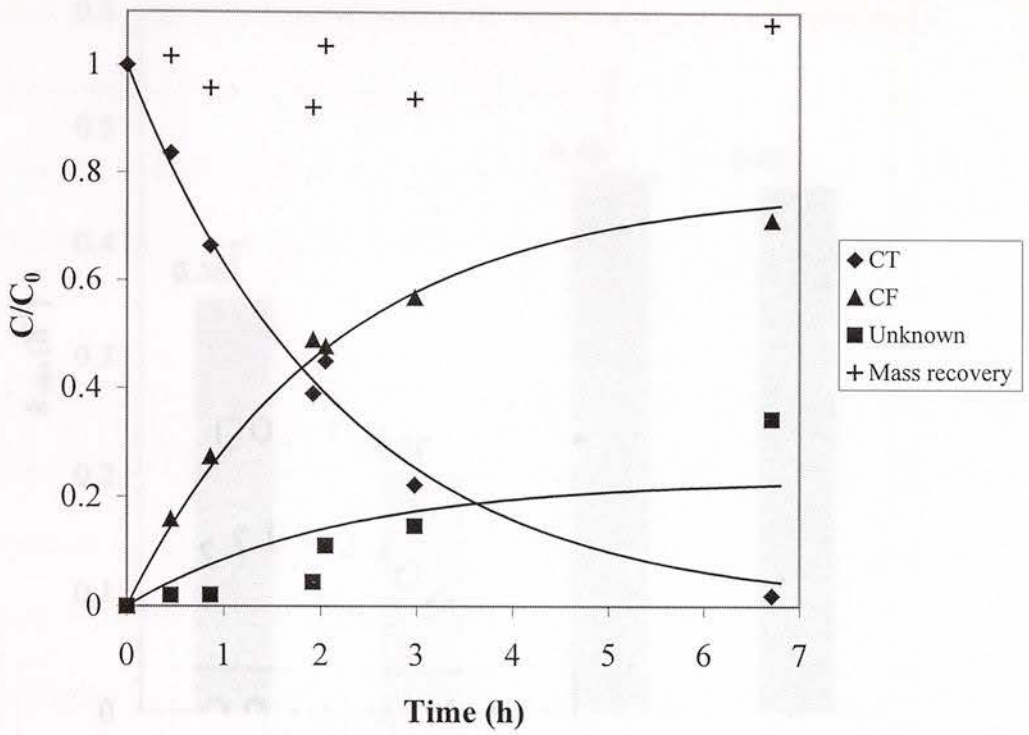

Figure 3.32. CT degradation by FE 99% equilibrated in 1 mM $MnBr_2$ at pH 7

3.4.3.1. Effect of Groundwater Constituents on Rates. $MnBr_2$ and $NaHCO_3$-equilibrated iron surfaces afforded higher rates of CT transformation whereas NaHS treatment slowed down the reaction (see Figure 3.33).

The enhancement in rates by $MnBr_2$ and $NaHCO_3$ can be attributed to increased corrosion rates, since aggressive anions such as Br^- and HCO_3^- can depassivate iron by promoting pitting corrosion (*59*). Other researchers found that treating iron surfaces with sulfur species accelerated the rates of transformation of chlorinated organic compounds, presumably due to the effect of iron sulfide precipitates that enhance the reducing potential of the Fe^0 system (*19*, *20*, *45*).

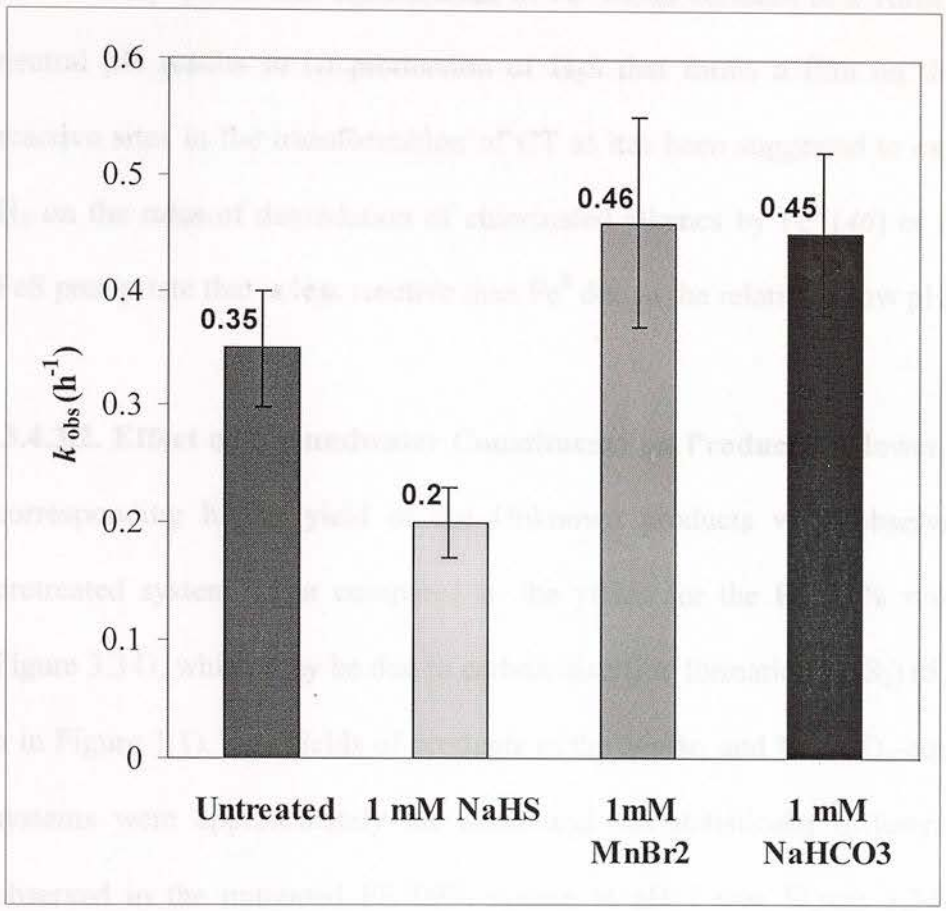

Figure 3.33. Effect of 1 mM NaHS, $MnBr_2$, and $NaHCO_3$ on the overall rate constants

The decrease in the rate of CT degradation in our NaHS-equilibrated system could arise from keeping the pH at 7.0 since higher pH or no pH control was used in some of the previous studies, and the rate of FeS-mediated reductive dechlorination is highly pH-dependent (*20*). Based on the acid-base equilibria of sulfide species ($H_2S \leftrightarrow HS^- + H^+$ (pK_a=7.02); $HS^- \leftrightarrow S^{2-} + H^+$ (pK_a=17) (*88-89*)), bisulfide (HS^-) is quite stable at neutral pH, and expected to be in equimolar proportion with dissolved hydrogen sulfide (H_2S); at high pH values, however, the tendency for precipitation of FeS phases increases as seen from the following equation:

$$Fe^{+2} + HS^- \rightarrow FeS(s) + H^+ \qquad (3.15)$$

Thus, it is possible that equilibration of Fe^0 metal surfaces in a 1mM NaHS solution at neutral pH results in (i) production of H_2S that forms a film on the metal, blocking reactive sites in the transformation of CT as has been suggested to explain the effect of H_2 on the rates of degradation of chlorinated alkenes by Fe^0 (*46*) or (ii) formation of a FeS precipitate that is less reactive than Fe^0 due to the relatively low pH.

3.4.3.2. Effect of Groundwater Constituents on Products. A lower yield of CF and a corresponding higher yield of the Unknown products were observed in the NaHS-pretreated system when compared to the yields for the FE 99% system at pH 7 (see Figure 3.34), which may be due to carbon disulfide formation (CS_2) (5, *10 -11*) (pathway h in Figure 1.1). The yields of products in the $MnBr_2$ and $NaHCO_3$-equilibrated FE 99% systems were approximately the same and not statistically different from the yields observed in the untreated FE 99% system at pH 7 (see Figure 3.34). It is likely that sorption of Mn(II) to iron surfaces was not relevant at neutral pH because sorption of cations increases as pH goes up due to the interaction of deprotonated surface oxide hydroxyl groups with the positively charged cations. Evidence that adsorption of Mn(II) onto the iron oxide of FE 99% was minimal at pH 7 comes from (i) the fact that the pK_a for the hydrolysis of Mn(II) equals 10.2 (*47*), indicating that Mn^{+2} is the predominant species at neutral pH, and (ii) the fact that the pH values corresponding to the points of zero charge (pH_{zpc}) of the possible oxides present on FE 99% vary in the range from 6.4-9.3 (*14*). For example, the pH_{zpc} for goethite, magnetite, hematite, and lepidocrocite are 7.8, 6.4-6.9, 8.3-9.3, and 7.3, respectively (*14*). Adsorption of Mn(II) is anticipated to be significant only at pH values above the pH_{zpc} of the oxides.

It would be interesting to study how products could be affected by the addition of Mn(II) to iron at higher pH values. If ≡ FeO^- groups drive product distribution at high pH values, sorption of Mn(II) to ≡ FeO^- sites is expected to affect the of extent of dichloroelimination.

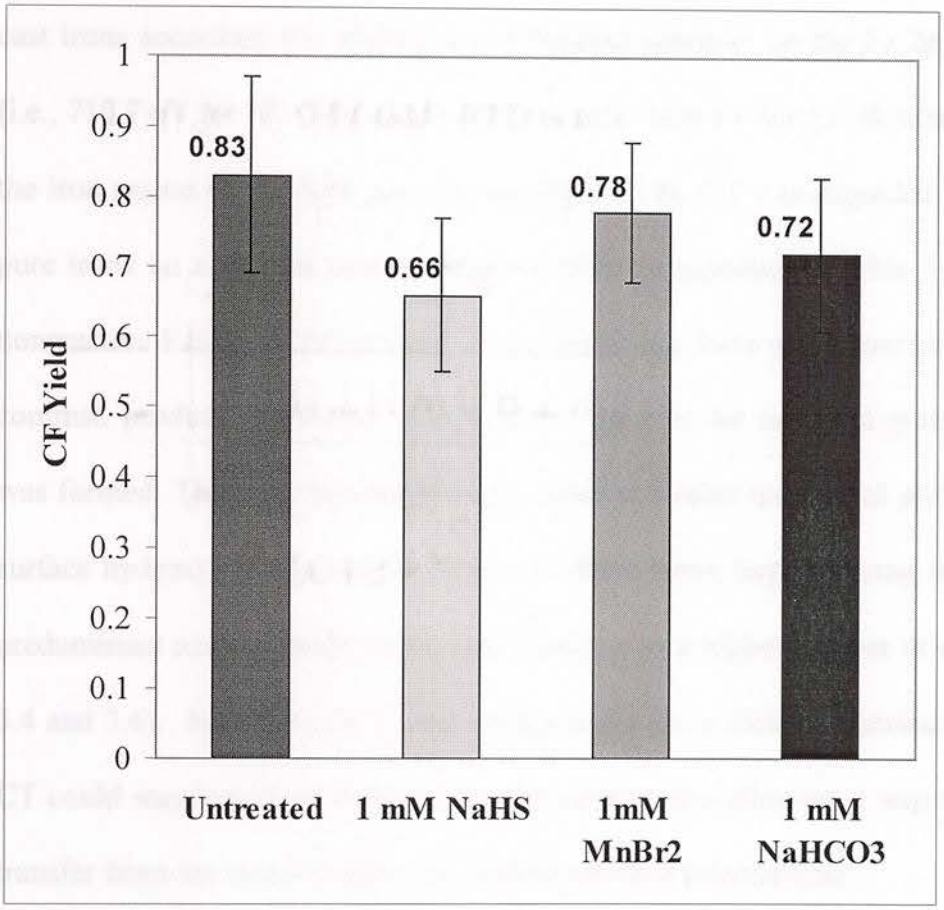

Figure 3.34. Effect of 1 mM NaHS, $MnBr_2$, and $NaHCO_3$ on CF yields

3.5 Summary on the Influence of Fe^0 Surface Properties on Rates and Products

XPS characterization of the untreated Fe^0 metals indicated that their surface was similarly covered by Fe(III) oxides (e.g., hematite, maghemite) or a mix of Fe(II)/Fe(III) oxides (e.g., magnetite). Electrolytic irons, however, appeared to be less oxidized than the cast irons according the slightly lower binding energies for the Fe $2p_{3/2}$ peak maximum (i.e., 710.7 eV for FE 93% and Fe 99% vs and 710.9 eV for FF-40 mesh and Peerless) of the iron region of the XPS spectra (see Figure 3.8). CT was degraded faster by the more pure irons on a surface area normalized basis as reported in Table 3.5, suggesting that nonreactive Fe(III) oxides present in cast irons may have a detrimental effect on rates. In contrast, product distribution was slightly better in the cast iron systems since less CF was formed. This may be explained by either a smaller number of protonated iron oxide surface hydroxyl groups on the surface of these irons, hypothesizing that hematite is the predominant surface oxide on the cast irons, or by a higher content of carbon (see Tables 3.4 and 3.6). Sorption of CT onto carbon could favor dichloroelimination products since CT could stay longer on these carbon impurities, thus allowing a sequential two-electron transfer from the metal to form the dichlorocarbene intermediate.

On the other hand, solution pH influences the types of predominant oxides on the surface of Fe^0 and the thickness of the oxide layer. XPS spectra of Peerless cast Fe^0 samples equilibrated at pH values of 7.0 and 9.3 (see Figure 3.24b) showed predominantly Fe(II) oxides on the surface of the pH 7-equilbrated Fe^0 whereas Fe(III) oxides were predominant at pH 9.3. Thus, the slower CT transformation rates at high pH could result from its surface being covered by nonreactive Fe(III) oxides as well as from

a thicker oxide layer as suggested by the depth profiling analysis of the pH-equilibrated samples (see Figure 3.28).

4. CONCLUSIONS

- Zerovalent iron metal (Fe^0) can degrade carbon tetrachloride (CT) via parallel pathways. Chloroform (CF), chloride (Cl^-), and an unidentified carbon fraction, found to be completely dechlorinated, were the main products of the reaction. CT reduction by Fe^0 depends on the solution chemistry of the medium, with pH being the most influential variable affecting rates and products. Ground water pH in the vicinity of Fe^0 permeable reactive barriers (PRBs) is high because of the corrosion of iron; in fact, pH values as high as 10 have been measured in field PRBs. Although high pH values slow the transformation of CT by Fe^0, likely because of a thicker oxide layer, the formation of the toxic product CF also tends to decrease, with a corresponding increase in benign products. This trend may also apply to the reductive dechlorination of other chlorinated compounds that are susceptible to both hydrogenolysis and dichloroelimination, such as 1,1,1- trichloroethane (TCA), tetrachloroethylene (PCE), and trichloroethylene (TCE).
- Iron purity did not significantly influence product distribution in the transformation of CT, but it did affect the rate of CT disappearance. Faster transformation rates were observed in the FE 99% Fe^0 system most likely due the high purity and low degree of oxidation of this Fe^0 with respect to the cast irons, Peerless and FF-40 mesh, which have higher contents of impurities such as carbon and oxygen.
- Pretreatment of iron surfaces by acid-washing enhanced the rate of CT degradation possibly due to removal of nonreactive oxides originally covering the metals or to the induced pitting corrosion of the metals that creates cracks or

crevices in the oxide layer. These crevices are considered reactive sites for CT transformation because the contaminant can reach the bare metal, where direct electron transfer for CT reduction occurs, by diffusing through them.

- Finally, equilibration of iron in HCO_3^-, HS^-, and Mn^{2+} solutions affected rates of CT degradation at neutral pH, but had little influence on the distribution of reaction products, except for the HS^- system where less CF was produced. Carbon disulfide (CS_2) formation may explain the decrease in the CF yield.

5. RECOMMENDATIONS

5.1 Recommendations for Remediation Applications

- CT degradation by Fe^0 under highly alkaline conditions (pH > 12.9) may have applications in above-ground treatment since CF production is minimized due to its alkaline hydrolysis. The rate of CT destruction, though, is expected to be slow. For instance, the half-life for CT reduction is 30 h for a Peerless Fe^0 mass loading of 152 g/L.
- Researchers have suggested the addition of buffering compounds such as pyrite (FeS_2) to Fe^0 PRBs, either in situ or ex situ, in order to avoid the pH increase considered to be detrimental to the long-term performance of the system. Controlling pH in this way may be favorable to rates, but it could adversely affect the distribution of reaction products. A pretreatment zone containing 10% pyrite/sand mixture was installed upgradient of a Fe^0 PRB at Dover Air Force Base (Dover, Delaware) in order to control the pH of the groundwater entering the barrier (90). Despite this, pH control within the reactive barrier was not achieved. Therefore, the no pH control alternative seems appealing since long-term studies have shown that the performance of the PRB is not seriously compromised by permeability reduction or reactivity losses due to mineral precipitation at high pH values (*46*).
- Cast irons, although impure, have a relatively good reactivity towards degrading chlorinated contaminants and do not seem to negatively influence product distribution. This suggests that further studies on mechanistic aspects of reductive dechlorination should use cast irons since they are less expensive than high purity ones, and thus the preferred materials for field applications of Fe^0 PRBs.

5.2 Recommendations for Future Research

- Examine the effect of groundwater constituents that act as Fe^0 corrosion inhibitors on the degradation of CT. Changing the surface chemistry of the iron oxides covering Fe^0 by forming complexes with inorganic (e.g., phosphates) and organic functional groups (e.g., model compounds of natural organic matter (NOM)) may affect rates and products.
- NaHS-pretreatment slightly decreased CF formation; competitive CS_2 production in this system may be the reason for the change in the selectivity of the reaction in the presence of sulfur compounds, presumably FeS precipitates, formed upon contact of NaHS and iron surfaces. It would be interesting to study how pH affects rates and products of CT degradation in NaHS-pretreated iron systems.
- Study the electrochemical degradation of CT at Fe^0 cathodes at fixed pH values to get insight into the mechanism of CT reduction and product formation. Surface characterization (e.g., Raman and XPS spectroscopy, Atomic Force Microscopy) should be used to characterize the composition and morphology of the cathodes before and after reaction.
- Prepare graphite-Fe composite materials and run CT degradation experiments with them. Graphite is a good electrical conductor. Besides, it can sorb chlorinated organic compounds such as CT and CF more strongly than pure iron surfaces. This may increase the likelihood of a sequential two-electron transfer from Fe^0, possibly changing the selectivity of the CT reaction.

LITERATURE CITED

(1) Helland, B.R.; Alvarez, P.; Schnoor, J.L. Reductive Dechlorination of Carbon Tetrachloride with Elemental Iron. *Journal of Hazardous Materials*. **1995**, *41*, 205-216.

(2) Vogel, T.; Criddle, C.; McCarty, P. Transformations of Halogenated Aliphatic Compounds. *Environ. Sci. Technol.* **1987**, *21*, 722-736.

(3) Assaf-Anid, N.; Hayes, K.F.; Vogel, T. Reductive Dechlorination of Carbon Tetrachloride by Cobalamin (II) in the Presence of Dithiothreitol: Mechanistic Study, Effect of Redox Potential and pH. *Environ. Sci. Technol.* **1994**, *28*, 246-252.

(4) Matheson, L.J.; Tratnyek, P.G. Reductive Dehalogenation of Chlorinated Methanes by Iron Metal. *Environ. Sci. Technol.* **1994**, *28*, 2045 - 2053.

(5) Devlin, J.F.; Müller, D. Field and Laboratory Studies of Carbon Tetrachloride Transformation in a Sandy Aquifer under Sulfate Reducing Conditions. *Environ. Sci. Technol.* **1999**, *33*, 1021-1027.

(6) Buschmann, J.; Angst, W.; Schwarzenbach, R.P. Iron Porphyrin and Cysteine Mediated Reduction of Ten Polyhalogenated Methanes in Homogeneous Aqueous Solution: Product Analyses and Mechanistic Considerations. *Environ. Sci. Technol.* **1999**, *33*, 1015-1020.

(7) Criddle, C.S.; McCarty. P.L. Electrolytic Model System for Reductive Dehalogenation in Aqueous Environments. *Environ. Sci. Technol.* **1991**, *25*, 973 - 978.

(8) Krone, U.E.; Thauer, R.K.; Hogenkamp, H.;Steinbach, K. Reductive Formation of Carbon Monoxide from CCl_4 and FREONs 11, 12, and 13 Catalyzed by Corrinoids. *Biochemistry*, **1991**, *30*, 2713 - 2719.

(9) Ahr, H.J.; King, L.J.; Nastainczyk, W.; Ullrich, V. The Mechanism of Chloroform and Carbon Monoxide Formation from Carbon Tetrachloride by Microsomal Cyrochrome P-450. *Biochemical Pharmacology*. **1980**, *29*, 2855-2861.

(10) Kriegman-King, M.R.; Reinhard, M. Transformation of Carbon Tetrachloride in the Presence of Sulfide, Biotite, and Vermiculite. *Environ. Sci. Technol.* **1992**, *26*, 2198-2206.

(11) Kriegman-King, M.R.; Reinhard, M. Transformation of Carbon Tetrachloride by Pyrite in Aqueous Solution. *Environ. Sci. Technol.* **1994**, *28*, 692-700.

(12) Chiu, Pei-Chun.; Reinhard, M. *Environ. Sci. Technol.* Transformation of Carbon Tetrachloride by Reduced Vitamin B_{12} in Aqueous Cysteine Solution. **1996**, *30*, 1882-1889.

(13) de Best, J.H.; Hunneman, P.; Doddema, H.J.; Jansen, D.B.; Harder, W. Transformation of Carbon Tetrachloride in an Anaerobic Packed-Bed Reactor without Addition of Another Electron Donor. *Biodegradation.* **1999**, *10*, 287-295.

(14) Pecher, K.; Haderlein, S.B.; Schwarzenbach, R.P. Reduction of Polyhalogenated Methanes by Surface-Bound Fe(II) in Aqueous Suspensions of Iron Oxides. *Environ. Sci. Technol.* **2002**, *36*, 1734 - 1741.

(15) Wagner, A.J.; Vecitis, C.; Fairbrother, D.H. Electron-Stimulated Reactions in Carbon Tetrachloride/Water (Ice) Films. *J. Phys. Chem. B.* **2002**, *106*, 4432-4440.

(16) Scherer, M.M.; Richter, S.; Valentine, R.L.; Alvarez, P.J.J. Chemistry and Microbiology of Permeable Reactive Barriers for *In Situ* Groundwater Clean up. Critical Reviews in Environmental Science and Technology, **2000**, *30*, 363-411.

(17) Deng, B.; Hu, S. Reductive Dechlorination of Chlorinated Solvents on Zerovalent Iron Surfaces. *Physicochemical Groundwater Remediation;* Edited by Smith and Burns, Kluwer Academic/Plenum Publishers, **2001**; Chapter 7. pp 139-159.

(18) Warren, K.D.; Arnold, R.G.; Bishop, T.L.; Lindholm, L.C.; Betterton, E.A. Kinetics and Mechanism of Reductive Dehalogenation of Carbon Tetrachloride Using Zero-Valence Metals. *Journal of Hazardous Materials*. **1995**, *41*, 217 - 227.

(19) Lipczynska-Kochany, E.; Harms, S.; Milburn, R.; Sprah, G.; Nadarajah, N. Degradation of Carbon Tetrachloride in the presence of Iron and Sulfur Containing Compounds. *Chemosphere.* **1994**, *29,* 1477-1489.

(20) Butler, E.C.; Hayes, K.F. Factors Influencing Rates and Products in the Transformation of Trichloroethylene by Iron Sulfide and Iron Metal. *Environ. Sci. Technol.* **2001**, *35*, 3884 - 3891.

(21) Tratnyek, P.G.; Scherer, M.M.; Deng, B.; Hu, S. Effect of Natural Organic Matter, Anthropogenic Surfactants, and Model Quinones on the Reduction of Contaminants by Zero-Valent Iron. *Wat. Res.* **2001**, *18*, 4435-4443.

(22) Agrawal, A.; Ferguson, W.J.; Gardner, B.O.; Christ, J.A.; Bandstra, J.Z.;Tratnyek, P.G. Effects of Carbonate on the Kinetics of Dechlorination of 1,1,1-Trichloroethane by Zero-Valent Iron. *Environ. Sci. Technol.* **2002**, *36*, 4326-4333.

(23) Dahmke, A.; Köber, E. R.; Schäfer, D. Laboratory and Field Results of Fe(0) Reaction Walls – A First Resume. In: Bjerg PL, Engesgaard P, Krom TD (eds) *Groundwater 2000, Proceedings of the International Conference on Groundwater Research,* Copenhagen, pp 395-396.

(24) Köber, R.; Schliker, O.; Ebert, M.; Dahmke, A. Degradation of Chlorinated Ethylenes by Fe^0: Inhibition Processes and Mineral Precipitation. *Environmental Geology.* **2002**, *41*, 644-652.

(25) Dries, J.; Bastiaens, L.; Springael, D.; Diels, L. Kinetics of Trichloroethylene (TCE) Reduction by Zero-Valent Iron: Effect of Medium Composition. *Groundwater Quality: Natural and Enhanced Restoration of Groundwater Pollution. Proceedings of the Groundwater Quality 2001 Conference,* Shefield, UK, pp 397-402.

(26) Su, C.; Puls, R.W. Kinetics of Trichloroethene Reduction by Zerovalent Iron and Tin: Pretreatment Effect, Apparent Activation Energy, and Intermediate Products. *Environ. Sci. Technol.* **1999**, *33*, 163-168.

(27) Davies, A.; Fennemore, G.G.; Peck, C.; Walker, C.R.; McIlwraith, J.; Thomas, S. Degradation of Carbon Tetrachloride in a Reducing Groundwater Environment: Implications for Natural Attenuation. *Applied Geochemistry*. **2003**, *18*, 503-525.

(28) Butler, E.; and Hayes, K. Kinetics of the Transformation of Halogenated Aliphatic Compounds by Iron Sulfide. *Environ. Sci. Technol*. **2000,** *34*, 422-429.

(29) McCormick, M.L.; Bouwer, E.J.; Adriaens, P. Carbon Tetrachloride Transformation in a Model Iron-Reducing Culture: Relative Kinetics of Biotic and Abiotic Reactions. *Environ. Sci. Technol.* **2002**, *36*, 403-410.

(30) Eweis, J.B.; Ergas, S.J.; Chang, D.P.Y.; Schroeder, E.D. *Bioremediation Principles*; McGraw- Hill, **1999**. pp. 136-137.

(31) Bekins, B.; Rittmann, B.E.; MacDonald, J.A. Natural Attenuation Strategy for Groundwater Cleanup Focuses on Demonstrating Cause and Effect. *EOS Transactions, American Geophysical Union*. **2001**, *82*, 1-5.

(32) Klausen, J.; Vikesland, P.J.; Kohn, T.; Burris, D.R.; Ball, W.P.; Roberts, A.L. Longevity of Granular Iron in Groundwater Treatment Processes: Solution Composition Effects on Reduction of Organohalides and Nitroaromatic Compounds. *Environ. Sci. Technol.* **2003**, *37*, 1208-1218.

(33) Schwarzenbach, R.P.; Gschwend, P.M. Imboden, D.M. *Environmental Organic Chemistry*; John Wiley & Sons, **1993**. pp.

(34) Johnson, T.L.; Fish, W.; Gorby, Y.A.; Trantyek, P.G. Degradation of Carbon Tetrachloride by Iron Metal: Complexation Effects on the Oxide Surface. *Journal of Contaminant Hydrology*. **1998**, *29*. 2752-2763.

(35) Johnson, T.L.; Scherer, M.M.; Tratnyek, P.G. Kinetics of Halogenated Organic Compound Degradation by Iron Metal. *Environ. Sci. Technol.* **1996**, *30*, 2634-2640.

(36) Scherer, M.M.; Westall, J.C.; Ziomec-Moroz, M.; Tratnyek, P.G. Kinetics of Carbon Tetrachloride Reduction at an Oxide-Free Iron Electrode. *Environ. Sci. Technol.* **1997**, *31*, 2385-2391.

(37) Perlinger, J.A.; Venkataphaty, J.A. Linear Free Energy Relationships for Polyhalogenated Alkane Transformation by Electron Transfer Mediators in Model Aqueous Systems. *J. Phys. Chem. A*. **2000**, *104*, 2752-2763.

(38) Balko, B.A.; Tratnyek, P.G. Photoeffects on the Reduction of Carbon Tetrachloride by Zero-Valent Iron. *J. Phys. Chem. B*, **1998**, *102*, 1459-1465.

(39) Liu, Z.; Arnold, R.G.; Betterton, E.A. Electrolytic Reduction of Chlorinated Solvents-Kinetics, Electrode Selectivity, and Electrode Materials. *International Conference on Remediation of Chlorinated Recalcitrant Compounds*, May 18-21, 1998, Monterrey, CA; Batelle Press: Columbus, Ohio, **1998**, 473 - 478.

(40) Liu, Z.; Arnold, R.G.; Betterton, E.A.; Festa, K.D. Electrolytic Reduction of CCl_4-Effects of Cathode Material and Potential on Kinetics, Selectivity, and Product Stoichiometry. *Environmental Engineering Science.* **1999**, *16*, 1-13.

(41) Li, T.; Farell, J. Electrochemical Investigation of the Rate Limiting Mechanisms for Trichloroethylene and CT Reduction at Iron Surfaces. *Environ. Sci. Technol.* **2001**, *35*, 3560-3565.

(42) Gotpagar, J.; Lyuksyutov, S.; Cohn, R.; Grulk, E.; Bhattacharyya, D. Reductive Dehalogenation of Trichloroethylene with Zero-Valent Iron: Surface Profiling Microscopy and Rate Enhacement Studies. *Langmuir*. **1999**, *15*, 8412-8420.

(43) Ruiz, N.; Seal,S.; Reinhart, D. Surface Chemical Reactivity in Selected Zero-Valent Iron Samples Used in Groundwater Remediation. *Journal of Hazardous Materials B.* **2000**, *80*, 107-117.

(44) Geiger, C.L.; Ruiz, N.E.; Clausen, C.A.; Reinhart, D.R.; Quinn, J.W. Ultrasound Pretreatment of Elemental Iron: Kinetic Studies of Dehalogenation Reaction Enhancement and Surface Effects. *Water Research.* **2002**, 36, 1342-1350.

(45) Hassan, S.M. Reduction of Halogenated Hydrocarbons in Aqueous Media: I. Involvement of Sulfur in Iron Catalysis. *Chemosphere*, **2000**, *40*, 1357-1363.

(46) Mackenzie, P.D.; Horney, D.P.; Sivavec, T.M. Mineral Precipitation and Porosity Losses in Granular Iron Columns. *Journal of Hazardous Materials*. **1999**, *68*, 1-17.

(47) Stumm, W.; Morgan, J.J. *Aquatic Chemistry;* John Wiley & Sons, **1996.**

(48) Puls, R. W; Blowes, D.W.; Gillham, R.W. Long-term Performance Monitoring for a Permeable Reactive Barrier at the U.S. Coast Guard Support Center, Elizabeth City, North Carolina. *Journal of Hazardous Materials*. **1999**, *68*, 109-124.

(49) Phillips, D.H.; Gu, B.; Watson, D.B.; Roh, Y.; Liang, L.; Lee, S.Y. Performance Evaluation of a Zerovalent Iron Reactive Barrier: Mineralogical Characteristics. *Environ. Sci. Technol.* **2000**, *34*, 4169 - 4176.

(50) Chen, J.-L; Al-Abed, S.R.; Ryan, J.A.; Li, Z. Effects of pH on Dechlorination of Trichloroethylene by Zero-Valent Iron. *Journal of Hazardous Materials B*. **2001**, *41*, 205-216.

(51) Allowitz, M.J.; Scherer, M.M. Kinetics of Nitrate, Nitrite, and Cr(VI) Reduction by Iron Metal. *Environ. Sci. Technol*. **2002**, *36*, 299-306.

(52) Scherer, M.M.; Balko, B.; Tratnyek, P.G. *The Role of Oxides in Reduction Reactions at the Metal-Water Interface;* Sparks, D., Grundl, T., Eds.; ACS Symposium Series 715; American Chemical Society: Washington, DC, **1998**; pp 301-322.

(53) Logue, B.A.; Westall, J.C. Kinetics of Reduction of Nitrobenzene and Carbon Tetrachloride at an Iron-Oxide Coated Gold Electrode. *Environ. Sci. Technol.* **2003**, *37*, 2356-2362.

(54) Arnold, W.; and Roberts, L. Pathways and Kinetics of Chlorinated Ethylene and Chlorinated Acetylene Reaction with Fe(0) Particles. *Environ. Sci. Technol*. **2000,** *34*, 1794-1805.

(55) Gaspar, D.J.; Lea, S.A.; Engelhard, M.H.; Baer, D. R.; Miehr, R.; Tratnyek, P.G. Evidence for Localization of Reaction Upon Reduction of Carbon Tetrachloride by Granular Iron *Langmuir*. **2002**, *18*, 7688-7693.

(56) Deng, B.; Campbell, T.J.; Burris, D.R. Hydrocarbon Formation in Metallic Iron/Water Systems. *Environ. Sci. Technol.* **1997**, *31*, 1185 - 1190.

(57) Burris, D.R.; Campbell, T.J.; Manoranjan, V.S. Sorption of Trichloroethylene and Tetrachloroethylene in a Batch Iron-Water System. *Environ. Sci. Technol.* **1995**, *29*, 2850-2855.

(58) O'Loughlin, E.J.; Kemner, K.M.; Burris, D.R. . Effects of Ag^{I}, Au^{III}, and Cu^{II} on the Reductive Dechlorination of Carbon Tetrachloride by Green Rust. *Environ. Sci. Technol.* **2003**, *37*, 2095-2912.

(59) Talbot, D.; Talbot, J. *Corrosion Science and Technology*; CRC Press LLC, Boca Raton, Florida, **1998**.

(60) Sivavec, T.M.; Horney, D.P.; Baghel, S.S. Reductive Dechlorination of Chlorinated Ethenes by Iron Metal and Iron Sulfide Minerals. *Preprints of Extended Abstracts Presented at the I&EC Special Symposium.* Sept. 17-20, **1995**, Atlanta, GA. American Chemical Society: Washington, D.C. pp 42-45.

(61) Farrell, J.; Kason, M.; Melitas, N. Li, T. Investigation of the Long-Term Performance of Zero-Valent Iron for Reductive Dechlorination of Trichloroethylene. *Environ. Sci. Technol.* **2000**, *34*, 514-521.

(62) Klausen, J.; Tröber, S.P.; Haderlein, S.B.; Schwarzenbach, R.P. Reduction of Substituted Nitrobenzenes by Fe(II) in Aqueous Mineral Suspensions. *Environ. Sci. Technol.* **1995**, *29*, 2396-2404.

(63) Pecher, K.; Kneedler, E.M.; Tonner, B.P. Identification and Characterization of Iron Surfaces Capable of Reductive Transformation of Pollutants Using Synchrotron X- Ray Absorption Spectroscopy Techniques. *Preprints of Papers Presented at the 217th ACS National Meeting*. Anaheim, CA. American Chemical Society, Vol. 39(1), Mar. 1999, pp. 292 –294.

(64) Watts, J.F. *An Introduction to Surface Analysis by Electron Spectroscopy*. Oxford University Press: Royal Microscopical Society. **1990**, p. 26.

(65) Vaughan, D.J.; Patrick, R.A.D. *Mineral Surfaces*. Chapman & Hall. **1995**. pp. 35-37.

(66) Good, N.E.; Winger, G.D.; Winter, W.; Connolly, T.N.; Isawa, S.; Singh, R.M.M. Hydrogen Ion Buffers for Biological Research. *Biochemistry*. **1966,** *5*, 467-477.

(67) Dionex Corporation. *IonPac AS11 Manual*. Doc. No. 034791-07. **2002**, pp 19-21.

(68) Wachs, I.E. *Characterization of Catalytic Materials. Materials characterization series: surfaces, interfaces, thin films*; Butterworth-Heinemann: Stoneham, MA, 1992. pp. 19-25.

(69) Chambers, C.; Holliday, A.K. *Modern Inorganic Chemistry*. Butterworths. **1975**. p. 181.

(70) Amatore, C.; Savéant, J-M. Mechanism and Kinetic Characteristics of the Electrochemical Reduction of Carbon Dioxide in Media of Low Proton Availability. *J. Am. Chem. Soc.* **1981**, *103*, 5021-5023.

(71) McCormick, M.L.; Adriaens, P. The Fate of Carbon Tetrachloride in a Defined Iron Reducing Culture: Product Formation via Biotic and Abiotic Pathways. *Preprints of Papers Presented at the 220th ACS National Meeting*, Aug. 20-24, **2000**, Washington, DC., American Chemical Society: Washington, D.C, Vol. 40 (2), pp 357 – 361.

(72) Jeffers, P.M.; Ward, L.M.; Woytowitch, L.M.; Wolfe, N.L. Homogeneous Hydrolysis Rate Constants for Selected Chlorinated Methanes, Ethanes, Ethenes, and Propanes *Environ. Sci. Technol.* **1989**, *23*, 965-969.

(73) Gäb, S.; Schmitzer, J.; Turner, W. V.; Korte, F. Mineralization of CCl_4 and CCl_2F_2 on Solid Surfaces. *Zeitschrift fuer Naturforschung, Teil B: Anorganishe Chemie, Organische Chemie*. **1980**, *35B*, 946-952.

(74) House, J.E. *Principles of Chemical Kinetics*; Wm. C. Brown Publishers, Dubuque, IA, **1997**, pp 38-40.

(75) Stumm, W. *Aquatic Surface Chemistry;* Wiley: New York, **1987**; p 97.

(76) Regazzoni, A.E.; Blesa, M.A.; Maroto, A.J.G. Interfacial Properties of Zirconium Dioxide and Magnetite in Water. *Journal of Colloid and Interface Science*.**1983**. *91*.560-569.

(77) Cromieres, L.; Moulin, V.; Fourest, B.; Giffaut, E. Physicochemical Characterization of the Colloidal Hematite/Water Interface: Experimentation and Modelling. *Colloids and Surfaces A: Physicochemical and Engineering Aspects*. **2002**. *202*. 101-115.

(78) Mills, P.; Sullivan, J.L. A Study of the Core Level Electrons in Iron and its Three Oxides by Means of X-ray Photoelectron Spectroscopy. *J. Phys. D: Appl. Phys*. **1983**, *16*, 723 – 732.

(79) Ritter, K.; Odziemkowsky, M.S.; Gillham, R.W. An In Situ Study of the Role of Surface Films on Granular Iron in the Permeable Iron Wall Technology. *Journal of Contaminant Hydrology*. **2002,** *55*, 87-111.

(80) Bohnsack, G. The Solubility of Magnetite in Water and in Aqueous Solutions of Acid and Alkali. Hemisphere Publishing Corporation. 1987.

(81) Robinson, E.A. The Reaction of Dichloromethane with Water and with Phenoxy Ions. *J. Chem. Soc*. **1961**, 1663.

(82) Huang, Y.H.; Zhang, T.C.; Shea, P.J.; Comfort, S.D. Effect of Oxide Coating and Selected Cations on Nitrate Reduction by Iron Metal. *J. Environ. Quality*. **2003**, *32*, 306-1315.

(83) Erbs, M.; Hansen, H.C.B.; Olsen, C.E. Reductive Dechlorination of Carbon Tetrachloride Using Iron(II) Iron(III) Hydroxy Sulfate (Green Rust). *Environ. Sci. Technol.* **1999**, *33*, 307-311.

(84) Asami, K.; Hashimoto, K. X-ray Photoelectron Spectroscopy for Corrosion Studies. *Langmuir*. **1987**, *3*, 897-904.

(85) Phillips, D.H.; Gu, B.; Watson, D.B.; Roh, Y. Impact of Sample Preparation on Mineralogical Analysis of Zero-Valent Iron Reactive Barrier Materials. *J. Environ. Quality*. **2003**, *32*, 1299-1305.

(86) Hunter, R.J. *Zeta Potential in Colloid Science*; Academic Press. **1981**. p. 17-21.

(87) Choi, W.; Hoffmann, M.R. Photoreductive Mechanism of CCl_4 Degradation on TiO_2 Particles and Effects of Electron Donors. *Environ. Sci. Technol.* **1995**, *29*, 1646-1654.

(88) Myers, R.J. The New Low Value for the Second Dissociation Constant for H_2S. *Journal of Chemical Education.* **1986**, *63*, 687-690.

(89) Licht, S.; Manassen, J. The Second Dissociation Constant of H_2S. *J. Electrochem Soc.* **1987**, *134*, 918-921.

(90) Remediation Technologies Development Forum. Permeable Reactive Barriers Action Team Meeting. February 16-17. **2000**. (http:/www.rtdf.org/public/perbarr/minutes).

(91) Skoog, D.A.; West, D.M.; Holler, F.J. *Fundamentals of Analytical Chemistry*; Thomson Learning, Inc., **1996**. pp. 33-39.

APPENDIX A

Detailed Experimental Procedures

Preparation of buffer solutions

Good's buffers were used to prepare aqueous solutions over the pH range from 7 to 10.2. The following equations were used to calculate the amount of acid and salt of the organic buffer in order to achieve a desired pH.

$$pH = pK_a + \log\frac{[Salt]}{[Acid]} \qquad (1)$$

$$C_T = [Acid] + [Salt] \qquad (2)$$

where

pH = desired pH

pK_a = pK_a of the buffer system at 25° C

[Salt] = concentration of the salt form of the buffer

[Acid] = concentration of the acid form of the buffer

C_T = Total concentration of buffer

Example 1. How to prepare a pH 7 buffer solution.

- Use HEPES, (N- [2-hydroxyethyl] piperazine- N'- [2-ethanesulfonic acid]), because its pK_a is 7.5 at 25° C, so that it can be used to control pH in the range from 6.8 to 8.2.
- The total concentration of buffer is set to 0.05 M (C_T = 0.05 M)
- From eq 1

$$\log\frac{[Salt]}{[Acid]} = pH - pK_a = 7.0 - 7.5 = -0.5$$

$$\frac{[\text{Salt}]}{[\text{Acid}]} = 10^{-0.5} = 0.316 \qquad (3)$$

- Solve for [Acid] and [Salt] by combining eqs (2) and (3)

$[\text{Acid}] = 0.038\ \text{M}$

$[\text{Salt}] = 0.012\ \text{M}$

- Calculate the amount of acid and salt needed to prepare 500 mL of 0.05 M HEPES buffer.

The molecular weights of the acid and sodium salt of HEPES are 238.3 g/mol and 260.3 g/mol, respectively. Then,

Amount of acid = 0.038 moles/L × 238.3 g/mol × 0.5 L = 4.53 g

Amount of salt = 0.012 moles/L × 260.3 g/mol × 0.5 L = 1.56 g

When only the acid form of the buffer was available, the pH was adjusted by adding sodium hydroxide.

Example 2. How to prepare a pH 9.3 buffer solution.

- Use CHES, (2 – [N-cyclohexylamino] ethanesulfonic acid), because its pK_a is 9.3 at 25° C, so that it can be used to control pH in the range from 8.6 to 10.0.
- The total concentration of buffer is set to 0.05 M (C_T = 0.05 M)
- From eq 1

$$\log\frac{[\text{Salt}]}{[\text{Acid}]} = \text{pH} - \text{pK}_a = 9.3 - 9.3 = 0.0$$

$$\frac{[\text{Salt}]}{[\text{Acid}]} = 10^{0.0} = 1 \qquad (4)$$

- Solve for [Acid] and [Salt] by combining eqs (2) and (4)

$[\text{Acid}] = [\text{Salt}] = 0.025\ \text{M}$

- Calculate the amount of acid and NaOH needed to prepare 500 mL of 0.05 M CHES buffer.

  The molecular weights of the acid form of CHES and of NaOH are 207.3 g/mol and 40 g/mol, respectively. Then,

  Amount of acid = 0.05 moles/L × 207.3 g/mol × 0.5 L = 5.18 g

  Amount of NaOH = 0.025 moles/L × 40 g/mol × 0.5 L = 0.5 g

The following table summarizes the amounts of acid and salt/NaOH needed to prepare 500 mL of 0.05 M Good's buffer solutions (7 < pH < 10.2) as well as the amount of NaOH needed to prepare 500 mL of 0.02 M and 0.1 M NaOH aqueous solutions of pH values of 12 and 12.9, respectively.

Table A1. Recipes for preparation of buffer solutions

Desired pH	Buffer	pK_a	Amount of acid (g)	Amount of salt or NaOH (g)
7.0	HEPES	7.5	4.53	1.56
8.4	HEPES	7.5	0.67	5.78
8.4	CHES	9.3	5.18	0.11
9.3	CHES	9.3	5.18	0.5
10.2	CAPS[a]	10.4	5.53	0.4
12	NONE	--	--	0.4
12.9	NONE	--	--	2

[a] CAPS (3- (cyclohexylamino-1-propane sulfonic acid)); pH 10.2 solution prepared by adjusting pH with NaOH; MW = 221.32 g/mol

Preparation of methanolic CT stock solution

Add 77 µL of pure CT to 19.8 mL of oxygen-free methanol.

$$\left(\frac{77\,\mu L}{19800\,\mu L + 77\,\mu L}\right) \times 1.590\,\frac{g}{mL} \times 1000\,\frac{mL}{L} \times \frac{1\,mole\,CT}{154\,g} = 4.00 \times 10^{-2}\ M$$

Step by step procedure to set up a typical kinetic batch experiment

1. Weigh 1.2 g of Fe^0 into 8-mL vials. The number of vials to prepare depends on how many experimental data points are desired to describe the kinetics of contaminant disappearance. In this work, at least 12 reaction vials were prepared.
2. Place vials inside anaerobic glove box.
3. Add 7.8 mL of oxygen-free buffer solution to each vial using an automatic pipettor, so that the vials do not have headspace.
4. Add 80 µL of a 40 mM CT stock solution prepared in methanol to each vial to give an initial CT concentration of approximately 0.4 mM and 1% v/v in methanol.
5. Cap vial with a Teflon-lined butyl rubber septum and a crimp-seal it after placing an aluminum seal on top of the septum.
6. Remove vials from glove box and place them in rotary shaker located inside incubator kept at 25°C.
7. Sacrifice vials at regular time intervals over a period covering at least two to three half-lives. For this purpose, remove vials from incubator, centrifuge them for at least five minutes, remove aluminum seal from vial with decrimper in the fume hood area, and take aqueous samples from the supernatant as needed for quantification of products with gas chromatography and ion chromatography.
8. Prepare control and blank vials immediately before preparing reaction vials. Control vials contain CT and no Fe^0 whereas blank vials contain Fe^0 but no CT. Sample control and blank vials at the same time as reaction vials. Control vials are needed to assess whether transformation processes (e.g., volatilization) other

than chemical transformation of the contaminant by Fe^0 are taking place over the course of a typical kinetic experiment. Blank vials are prepared to measure background aqueous concentration of chloride (Cl^-) originating from either the buffer solution or dissolving from Fe^0. Background Cl^- concentrations are subtracted from the concentrations measured in reaction vials.

9. Follow steps 1 to 8 for setting up the experiments involving FE 99% Fe^0 equilibrated in 0.05 M HEPES buffer solution containing 1 mM concentrations of NaHS, $NaHCO_3$, or $MnBr_2$. In this case, however, after addition of the buffer solution to the vials inside the glove box (step 3), cover the vials with Teflon-lined rubber septum, and allow equilibration for a 12-h period before proceeding to step 4.

Note: Preliminary experiments can be done to estimate how long takes for the contaminant to disappear under a given experimental condition, so that sampling in the definitive experiment is done over two to three half-lives.

Preparation of standards for GC and IC analysis

Standards for GC/ECD analysis

1. Add 18.5 mL of isooctane to a 22-mL vial, and then inject 9 μL of pure CT and 8 μL of pure CF into the isooctane with a 10-μL syringe. Cap vial with Teflon-lined rubber septum and gently shake it by hand. This gives CT and CF concentrations of approximately 5×10^{-3} M. See the following calculations:

CT:

$$\left(\frac{9\,\mu L}{18500\,\mu L + 9\,\mu L}\right) \times 1.590\,\frac{g}{mL} \times 1000\,\frac{mL}{L} \times \frac{1\,mole\,CT}{154\,g} = 5.02 \times 10^{-3}\ M$$

CF:

$$\left(\frac{8\,\mu L}{18500\,\mu L + 8\,\mu L}\right) \times 1.492\,\frac{g}{mL} \times 1000\,\frac{mL}{L} \times \frac{1\,mole\,CT}{119.5\,g} = 5.00 \times 10^{-3}\ M$$

In the above equations 1.590 g/mL and 1.492 g/mL are the densities of CT and CF. 154 g/mol and 119.5 g/mol are the molecular weights of CT and CF.

2. Prepare a 1×10^{-5} M CT and CF stock solution by injecting 10 uL of the 5×10^{-3} M solution into 5 mL of isooctane contained in an 8-mL vial. Cap vial with Teflon-lined rubber septum and gently shake vial by hand.

3. Use stock solution 1×10^{-5} M in CT and CF to prepare standards in 1.5-mL GC vials. For example, to prepare a standard 8×10^{-6} M in CT and CF, add 205 μL of isooctane to the vial, and then add 820 μL of the 1×10^{-5} M solution. The following table summarizes the volumes of isooctane and 1×10^{-5} M stock solution needed to prepare the calibration standards.

Table A2. Calibration standards for GC/ECD analysis

[CT] or [CF], M	$V_{isooctane}$ (uL)	$V_{stock\ soln}$ (uL)
8×10^{-6}	205	820
6×10^{-6}	405	620
4×10^{-6}	610	415
2×10^{-6}	810	215
1×10^{-7}	1015	10

Standards for GC/TCD analysis

The headspace method was used to quantify the concentration of CO and CH_4 in samples and standards. This method has the advantage of quantifying the analytes by measuring their concentration in the gas phase, thus avoiding potential interferences from the aqueous matrix.

Sample and standard preparation

1. Add 18-mL of either buffer solution or aqueous sample from the reaction bottle to a 22-mL vial, rapidly cap vial with Teflon-lined rubber septum and crimp-seal it. For the standards, inject a volume of gas calibration standard of known concentration into the headspace of the vial containing the buffer solution. Before injecting the gas of interest, remove the same volume of air from the headspace to avoid the buildup of pressure. The concentration of a particular analyte in the calibration vials was determined by using the ideal gas law; an example is provided below.

Given:

[CO] = 4.5 % v/v = 0.045 mole fraction (standard from Scott Specialty gases)

V_{CO} = 100 uL = 10^{-4} L

Calculate $[CO]_{aq}$

- Estimate moles of CO injected into the system

$$n_{CO} = \frac{PV_{CO}y_{CO}}{RT} = \frac{1\text{atm} \times (10^{-4}\text{ L}) \times 0.045}{0.082\frac{\text{Latm}}{\text{molK}} \times 298.15\text{ K}} = 1.84 \times 10^{-7}\text{ moles}$$

where

P = pressure (ambient pressure = 1 atm)

R = 0.082 L-atm/mol-K (ideal gas constant)

V_{co} = volume of 4.5% v/v CO standard injected into the system

y_{co} = molar fraction of CO

T = ambient temperature (25°C = 298.15 K)

- Then

$$[CO]_{aq} = \frac{n_{CO}}{V_{soln}} = \frac{1.84 \times 10^{-7} \text{ moles}}{0.018 \text{ L}} = 1.02 \times 10^{-5} \text{ M}$$

V_{soln} = volume of buffer solution

The following table compiles the volumes of CO and CH_4 required to prepare calibration standards of different concentration.

Table A3. Calibration standards for GC/TCD analysis

V_{CO} (µL)[a]	$[CO]_{aq}$ (M)	V_{CH4} (µL)	$[CH_4]_{aq}$ (M)
100	1.02×10^{-5}	2000 [b]	4.53×10^{-6}
200	2.05×10^{-5}	50 [c]	1.14×10^{-5}
500	5.12×10^{-5}	100 [c]	2.27×10^{-5}
700	7.16×10^{-5}	150 [c]	3.41×10^{-5}
1000	1.00×10^{-4}	400 [c]	9.09×10^{-5}

[a] Use 4.5% v/v CO in N_2 Scott specialty gas mix
[b] Use 996 ppm v/v CH_4 in N_2 Scott specialty gas mix
[c] Use 10% v/v CH_4 in N_2 Scott specialty gas mix

2. Allow equilibration of the aqueous phase with the gas phase for a 2-h period to permit partitioning of the gases to the headspace.

3. Manually withdraw 500 µL of the headspace of the 22-mL vial with a gas-tight syringe and inject it into the GC/TCD for analysis.

Standards for IC analysis

1. Prepare a 1000 mg/L stock solution in Cl^- and $HCOO^-$. Add 0.076 g of sodium formate (HCOONa) and 0.0824 g of sodium chloride (NaCl) to a 50 mL volumetric flask. Fill flask to the mark with water or buffer solution.

2. Prepare calibration standards by diluting the 1000 mg/L solution. For example, to prepare a 50 mg/L standard in Cl^- and $HCOO^-$, add 1 mL of 1000 mg/L stock solution to 19 mL of water or buffer solution. The following table summarizes the volumes of stock solution and buffer required to prepare standards of a given concentration.

Table A4. Calibration standards for IC analysis

[Cl^-] or [$HCOO^-$], mg/L	V_{buffer} (mL)	$V_{stock\ soln}$ (mL)
50	19.0	1
20	19.6	0.4
10	19.8	0.2
5	19.9	0.1
2	19.96	0.04
0.5	19.99	0.01

APPENDIX B

Sample Chromatograms

GC/ECD

The retention times for CT and CF were 5.7 min and 5.1 min, respectively. The injection volume was 1 μL. The concentrations of CT and CF were 3.21×10^{-6} and 3.45×10^{-6} M. respectively.

File : c:\class-vp\chrom\marial\april03\042903.011
Method : c:\class-vp\chrom\marial\methods\zvi.met
Sample ID : std4
Vial : 6
Volume : 1
Acquired : Apr 29, 2003 19:58:12
User : System

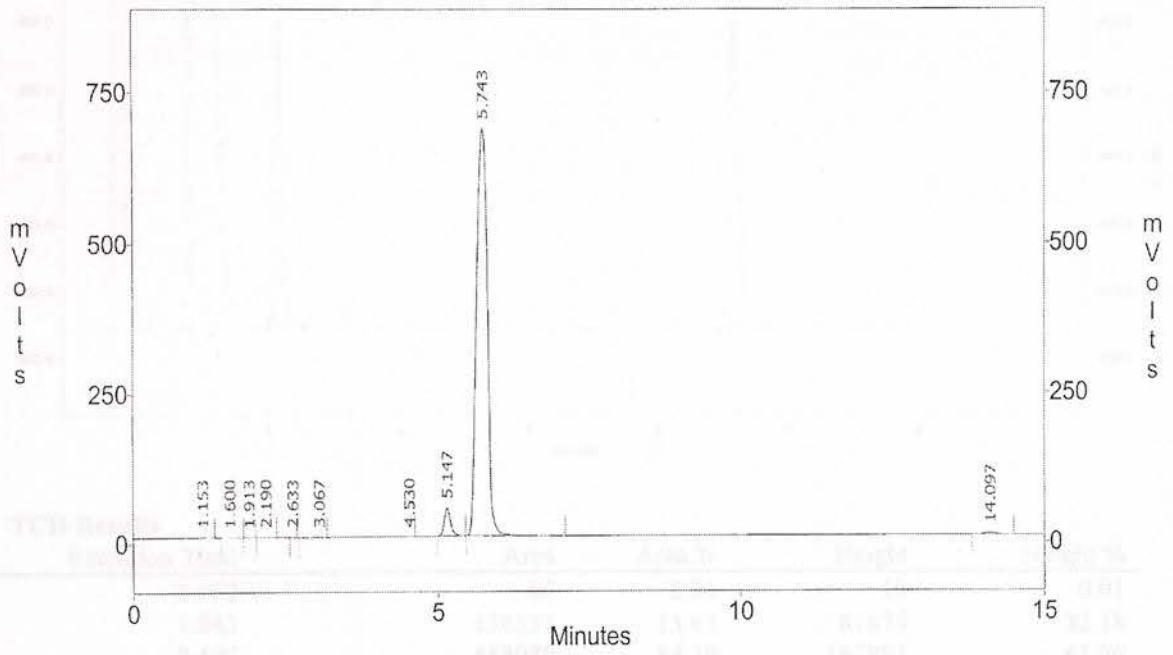

Channel B Results

Peak	Time	Area	Area %
1	1.15	3045	0.035
2	1.60	4084	0.047
3	1.91	1360	0.016
4	2.19	1746	0.020
5	2.63	832	0.010
6	3.07	3158	0.036
7	4.53	174	0.002
8	5.15	333389	3.818
9	5.74	8344245	95.566
10	14.10	39344	0.451
Totals :		8731377	100.000

GC/TCD

The retention times for CH_4 and CO were 3.07 min and 6.6 min, respectively. The injection volume was 500 μL. The concentrations of CO and CH_4 were 1.00×10^{-4} and 9.1×10^{-5} M. respectively.

Area % Report

Method Name: C:\CLASS-VP7.1.1\projects\Default\Methods\DKSTEST.MET.met
Data: C:\CLASS-VP7.1.1\Projects\Default\Data\Instrument 10004 Preview.dat
User: System
Acquired: 08/18/2002 6:46:24 PM
Printed: 08/18/2002 6:55:07 PM

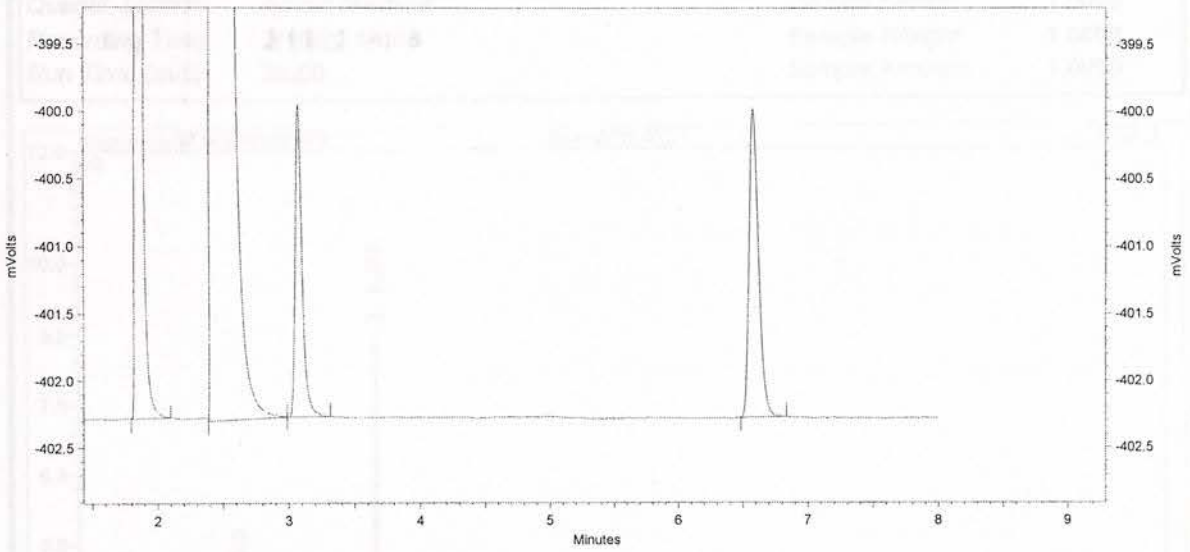

TCD Results

Retention Time	Area	Area %	Height	Height %
0.072	86	0.01	19	0.01
1.843	138533	13.62	81875	32.18
2.407	858080	84.39	167883	65.99
3.065	8391	0.83	2326	0.91
6.573	11714	1.15	2301	0.90
Totals	1016804	100.00	254404	100.00

GC/IC

The retention times for formate and chloride were 2.9 min and 5.4 min, respectively. The injection volume was 25 µL. The concentrations of formate and chloride were 5 mg/L each.

79 5ppmSTdH2Or1

Sample Name:	**5ppmSTdH2Or1**	*Injection Volume:*	**25.0**
Vial Number:	**59**	*Channel:*	**ECD_1**
Sample Type:	**unknown**	*Wavelength:*	**n.a.**
Control Program:	**Anion Program**	*Bandwidth:*	**n.a.**
Quantif. Method:	**Anion Method**	*Dilution Factor:*	**1.0000**
Recording Time:	**6/19/02 14:06**	*Sample Weight:*	**1.0000**
Run Time (min):	**20.00**	*Sample Amount:*	**1.0000**

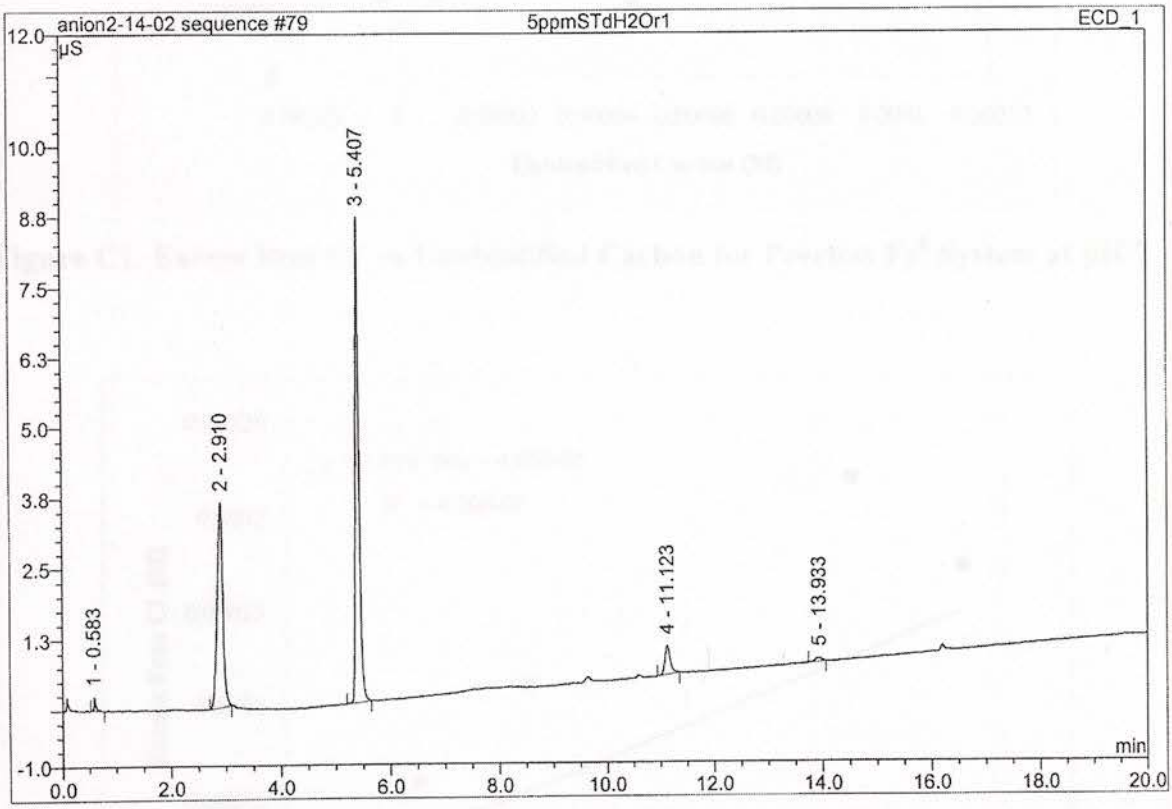

No.	Ret.Time min	Peak Name	Height µS	Area µS*min	Rel.Area %	Amount mg/L	Type
1	0.58	n.a.	0.250	0.011	0.93	n.a.	BMB
2	2.91	n.a.	3.646	0.433	36.76	n.a.	BMB
3	5.41	n.a.	8.637	0.663	56.24	n.a.	BMB
4	11.12	n.a.	0.512	0.061	5.16	n.a.	BMB
5	13.93	n.a.	0.072	0.011	0.91	n.a.	BMB
Total:			13.118	1.179	100.00	0.000	

APPENDIX C

Plots of Excess Free Chloride vs Unidentified Carbon

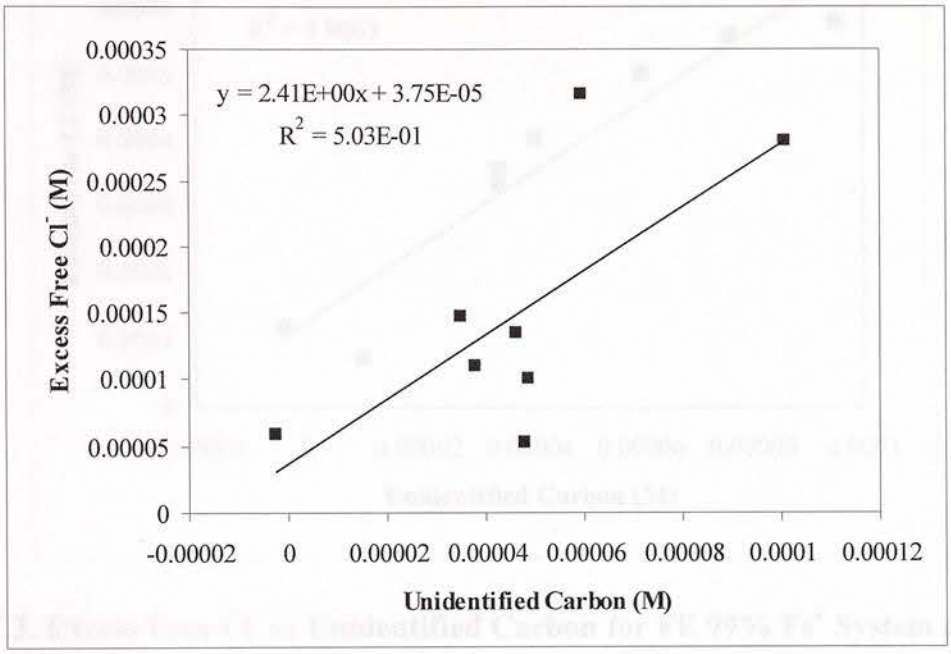

Figure C1. Excess Free Cl^- vs Unidentified Carbon for Peerless Fe^0 System at pH 7

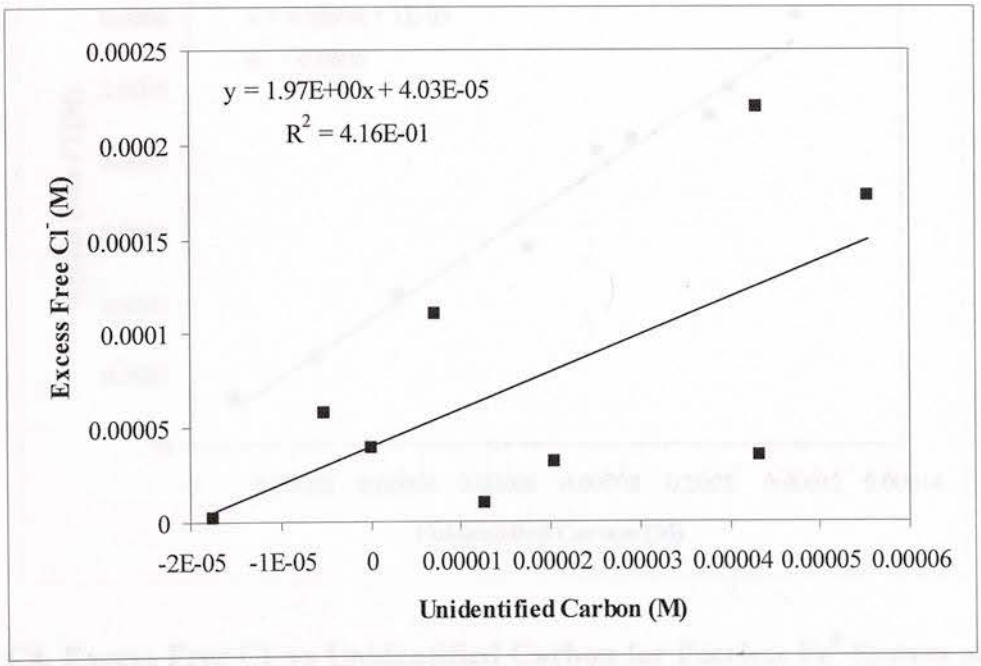

Figure C2. Excess Free Cl^- vs Unidentified Carbon for FE 93% Fe^0 System at pH 7

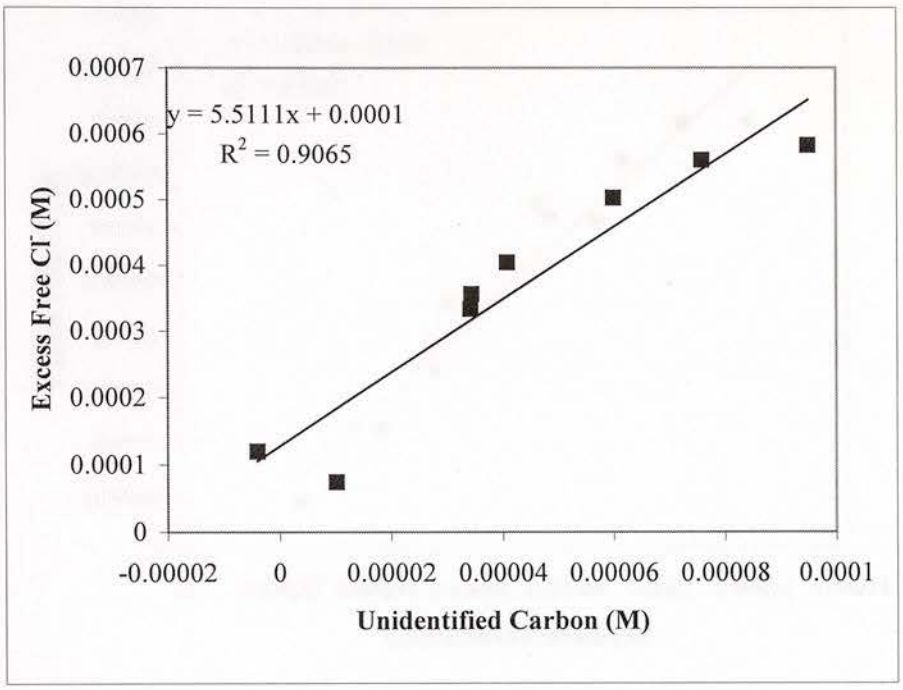

Figure C3. Excess Free Cl^- vs Unidentified Carbon for FE 99% Fe^0 System at pH 7

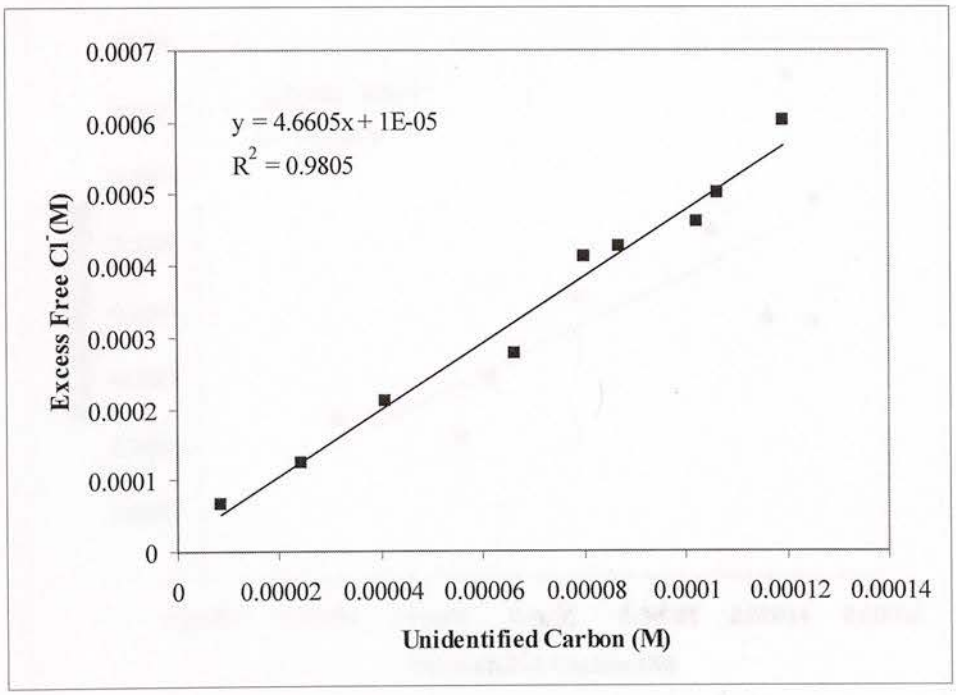

Figure C4. Excess Free Cl^- vs Unidentified Carbon for Peerless Fe^0 System at pH 8.4 with HEPES Buffer

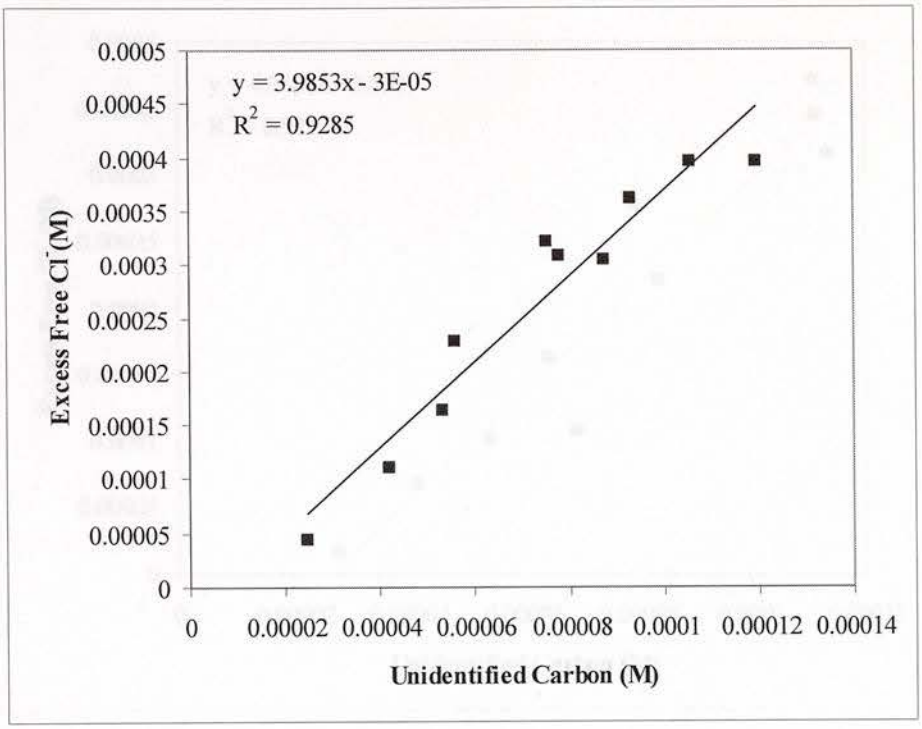

Figure C5. Excess Free Cl⁻ vs Unidentified Carbon for Peerless Fe^0 System at pH 8.4 with CHES Buffer

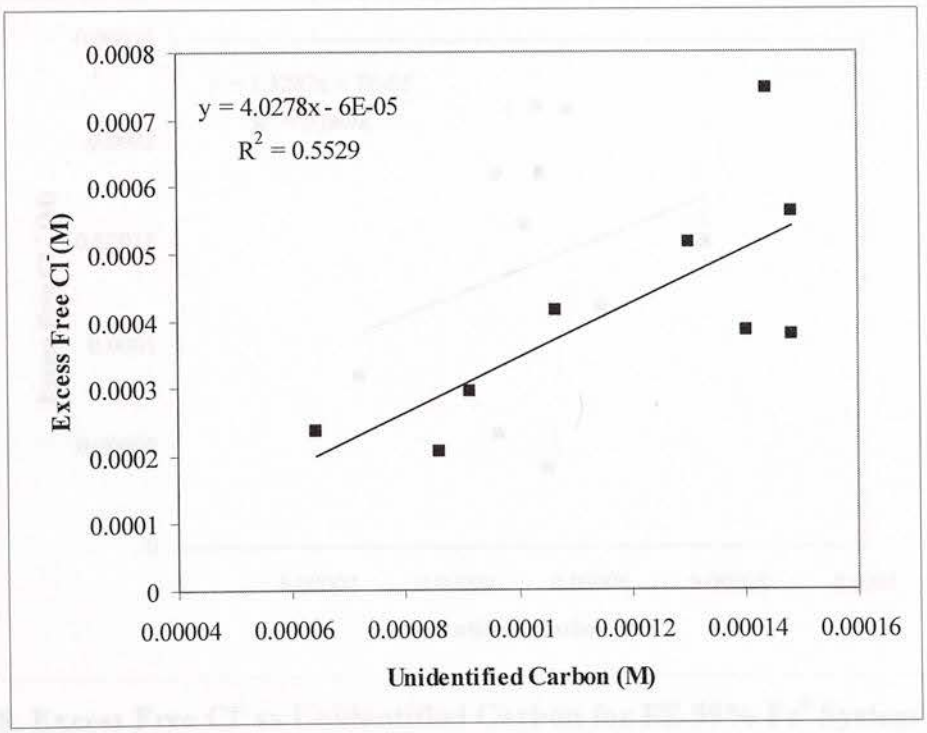

Figure C6. Excess Free Cl⁻ vs Unidentified Carbon for FF-40 mesh Fe^0 System at pH 9.3

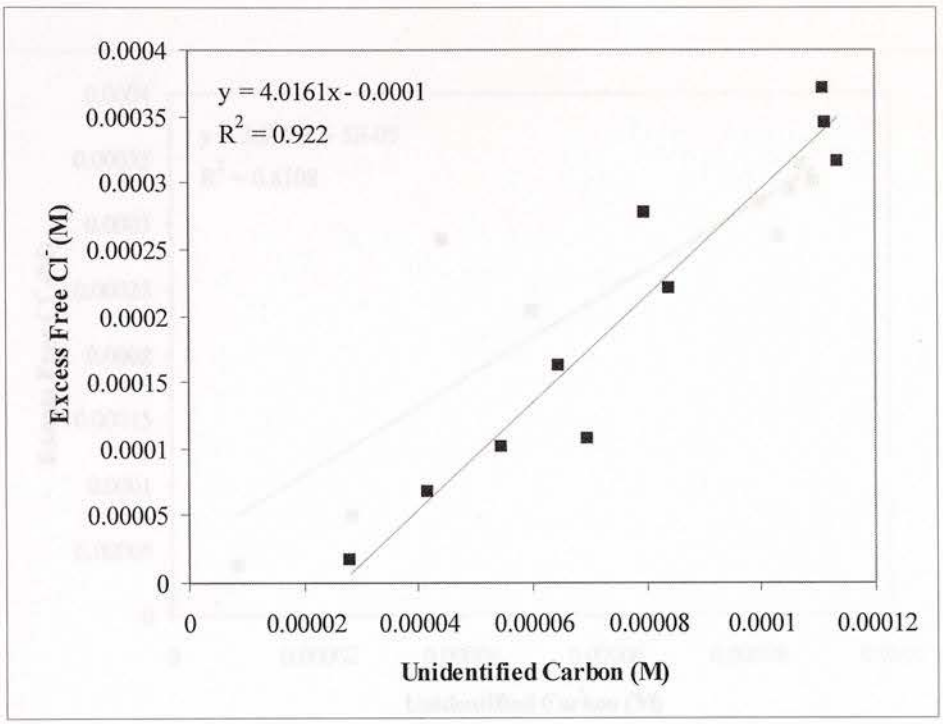

Figure C7. Excess Free Cl^- vs Unidentified Carbon for Peerless Fe^0 System at pH 9.3

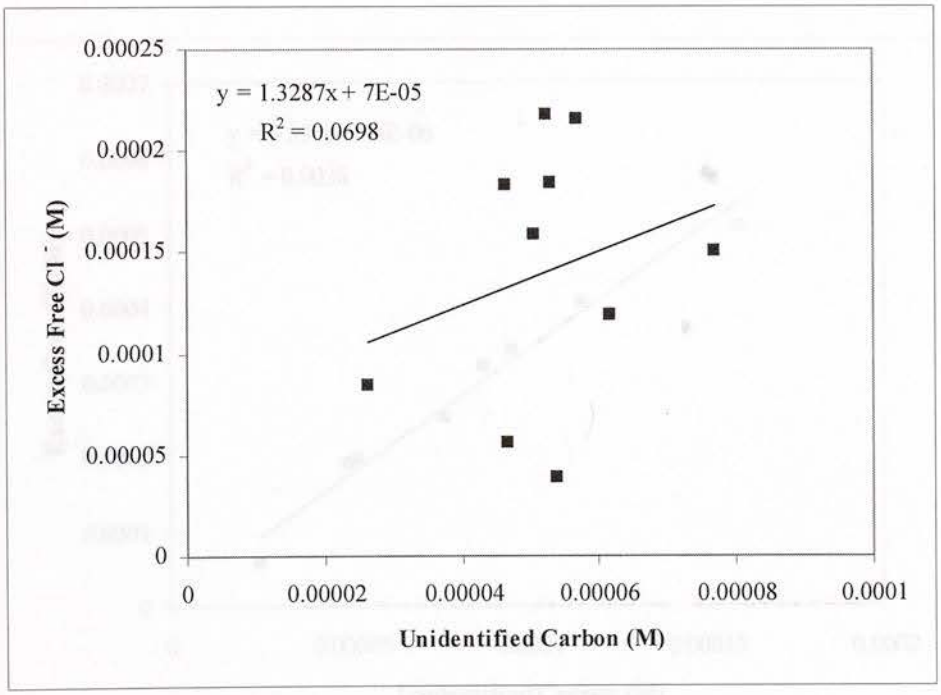

Figure C8. Excess Free Cl^- vs Unidentified Carbon for FE 99% Fe^0 System at pH 9.3

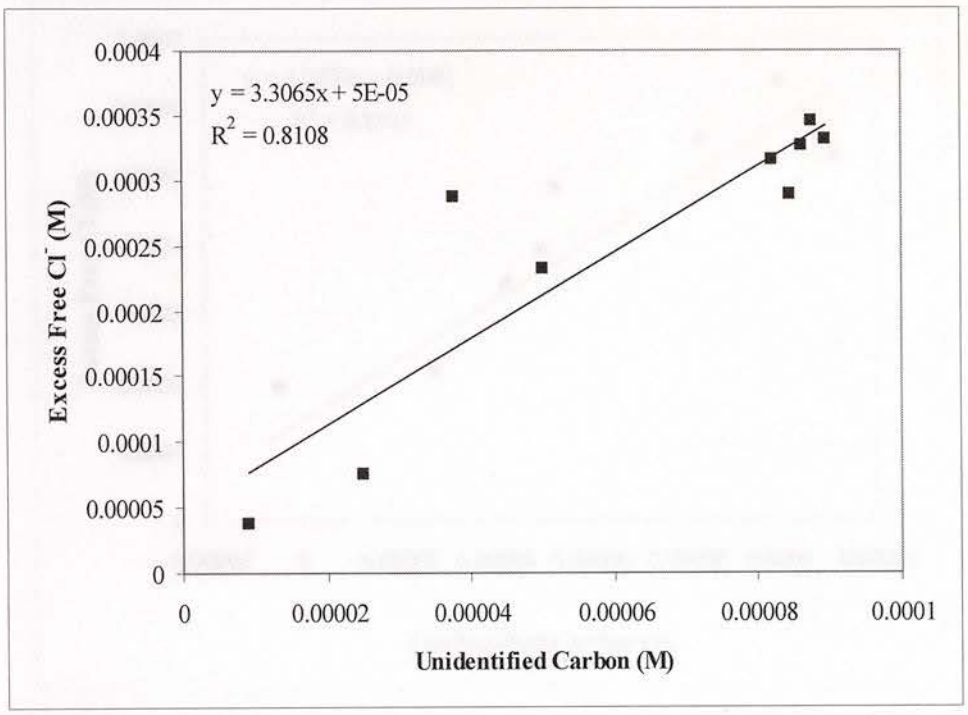

Figure C9. Excess Free Cl^- vs Unidentified Carbon for Peerless Fe^0 System at pH 10.2

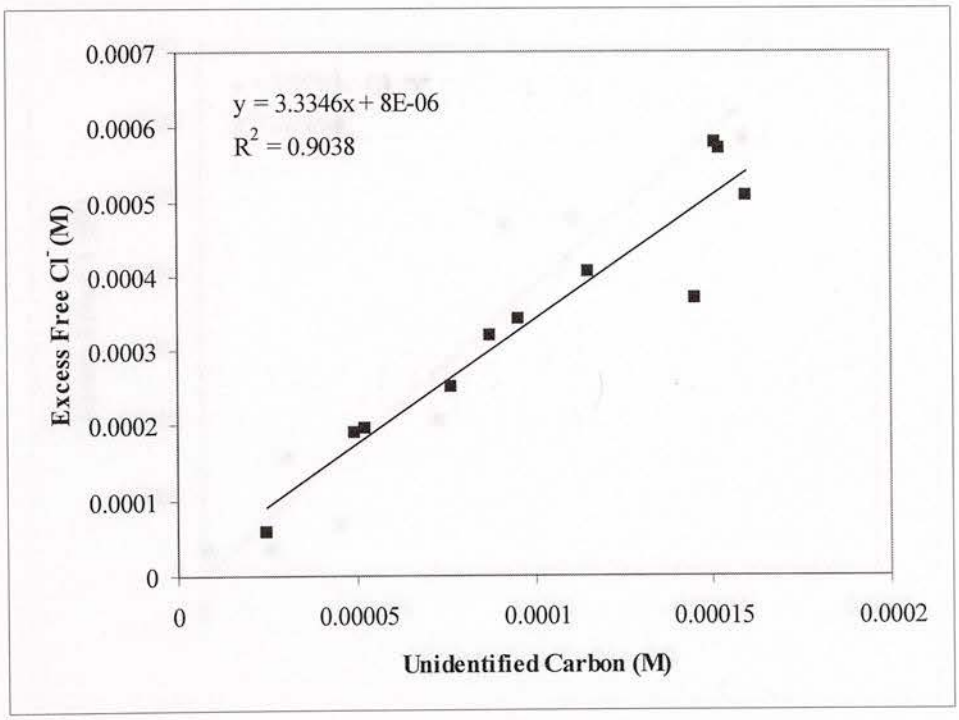

Figure C10. Excess Free Cl^- vs Unidentified Carbon for Peerless Fe^0 System at pH 12

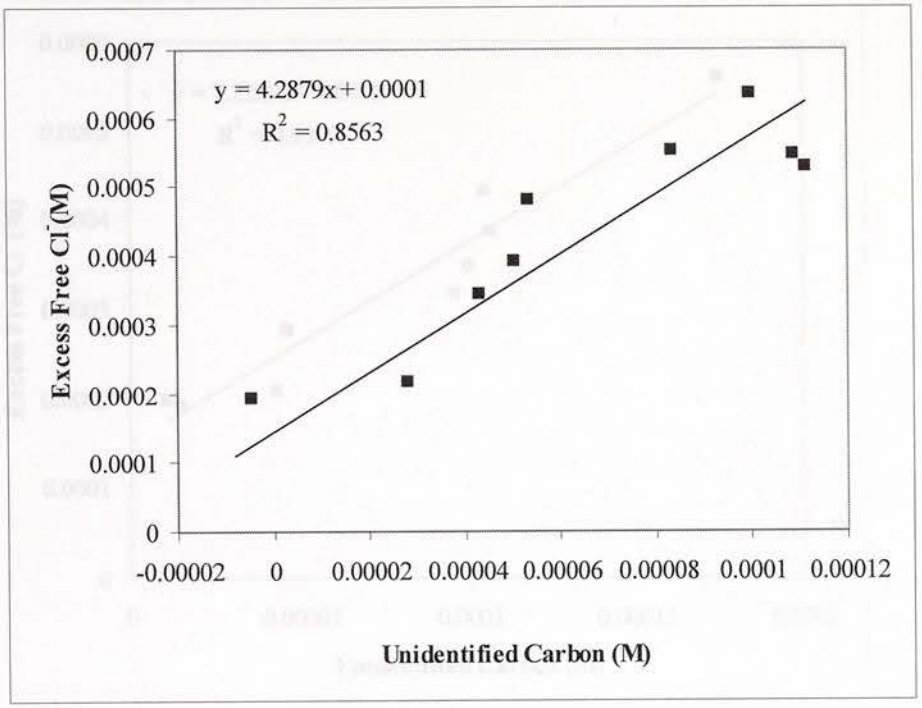

Figure C11. Excess Free Cl^- vs Unidentified Carbon for NaHS-equilibrated FE 99% at pH 7.0

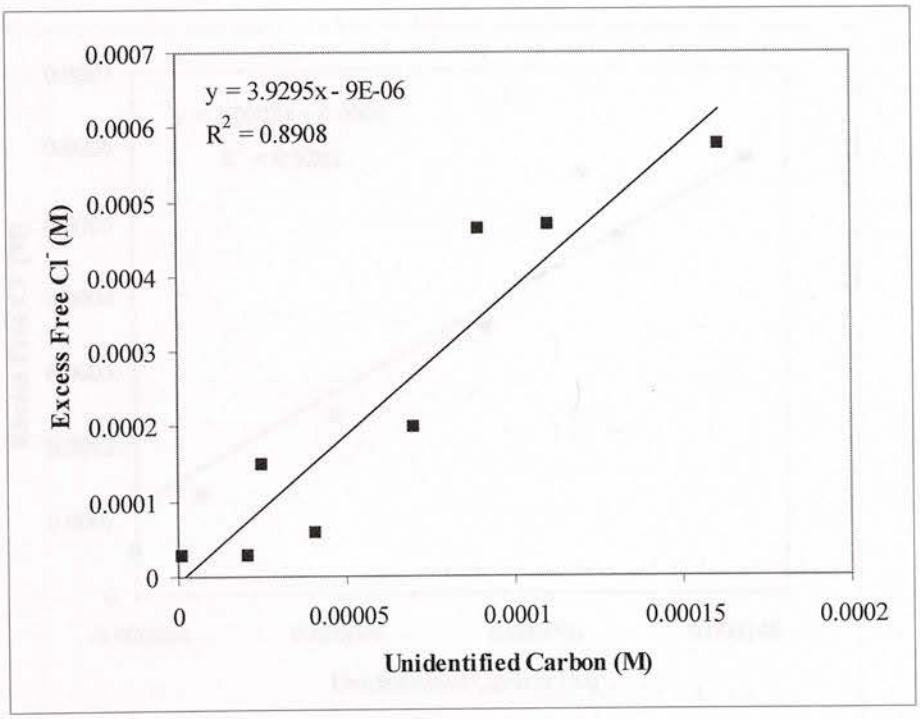

Figure C12. Excess Free Cl^- vs Unidentified Carbon for $MnBr_2$-equilibrated FE 99% at pH 7.0

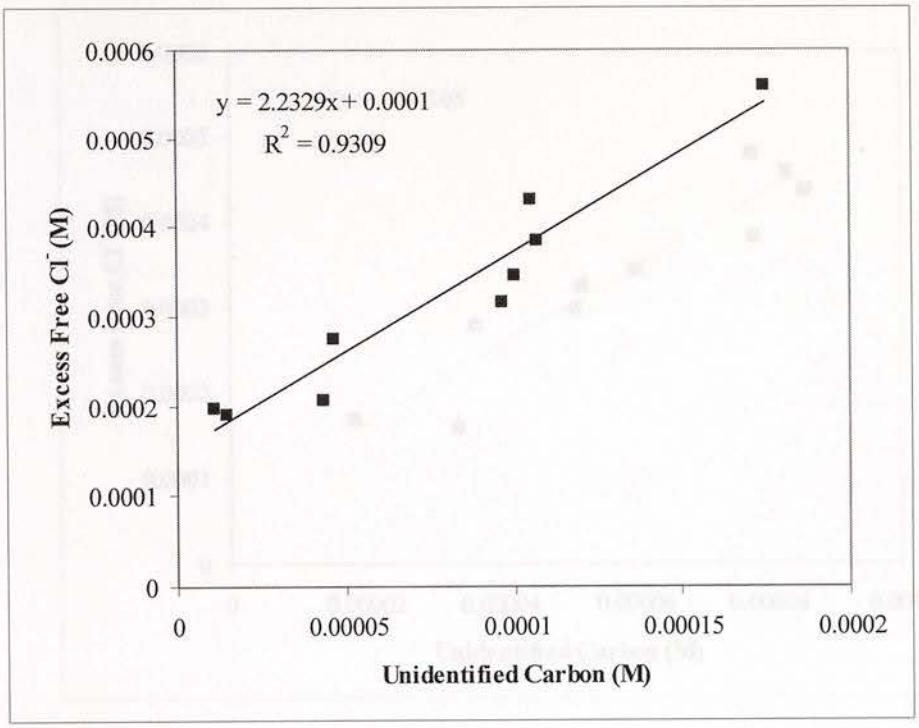

Figure C13. Excess Free Cl^- vs Unidentified Carbon for $NaHCO_3$-equilibrated FE 99% at pH 7.0

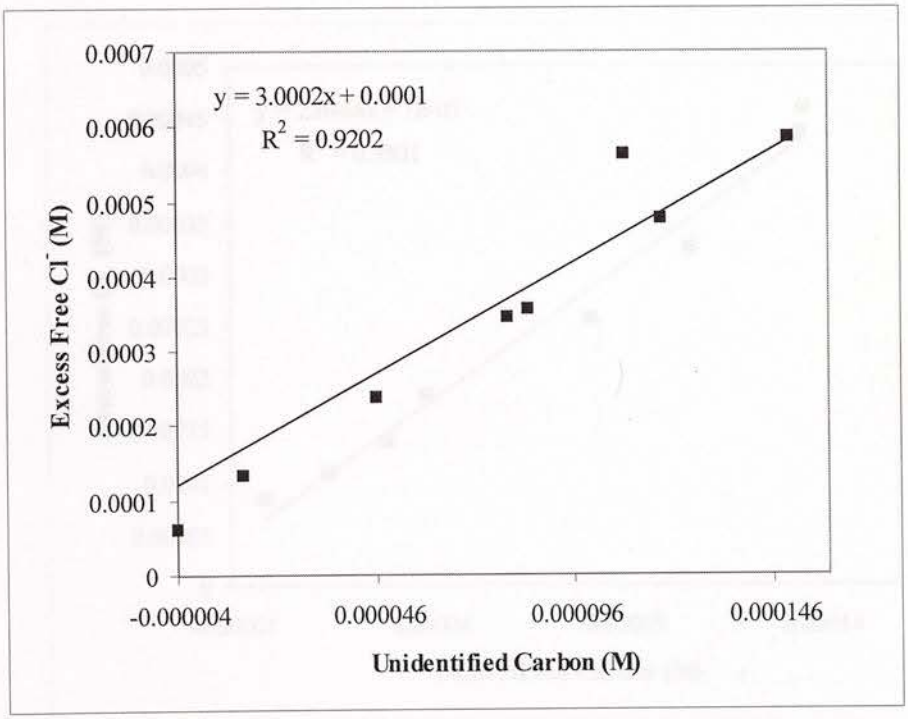

Figure C14. Excess Free Cl^- vs Unidentified Carbon for Acid-washed-FF-40 mesh Fe^0 System at pH 7.0

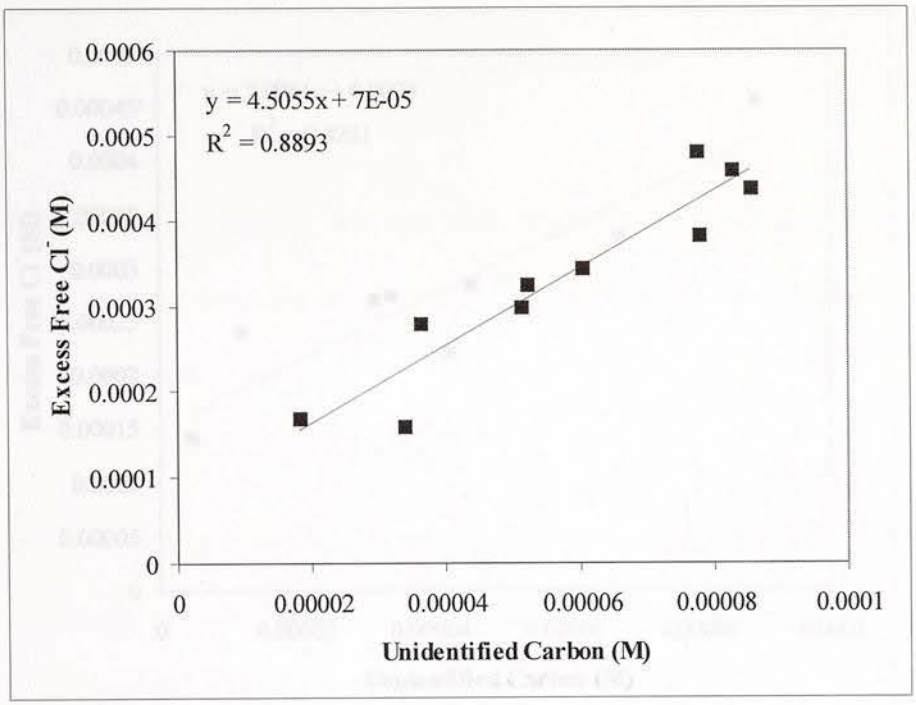

Figure C15. Excess Free Cl^- vs Unidentified Carbon for Acid-washed-Peerless Fe^0 System at pH 7.0

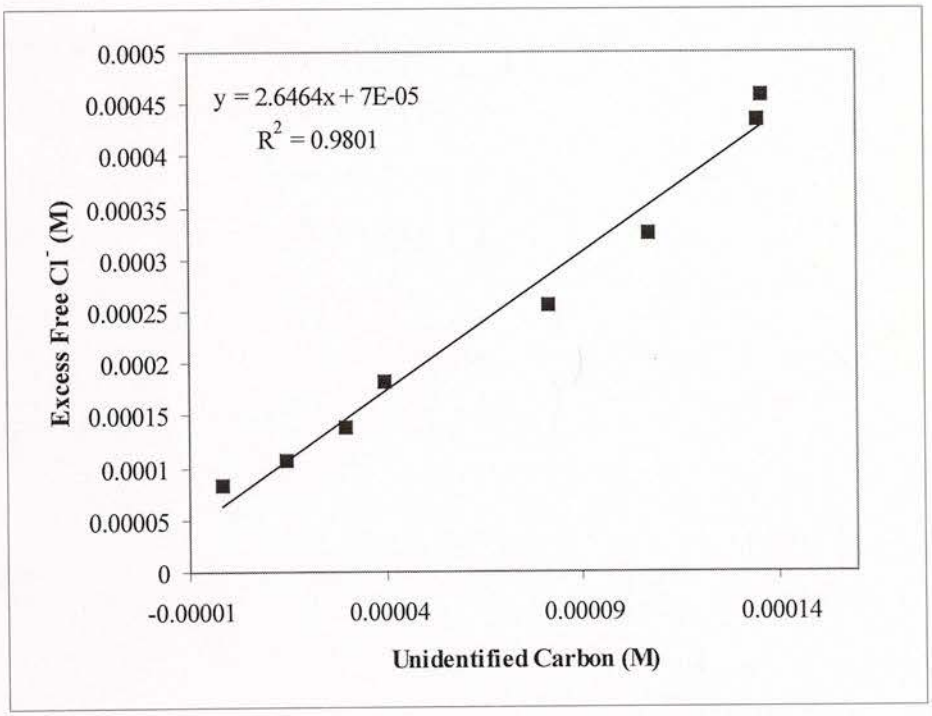

Figure C16. Excess Free Cl^- vs Unidentified Carbon for Acid-washed- FE 93%Fe^0 System at pH 7.0

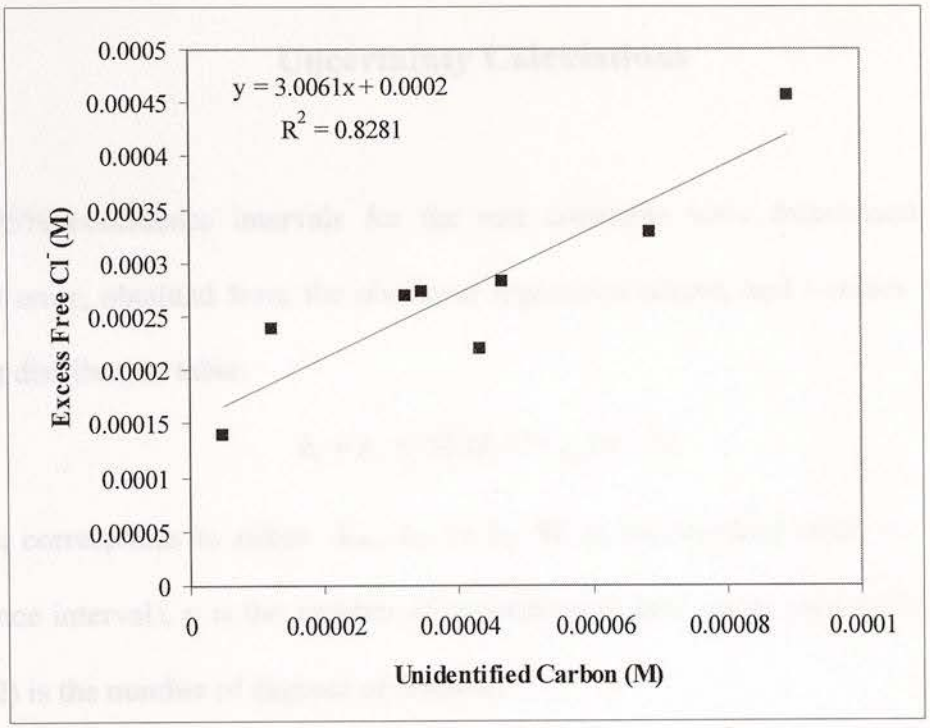

Figure C17. Excess Free Cl^- vs Unidentified Carbon for Acid-washed- FE 99%Fe^0 System at pH 7.0

APPENDIX D

Uncertainty Calculations

95% confidence intervals for the rate constants were determined from their standard error, obtained from the nonlinear regression output, and t-values read from a student t distribution table:

$$k_i = k_i \pm \mathrm{SE}(k_i) * t_{(\alpha/2)}(\mathrm{n}-2)$$

where k_i corresponds to either k_{obs}, k_1, or k_2, SE is the standard error, α = 0.05 (95% confidence interval), n is the number of experimental data points used in the regression, and (n-2) is the number of degrees of freedom.

Error propagation calculations were done to estimate the 95% confidence intervals for the yields of products. For example, for the CF yield (CF yield = k_1/k_{obs}), the standard error of the CF yield, SE(CF yield), due to the standard errors of k_1 and k_{obs}, SE(k_1) and SE(k_{obs}), can be expressed as (*91*):

$$\mathrm{SE(CF\ yield)} = \sqrt{\left(\frac{\partial \mathrm{CF\ yield}}{\partial k_1}\right)^2 \mathrm{SE}^2(k_1) + \left(\frac{\partial \mathrm{CF\ yield}}{\partial k_{obs}}\right)^2 \mathrm{SE}^2(k_{obs})}$$

with

$$\left(\frac{\partial \mathrm{CF\ yield}}{\partial k_1}\right) = \left(\frac{1}{k_{obs}}\right)$$

$$\left(\frac{\partial \mathrm{CF\ yield}}{\partial k_{obs}}\right) = \left(-\frac{k_1}{k^2{}_{obs}}\right)$$

so that

$$\mathrm{CF\ yield} = \mathrm{CF\ yield} \pm \mathrm{SE(CF\ yield)} * t_{(\alpha/2)}(\mathrm{n}-2)$$

This volume is the property of the University of Oklahoma, but the literary rights of the author are a separate property and must be respected. Passages must not be copied or closely paraphrased without the previous written consent of the author. If the reader obtains any assistance from this volume, he must give proper credit in his own work.

I grant the University of Oklahoma Libraries permission to make a copy of my thesis upon the request of individuals or libraries. This permission is granted with the understanding that a copy will be provided for research purposes only, and that requestors will be informed of these restrictions.

NAME [redacted]

DATE [redacted]

A library which borrows this thesis for use by its patrons is expected to secure the signature of each user.

This thesis by MARIA L. TAMARA has been used by the following persons, whose signatures attest their acceptance of the above restrictions.

NAME AND ADDRESS	DATE

OU–138